MULTIPLE STELLAR POPULATIONS OF GLOBULAR CLUSTERS FROM HOMOGENOUS *Ca by* PHOTOMETRY. I. M22 (NGC 6656).[1,2]

Jae-Woo Lee[3,4]

ABSTRACT

We investigate the multiple stellar populations in one of peculiar globular clusters (GCs) M22 using new ground-based wide-field *Ca by* and HST/WFC3 photometry with equivalent passbands, confirming our previous result that M22 has a distinctive red-giant branch (RGB) split mainly due to difference in metal abundances. We also make use of radial velocity measurements of the large number of cluster membership stars by other. Our main results are followings. (i) The RGB and the subgiant branch (SGB) number ratios show that the calcium-weak (*Ca-w*) group is the dominant population of the cluster. However, an irreconcilable difference can be seen in the rather simple two horizontal branch (HB) classification by other. (ii) Each group has its own CN-CH anti-correlation. However, the alleged CN-CH positive correlation is likely illusive. (iii) The location of the RGB bump of the calcium-strong (*Ca-s*) group is significantly fainter, which may pose a challenge to the helium enhancement scenario in the *Ca-s* group. (iv) The positions of the center are similar. (v) The *Ca-w* group is slightly more centrally concentrated, while the the *Ca-s* is more elongated at larger radii. (vi) The mean radial velocities for both groups are similar, but the *Ca-s* group has a larger velocity dispersion. (vii) The *Ca-s* group rotates faster. The plausible scenario for the formation of M22 is that it formed via a merger of two GCs in a dwarf galaxy environment and accreted later to our Galaxy.

---

[1]Based on observations made with the Cerro Tololo Inter-American Observatory (CTIO) 1m and 0.9m telescopes, which are operated by the SMARTS consortium.

[2]Partially based on observations made with the NASA/ESA *Hubble Space Telescope*, obtained at the Space Telescope Science Institute, which is operated by AURA, Inc., under NASA contract NAS 5-26555.

[3]Department of Physics and Astronomy, Sejong University, 98 Gunja-Dong, Gwangjin-Gu, Seoul, 143-747, Korea; jaewoolee@sejong.edu, jaewoolee@sejong.ac.kr

[4]Visiting Astronomer, CTIO, National Optical Astronomy Observatories (NOAO), operated by the Association of Universities for Research in Astronomy, Inc., under cooperative agreement with the National Science Foundation.

Subject headings: globular clusters: individual (M22: NGC 6656) — Hertzsprung-Russell diagram – stars: abundances – stars: evolution

1. INTRODUCTION

The last decade has witnessed a drastic paradigm shift on the true nature of Galactic GCs. In particular, the conventional wisdom of the simple stellar population of GCs is no longer valid in almost all GCs in our Galaxy. In this regard, variations in lighter elements in GC RGB stars have been known for more than three decades (Cohen 1978) and the Na-O anti-correlation, for example, seen in almost all normal GCs (Carretta et al. 2009; D'ercole et al. 2008) is now generally explained by two star formation episodes (see also, Lee 2010), in which the proto-stellar clouds of the second generation of stars must have been polluted by the gaseous ejecta from the first generation of the intermediate-mass asymptotic giant branch (AGB) stars (D'Antona & Ventura 2007) or the fast rotating massive stars (Decressin et al. 2007).

Contrary to normal GCs showing the lighter elemental abundance variations, peculiar GCs such as ω Cen (Lee et al. 1999; Bedin et al. 2004) and M22 (Lee et al. 2009a; Marino et al. 2009, 2011) show spreads in the heavy elemental abundances which synthesized and supplied by the core-collapsed supernovae. To retain ejecta from energetic supernova explosions requires much more massive systems than typical Galactic GCs (Baumgardt et al. 2008). Furthermore, some of massive GCs in our Galaxy appear to have different kinematics than the normal GCs (Lee et al. 2007). As a consequence, these peculiar GCs are thought to have an extragalactic origin, such as being the remnant of dwarf galaxies (for example, see Bekki & Freeman 2003), and they are building blocks of our Galaxy.

One of the early hints on the peculiarity of M22 can be found in Hesser et al. (1977) and Hesser & Harris (1979). They studied M22 using the DDO photometry and the low resolution spectroscopy, finding heterogeneous light elemental abundances in M22 RGB stars. Hesser & Harris also noted that M22 may share the similar elemental abundance anomalies of ω Cen. Later Norris & Freeman (1983) found a variation in calcium abundance as well as those of the CN band and the G band strength in M22 RGB stars. They suggested that calcium abundances among M22 RGB stars can vary up to Δ[Ca/H] $\approx$ 0.3 dex and it is positively correlated with the carbon abundance.

Regarding variations of heavy elemental abundances including calcium in M22, more intriguing results have been emerged in recent years. In our previous work, Lee et al. (2009a) studied M22 using the extended Strömgren photometry and we found the distinctive RGB

split in the hk index [$= (Ca - b) - (b - y)$]. The hk index of RGB stars is a measure of the Ca II H & K absorption strength (Anthony-Twarog et al. 1991) and our previous result indicated discrete calcium abundances among M22 RGB stars (see also Lim et al. 2015). We also showed that two discrete RGB sequences have indeed different iron and calcium abundances by using elemental abundance measurement from the high resolution spectroscopy by Brown & Wallerstein (1992). Da Costa et al. (2009) also obtained the same result from observations of the infrared Ca II triplet that M22 RGB stars show a substantial intrinsic metallicity spread. Finally, Marino et al. (2009, 2011) performed high resolution spectroscopic studies of RGB stars in M22. In addition to the spread in metallicity and the calcium abundance among RGB stars in M22, Marino et al. (2011) found that the metal-rich group of stars have enhanced CNO, which may account for the the split in the SGB, and s-process-element abundances. Furthermore, each stellar group in M22 appears to exhibit its own Na-O anti-correlation. Spectroscopic studies of the M22 HB stars also showed that the the true nature of HB populations may be as complex as that of RGB populations (e.g. Marino et al. 2014a; Gratton et al. 2014). All the available observational evidences up to date may suggest that M22 must have retained not only the material from SNe but also from low-mass and intermediate-mass AGBs[1], reflecting that the formation history of M22 must have been very complex compared to those of the bulk of normal GCs in our Galaxy.

This is the first of the series of papers addressing the multiple stellar populations of Galactic GCs based on the homogenous *Ca by* photometry. In this study we present a new wide-field *Ca by* photometry of M22. As we have extensively demonstrated in our previous work (Lee et al. 2009a), the narrow-band photometric study of GCs can provide an efficient means to investigate multiple stellar populations in the Galactic GC systems. Here we present more evidences that make M22 one of peculiar GCs in our Galaxy.

2. SEJONG *Ca by* SURVEY

Sejong *Ca by* survey program has been launched in July, 2006 after two years of preparation. As an official major partner of the SMARTS consortium, we acquired the guaranteed access to the small telescopes operated at the CTIO since 2006. For 8 years, we used about 270 nights in total, about 120 of which were photometric, for this survey program.

The main goals of our survey program are three fold. Using the extended Strömgren system (Strömgren *by* filters plus the *Ca* filter), we aimed at obtaining followings; i) Homo-

[1]See also Decressin et al. (2007) for the fast rotating massive stars (FRMSs) as a source of the Na-O anti-correlation of GCs.

geneous photometry of individual GCs without prerequisite information of the cluster. We tried to maintain a flux limited blind survey for Galactic GCs. The main purpose of our GC survey program is to study multiple stellar populations of Galactic GC systems to shed more light on the formation of the GC systems and furthermore on the formation of our Galaxy. ii) Metallicity distribution of selected fields in the Galactic bulge, in particular we are very interested in the metal-poor regime of the Galactic bulge. iii) Metallicity distributions and multiple stellar populations of nearby dwarf galaxies.

Our survey program is consisted of three phases. The Phase I was from July, 2006 to November, 2010 (see Lee et al. 2009a,b). During this period, we used Strömgren *uvby* and *Ca* filters provided by the CTIO. The CN band at λ 3885 Å is often very strong in the RGB stars and the CTIO *Ca* filter was originally designed to avoid the CN band contamination. However, it was suspected that the CTIO *Ca* filter had undergone degradation due to aging effect and the original transmission function had been altered to the shorter wavelength. As a result, the CTIO *Ca* filter is suspected to be suffered from the CN band contamination.

Since March 2011 (Phase II), we used our own Strömgren *by* and new *Ca* filters, all of which were manufactured by Asahi Spectra, Japan. Our new *Ca* filter was carefully designed to have very similar filter band width and pivot wavelength as those of F395N filter in the Wide-Field Camera 3 (WFC3) onboard the Hubble Space Telescope (HST). In Figure 1, we show a comparison of filter transmission functions between that in Anthony-Twarog et al. (1991) and that of our new *Ca* filter measured with collimated beam by the manufacturer of the filter. Both filter have similar full-width at the half maximums (FWHMs), approximately 90 Å but our new *Ca* filter has a more uniform and high transmission across the passband, dropping more rapidly at both edges. As shown in the figure, the CN band at λ 3885 Å lies on the lower tail of the *Ca* filter by Anthony-Twarog et al. (1991) while our new *Ca* filter is designed to be completely free from the CN band contamination.

In Figure 1, we also show the filter transmission functions for the HST WFC3 photometry system. The HST WFC3 F547M filter is supposed to be equivalent to the ground-based Strömgren *y* filter. However, the bandwidth of the F547M is twice as broad as the conventional Strömgren *y* filter.

The Phase III started in April 2013, we added a new filter system, $JWL39$, which allows us to measure the CN band at λ 3885 Å in combination with our new *Ca* filter. Note that the bandwidth of $JWL39$ is similar to that of DDO38 (McClure & van den Bergh 1968), but the pivot wavelength of the filter is at $\approx$ 3900 Å. We show the transmission function of our $JWL39$ filter in Figure 1.

In our current work, we will present *Ca by* photometry of M22 taken during the Phases

II and III only. We will present the results using the new $JWL39$ filter system in forthcoming papers.

There are at least two elements of strength in our survey program. First, we used the same instrumental setups, the CTIO 1m telescope and the Y4KCam, for most of our observations except for two runs in 2012, due to the maintenance of the Y4KCam. Second, almost all the data have been obtained by the author of the paper and all the data have been reduced and analyzed by the author of the paper, which guarantees homogeneity of the final results.

3. OBSERVATIONS AND DATA REDUCTION

3.1. Observations

New $Ca\ by$ observations for M22 were made in 44 nights, 23 of which were photometric, in 10 runs from March 2011 to May 2014 using the CTIO 1.0m and 0.9m telescopes. The CTIO 1.0m telescope was equipped with a STA 4k $\times$ 4k CCD camera, providing a plate scale of 0.289 arcsec pixel^{-1} and a field of view of about 20 $\times$ 20 arcmin. The CTIO 0.9m telescope was equipped with the Tektronix 2048 No. 3 CCD, providing a plate scale of 0.40 arcsec pixel^{-1} and a field of view of 13.5 $\times$ 13.5 arcmin. For most of our observations, we used the CTIO 1.0m telescope except for one semester. The Y4KCam mounted on the CTIO 1.0m telescope had been under inspection at Steward Observatory, Arizona, USA during the spring semester of 2012, and we used the CTIO 0.9m telescope for two runs in April and July 2012.

The total exposure times for M22 were 90,900 s, 20,930 s and 9,145 s for our new Ca, Strömgren b and y, respectively. We show the journal of observations in Table 1.

3.2. Data Reduction

The raw data were processed through the standard IRAF[2] packages using twilight or dawn sky flat images to calibrate science exposures. Since both CCD cameras are equipped with an iris type shutter, the illumination across the CCD chips is not uniform and the

[2]IRAF (Image Reduction and Analysis Facility) is distributed by the NOAO, which are operated by the Association of Universities for Research in Astronomy, Inc., under contract with the National Science Foundation.

shutter shading correction is applied for the photometric standard frames with the exposure times shorter than 10 s (see Lee & Pogge 2015, for detailed discussion). Note that the difference in the integration time between the center and the edge of the CCD is $\approx$ 70 msec for the Y4KCam. The most of photometric standards by Twarog & Anthony-Twarog (1995) and Anthony-Twarog & Twarog (1998) are too bright even for the small telescope like the CTIO 1.0m telescope. For most cases, we intended to have exposure times longer than 10 s. Although defocusing observing technique has been frequently used to observe isolated bright stars in the field, such as photometric standards, the most of the standard stars are still too bright to be observed with a integration time of longer than $\approx$ 10 s. Without any viable options, science frames with a short integration time are often necessary in order to secure wide range in colors of photometric standards, especially in y passband.

The field of view of the final combined science image of M22 is about 55 $\times$ 55 arcmin, which is more than 7 times larger than that of our previous study of the cluster (Lee et al. 2009a). The photometry of the cluster and photometric standard frames were analyzed using DAOPHOTII, DAOGROW, ALLSTAR and ALLFRAME, and COLLECT-CCDAVE-NEWTRIAL packages (Stetson 1987, 1993, 1994, 1995; Turner 1995) following the method described in Lee & Carney (1999) and Lee et al. (2014). In order to derive the transformation relations from the instrumental system to the standard system, we adopt the following equations:

$$\begin{aligned} y_{inst} &= y_{STD} + \alpha_y (b-y)_{STD} + \beta_y X + \gamma_y, \\ b_{inst} &= b_{STD} + \alpha_b (b-y)_{STD} + \beta_b X + \gamma_b, \\ Ca_{inst} &= Ca_{STD} + \alpha_{Ca} (b-y)_{STD} + \beta_{Ca} X + \delta hk_{STD} + \gamma_{Ca}, \end{aligned} \tag{1}$$

where X is the airmass and y_{STD}, b_{STD}, Ca_{STD}, $(b-y)_{STD}$ and hk_{STD} are the magnitudes and color on the standard system. The total number of stars measured in our M22 field from our ALLFRAME run was more than 518,000. Most of stars measured in our field turned out to be Galactic bulge stars.

In Figure 2 and Table 2, we show comparisons of our photometry with those of previous studies by Anthony-Twarog et al. (1995) and Richter et al. (1999). In the figure, the differences are given in the sense of other works minus our work. It can be seen that our results are in good agreement with previous studies within measurement errors. It should be emphasized that total exposure times of our observations in each passband are much greater than those of Anthony-Twarog et al. (1995) and Richter et al. (1999), and, therefore, the photometric quality of our work is believed to be superior to those of previous works.

Finally, astrometric solutions for individual stars in our field have been derived using the data extracted from the Naval Observatory Merged Astrometric Dataset (NOMAD,

Zachairias et al. 2004). We achieved the rms scatter in the residuals of less than 0.07 arcsec using the IRAF IMCOORS package. Then the astrometric solution was applied to calculate the equatorial coordinates for all stars measured in our science frames.

3.3. Completeness tests

To examine the completeness of our photometry as a function of V magnitude, we performed a series of artificial star experiments (see for example, Stetson & Harris 1988). We selected two square regions with a size of about 15×15 arcmin from the central part and the outer part of the cluster. We constructed a fortran program to distribute 1,000 stars in both fields by adopting the observed radial stellar number density and the luminosity profiles in our study. Note that the number of artificial stars used in our experiments corresponds to about 1.3% and 5.6% of the total measured number of stars in the central and the outer part of the cluster, respectively. This number of artificial stars added to the observed images is carefully chosen not to dramatically change the crowdedness characteristics between our data reduction procedures and our artificial star experiments.

We used the observed point-spread functions (PSFs) and the DAOPHOT's ADDSTAR task to generate 20 artificial star images in each field. Following the same data reduction procedure that we described above, we derived the completeness fractions as a function of V magnitude. We show our results in Figure 3. As shown in the figure our experiments suggest that our photometry is complete down to $V \approx 18.5$ mag both in the central and in the outer field of the cluster for the ground-based observations. As will be discussed below, it should be emphasized that incompleteness at the fainter magnitude regime does not affect our results presented in this work.

4. RESULTS

4.1. Color-Magnitude Diagrams

4.1.1. Ground-based observations: field star contamination

In Table 3, we provide our photometric data for stars brighter than $V = 19$ mag. Figure 4 shows the color-magnitude diagrams (CMDs) of bright stars in the M22 field. Note that, for the sake of clarity, we show stars within 10 arcmin from the center of the cluster. As can be seen in the figure, the double RGB sequences of M22 can be clearly seen, especially the distinctive split in the RGB stars in the hk versus V CMD. Note that the $m1$ versus V

CMD is from our previous study of the cluster (Lee et al. 2009a) taken during the Phase I period.

Since M22 is located towards the Galactic bulge ($l = 9.9°$, $b = -7.6°$), the contribution from the field star contamination is naturally expected to be very large (see Lee et al. 2009a, for detailed discussions). We attempted to remove the off-cluster field stars in our bright RGB sample by using multi-color CMDs following the method described in Lee et al. (2009a,b), which turned out to be very successful as discussed below.

In Figure 5–(a) and (b), we show CMDs of the M22 field using all the stars measured from $V = 11.5$ mag to 17.5 mag. In the figures, blue solid lines indicate the RGB boundary grids in the $(b-y)$ versus V and in the hk versus V CMDs. In order to prepare these RGB boundary grids, we made use of the fiducial sequence of the model isochrones by Joo & Lee (2013), which were kindly provided by S.-J. Joo, and we adopted the distance modulus and the foreground reddening value for M22 by Harris (1996). Then we added small amount of color offset values, $\Delta(b-y) \approx \pm$ 0.04 mag and $\Delta hk \approx \pm$ 0.07 mag, in the transformed model isochrone sequences to make the final RGB boundary grids. Although our definitions of the RGB boundary grids for $(b-y)$ and hk indexes appear to be arbitrary, our approach appears to work with great satisfaction as shown below.

The total number of RGB stars detected in the enclosed region in Figure 5–(c), is 3571. When plotted in the hk versus V plane, it can be clearly seen that about 42% of RGB stars selected in the $(b-y)$ versus V plane does not belong to M22, i.e. either the disk or the bulge populations with large hk index values. A comparison with the radial velocity measurements by Lane et al. (2009) shows that 12 stars out of 307 stars in common turn out to be radial velocity non-member stars. If we take this as a face value, the fraction of the inclusion of the off-cluster field population in our M22 RGB selection procedure is 3.9 $\pm$ 1.4%, which appears to be too low to dramatically change the results presented in this paper. Without 12 radial velocity non-member stars, we have, 2,054 RGB stars, from $V = 12.0$ mag to 16.5 mag, in total.

The validity of our RGB selection procedure can be confirmed by the surface-brightness profile (SBP) of the RGB stars in M22. In Figure 6-(d), we show the SBP of the red-clump stars in the Galactic bulge [the stars lie inside a cyan box in Figure 5–(a)]. As expected, the SBP of the bulge population is almost flat against the radial distance from the center of M22. Note that the mild fluctuation seen in the small r region, $\log(r/\mathrm{arcsec}) \lesssim 2$, is due to the small number of the bulge red-clump stars ($n \leq 15$) detected in this region.

Figure 6-(a)–(c) show the SBPs of the *Ca-w* group, the *Ca-s* group and all RGB stars in M22 (see below for details on the definition of the *Ca-w* and the *Ca-s* groups). With slightly

different zero-point offset values for each group of stars, our SBPs for M22 RGB stars are in excellent agreement with the Chebyshev polynomial fit of M22 by Trager et al. (1995) up to more than 10^3 arcsec from the center of the cluster. Our investigation of the SBPs of M22 RGB stars strongly suggests that the contamination of the off-cluster field star in our result is not severe, consistent with our previous result from the comparison of the radial velocity measurements of M22 RGB stars.

4.1.2. Ground-based observations: Ca-w versus Ca-s

As shown in Figures 4 and 5, M22 exhibits the distinctive double RGB sequences in the hk versus V CMD, which is mainly due to the difference in the heavy elemental abundances between the two groups (see also Lee et al. 2009a; Marino et al. 2009, 2011). As in our previous works (Lee et al. 2009a,b), we define the calcium-weak (Ca-w) group of stars with smaller hk index and the calcium-strong (Ca-s) group of stars with larger hk index at a given V magnitude.

In the left panel of Figure 7, we show 2,054 RGB stars from Figure 5–(d) on the Δhk versus V plane, where Δhk is defined to be the difference in the hk index of the individual RGB stars with respect to the hk index of the fiducial sequence of the Ca-w RGB group. As shown, the differences in the hk index between the mean values of the Ca-w and the Ca-s depend slightly on V magnitude, which is naturally expected if the difference in the absorption strengths of Ca II H and K lines is mainly responsible for the separation in the hk index of the RGB stars. Due to this magnitude (more precisely, surface gravity) dependency on the Δhk, we divide M22 RGB stars into four different magnitude bins and we show histograms of the Δhk distributions of RGB stars of each magnitude bin in the right panels of Figure 7, all of which appear to show double peaks. In order to separate the two different groups of RGB stars based on the Δhk distribution, we adopt the expectation maximization (EM) algorithm for the two-component Gaussian mixture distribution model. In an iterative manner, we derive the probability of individual RGB stars for being the Ca-w and the Ca-s groups. In the left panel of Figure 7, stars with $P(w|x_i) \geq 0.5$ from the EM estimator are denoted with blue dots which corresponds to the Ca-w group, while $P(s|x_i) > 0.5$ with red dots which corresponds to the Ca-s group. In the right panel of the figure, we show the distributions of the Ca-w and the Ca-s groups with blue and red solid lines, respectively, and we show the number ratio $n(Ca\text{-}w)$:$n(Ca\text{-}s)$ for each bin. In total the number ratio between the Ca-w and the Ca-s groups is $n(Ca\text{-}w)$:$n(Ca\text{-}s)$ = 68.8:31.2 ($\pm$3.3).

Our observed number ratio between the two groups does not necessarily reflect the initial stellar number ratio or the initial mass ratio between the two groups, since both groups

have different initial chemical compositions, different masses at a given luminosity, and furthermore slightly different ages (e.g., Lee et al. 2009a; Marino et al. 2009, 2011; Joo & Lee 2013). In order to take care of the heterogeneous evolutionary effects between the two groups, we constructed an evolutionary population synthesis model using the theoretical model isochrones by Joo & Lee (2013). We populated 10^7 artificial stars in each group using the Salpeter's initial mass function (IMF) and we generated 50 different sets for each group. We, then, compared the number ratios between the two groups in the magnitude range of $12.0 \leq V \leq 16.5$ mag, finding $n(Ca\text{-}w)$:$n(Ca\text{-}s) = 48.3$:51.7 ($\pm$ 0.3), in the sense that RGB stars in the Ca-s group are slightly more numerous than those in the Ca-w group at a fixed total number of stars in both groups. Note that using other types of IMF does not affect our results presented here, which was also pointed out by Joo & Lee (2013). As an exercise, we calculated the number ratio using the universal IMF by Kroupa (2001) and we obtained $n(Ca\text{-}w)$:$n(Ca\text{-}s) = 48.4$:51.6 ($\pm$ 0.3), in excellent agreement with that from the Salpeter's IMF within the 0.1% level.

Figure 8 shows the mean theoretical luminosity functions (LFs) for the Ca-w and the Ca-s groups. Note that the abscissa of the figure is M_V and the grey shaded area is corresponding to M22 RGB stars with $12.0 \leq V \leq 16.5$ mag. As can be seen, the theoretical LFs for the RGB stars in both groups are very similar. If we consider the evolutionary effect, the intrinsic or the true number ratio between the two groups becomes $n(Ca\text{-}w)$:$n(Ca\text{-}s) = 70.2$:29.8 ($\pm$3.3). Note that our new RGB number ratio is in good agreement with our previous rough estimate of the number ratio between the two groups, $\approx$ 0.70:0.30 (Lee et al. 2009a).

As discussed by Lee et al. (2009a) and Marino et al. (2009, 2011), the double RGB sequences in M22 is due to the difference in chemical abundances between the Ca-w and the Ca-s groups, in particular the difference in the calcium abundance measured with the Ca filter and in heavy elements, which was first hinted by the high-resolution spectroscopy of seven RGB stars by Brown & Wallerstein (1992) and confirmed later by Marino et al. (2009, 2011) with the expanded sample of RGB stars of the cluster. More detailed discussion on the difference in the chemical abundances between the two groups will be given below. Also worth emphasizing is the fact that the differential reddening effect and the contamination from the off-cluster populations cannot explain the double RGB sequences in M22 (Lee et al. 2009a). Assuming that the conventional interstellar reddening law for the extended Strömgren photometry system by Anthony-Twarog et al. (1991), $E(hk) = -0.16 \times E(b-y) \approx -0.12 \times E(B-V)$, the mean hk difference between the two RGB groups, $\Delta hk = 0.09$ mag, can be translated into $\Delta(b-y) = -0.56$ mag, $\Delta(B-V) = -0.75$ mag and $\Delta V = -2.33$ mag, in the sense that the metal-rich Ca-s RGB stars becomes bluer and brighter due to the foreground reddening. Indeed, this is not the case.

4.1.3. Ground-based observations: $m1$ versus V

The Strömgren v passband includes the CN band at λ 4215 Å and, as a consequence, $m1$ index [$= (v-b)-(b-y)$] is capable of distinguish the difference in the CN absorption strengths. In fact, the bimodal distribution in the $m1$ index of M22 RGB stars was known for decades and it has been frequently attributed to the bimodal distribution in the CN abundances (Norris & Freeman 1983; Anthony-Twarog et al. 1995; Richter et al. 1999; Lee et al. 2009a). It is widely accepted that the variation of lighter elemental abundances, such as C, N and O, is thought to be resulted from chemical pollution by the intermediate-mass AGB stars (see, for example, Ventura et al. 2001). The potential trouble with the $m1$ index is that the split between the double populations at the lower RGB sequence is not readily distinguishable in the $m1$ versus V CMD, most likely due to the strong surface gravity sensitivity on the CN band strength, in the sense that the CN band strength is inversely correlated with the surface gravity of stars (see for example, Tripicco & Bell 1991; Cannon et al. 1998), as shown in Figure 4.

On the other hand, as Lee et al. (2009a) discussed extensively, the hk index is a measure of calcium abundances of individual stars and, therefore, the difference in the hk index at a given luminosity indicates the heterogeneous calcium and other heavy elemental abundances between the double RGB populations in M22, which is confirmed by the high-resolution spectroscopic study of RGB stars in the cluster (Brown & Wallerstein 1992; Marino et al. 2009, 2011). Calcium and heavy elements can only be supplied through supernovae explosions of massive stars and the origin of the split in the hk index is intrinsically different from that in the $m1$ index in M22, if the $m1$ index is the most sensitively depends on the CN abundances as previous investigators perceived frequently. It is important to note that, however, since the Strömgren v passband includes numerous metallic lines, the $m1$ index also sensitively behaves in the difference in the heavy metal abundances.

In the top panels of Figure 9, we show the CMDs of M22 again. For the $m1$ versus V CMD, we show stars with $(b-y) \geq 0.45$ mag to prevent the degeneracy of the location of the HB and the RGB stars in the $m1$ versus V CMD. We also show the Padova model isochrones with [Fe/H] $= -1.8$ dex, comparable to that of the *Ca-w* group, and -1.5 dex, comparable to or slightly more metal rich than that of the *Ca-s* group, with a fixed [CNO/Fe] ratio (Bressan et al. 2012). From the figure, it is palpable that the bifurcation in the RGB sequences on the $m1$ versus V CMD is mainly due to the difference in the metal abundance. In addition, the higher mean [CNO/Fe] ratio in the *Ca-s* group[2] may intensify the difference in the $m1$ index between the two groups.

[2]The s-process-rich group by Marino et al. (2011).

A comparison of M22 with two Galactic GCs, M55 and NGC 6752 (Lee 2015 in preparation), may help to elucidate the nature of the double RGB sequences. Note that the metallicity of M55 is [Fe/H] = −1.9 dex, equivalent to the *Ca-w* group in M22, while that of NGC 6752 is −1.5 dex, equivalent to the *Ca-s* group in M22. It is well known that the HB morphologies of both clusters are different. M55 contains only the blue HB (BHB) population, while NGC 6752 contains the BHB and the extreme blue HB (EBHB) populations. The CN distributions of both clusters are also different. M55 appears to show an unimodal CN distribution (Kayser et al. 2008), in sharp contrast to the bimodal CN distribution of NGC 6752 (Norris et al. 1981).

In the bottom panels of Figure 9, we show the composite CMDs of M55 and NGC 6752. In order to make these composite CMDs, we tweaked the color indexes and the visual magnitude of individual stars in NGC 6752 to match with those in M55; $\Delta(b-y) = 0.034$ mag, $\Delta m1 = -0.008$ mag, $\Delta hk = -0.001$ mag and $\Delta V = 0.654$ mag. In the $m1$ versus V CMD, we do not plot the HB stars in M55 and NGC 6752 to avoid the confusion with the RGB stars. We emphasize that these composite CMDs can successfully reproduce the photometric characteristics of M22. Especially, the CMDs of M22 and the composite GCs show remarkable resemblance in the HB morphology and the double RGB sequences both in the $m1$ and the hk indexes, suggesting that the double RGB sequence in the $m1$ index of M22 is likely due to the difference in the mean heavy metal abundance. If so, the origin of the RGB split in the $m1$ index is the same as that of the hk index in M22.

Nonetheless, using the hk index as a metallicity indicator has advantages. As Anthony-Twarog et al. (1991) noted, the hk index is about three times more sensitive to metallicity than the $m1$ index is, for stars more metal-poor than the Sun, and it has half the sensitivity of the $m1$ index to interstellar reddening. The annoying trouble with the $m1$ index is that it loses sensitivity to metallicity changes in the regime below [Fe/H] ≈ -2 dex, especially for stars with higher surface gravity.

4.1.4. Hubble Space Telescope Observations

We also carried out the HST WFC3 photometry for the central part of M22. In Figure 10, we show the preliminary results from HST WFC3 observations of the cluster (PI : J.-W. Lee and PID : 12193) using the similar passbands that we used in our ground-based observations.

The left panel of the figure shows the $(m_{\rm F467M} - m_{\rm F547M})$ versus $m_{\rm F547M}$ CMD, which is equivalent to the ground-based $(b-y)$ versus V CMD, near the the subgiant branch (SGB)

and the faint RGB regions of M22. Similar to the ground-based $(b-y)$ versus V CMD, the split in the RGB or SGB can not be readily seen in the figure.

On the other hand, the $hk_{\rm STMAG}$ [$= (m_{\rm F395N} - m_{\rm F467M}) - (m_{\rm F467M} - m_{\rm F547M})$] versus $m_{\rm F547M}$ CMD shows the distinctive split in the the SGB and the RGB sequences of M22, confirming the results from our new ground-based observations discussed above. Note that the SGB split in M22 has been already known in other HST passbands by Marino et al. (2009, 2012) and the presence of the SGB split is likely due to variations in the CNO abundance (Cassisi et al. 2008) . Especially, Marino et al. (2012) performed a low-resolution spectroscopic study for a large number of SGB stars in M22, finding that the elemental abundance trend of the faint SBG (fSGB) group is consistent with that of the *s*-process-rich group in their early study (Marino et al. 2011, i.e. *Ca-s* in this study), while the elemental abundance trend of the bright SGB (bSGB) is consistent with that of the *s*-process-poor group (i.e. the *Ca-w* group), demonstrating that the observed difference in the CNO abundance can account for the observed SGB split.

Milone et al. (2009) devised a rather clever but complicated method to estimate the number ratio between the fSGB and the bSGB in NGC 1851. However, there are at least three aspects that make difficult for M22 to be analyzed using the method described by Milone et al. (2009). First, the spatial stellar number density in a fixed area on the sky (i.e. the number of stars/$\Box''$) of M22 is about 20 times smaller than that of NGC 1851. Therefore, the number of the SGB stars detected in our HST observations for M22 are much smaller than that in NGC 1851 by Milone et al. (2009). The small number of stars makes it difficult to delineate a clear SGB fiducial sequence for M22. Secondly, the foreground interstellar reddening value of M22, $E(B-V) = 0.34$, is much larger than that of NGC 1851, $E(B-V)$ = 0.02 (Harris 1996). Furthermore, there may exist the differential foreground reddening effect across M22, although the differential reddening is not the main reason for showing the double RGB or SGB sequences in M22 as we have already discussed. Lastly, the curvature of the SGB stars and the location of the transition region between the SGB and the base of the RGB are different between the HST hk_{STMAG} and the $F606W - F814W$ photometric systems. The essential idea of the method proposed by Milone et al. (2009) is to estimate the intrinsic or the true number ratio between the two SGB populations, derived from the apparent number ratio by taking care of the evolutionary effect as we have done for the RGB stars. It also should be important to point out that their method is arbitrary and model dependent, as they have noted.

Before turning to the observed number ratio between the two SGB groups in M22, we investigate the methodological aspect by employing the evolutionary population synthesis models that we constructed for the RGB stars above. In the left panels of Figure 11, we

show artificial CMDs around the SGB region of M22 for different photometric systems. In order to construct the evolutionary population synthesis models, we use the model isochrones by Joo & Lee (2013) with the Salpeter's IMF. The photometric errors are estimated from the measurement errors around the SGB region in our HST observations. We populate 10^8 artificial stars in each group. In the figure, blue dots denote the bSGB group while red dots the fSGB in M22. For the sake of clarity, we only show a small fraction of stars in the figure. We then count the numbers of SGB stars for each group at a fixed color range (the vertically shaded areas) and at a fixed magnitude range (the horizontally shaded areas) returned from our calculations.

The middle panels of Figure 11 show the distributions of SGB stars in the fixed color ranges for the different photometric systems, while the right panels show those in the fixed magnitude ranges. Similar to our RGB number ratio estimates, we calculate the differences in the magnitudes or in the color indexes against those of the fiducial sequences of the bSGB group. The first number ratios in each plot are those returned from the EM estimator assuming the two-component gaussian mixture model while the number ratios inside the parenthesis are the input values used in our evolutionary population models. Note that these number ratios in the parenthesis reflect the evolutionary effect between the two SGB groups at a given color or magnitude ranges. In the figure, our adopted ranges in each color index may be rather arbitrary but we intend to maximize the available number of stars maintaining the clear separation between the two SGB groups.

First, the SGB number ratio returned from the EM estimator between the two groups at the fixed (F606W − F814W) color is n(bSGB):n(fSGB) = 42:58, while that of the input value from the evolutionary population synthesis models is 39:61. On the other hand, the SGB number ratio determined at the fixed F606W magnitude appears to be more uncertain. We obtained n(bSGB):n(fSGB) = 63:37 with the input value of 56:43.

Next, the SGB number ratios determined from the $b - y$ versus V CMD appear to be the least reliable in our simulations. We obtain n(bSGB):n(fSGB) = 44:56 for the fixed color and 72:28 for the fixed magnitude ranges, which number ratios deviate largely from the input values of 38:62 and 65:35, respectively.

Lastly, the SGB number ratios determined from the hk versus V CMD appear to be the most reliable. Due to the combined effect of the mean heavy metal and the CNO abundances on the location of the SGB sequence on the hk versus V CMD, the separation in the hk index between the two SGB groups is the most conspicuous. The EM estimator securely retrieve the input values within an uncertainty of $\leq \pm$ 0.2. Since our simulations suggest that the total number of stars available in our simulations for the hk versus V CMD is about 3 times larger for the case with the fixed magnitude range, we estimate the observed SGB number

ratio from our HST observations of the cluster using the method with a fixed magnitude range, i.e. using the distribution of individual stars against Δhk, as for the RGB stars. Also importantly, using the method with a fixed magnitude range has an advantage in correcting the evolutionary effect. The SGB number ratio of n(bSGB):n(fSGB) = 58:42 is, in fact, the evolutionary effect correction factor shown in Figure 8 (the yellow shaded area) and applying the correction factor of the differential evolutionary effect based on the V magnitude is more direct.

In Figure 12-(a), we show the $hk_{\rm STMAG}$ versus $m_{\rm F547M}$ CMD around the SGB region of M22. Also shown is the fiducial sequence for the bSGB group. Following the similar procedure that we used for the RGB stars, we obtain the number ratio of n(bSGB):n(fSGB) = 69:31 ($\pm$ 6). If we apply the correction factor for the differential evolutionary effect between the two group, the intrinsic number density becomes n(bSGB):n(fSGB) = 62:38 ($\pm$ 6). This SGB number ratio is in agreement with the RGB number ratio, $n(Ca\text{-}w)$:$n(Ca\text{-}s)$ = 70:30 ($\pm$ 3.3), within the measurement errors.

As mentioned above, Marino et al. (2009, see references therein) already discovered the SGB split in their HST Advanced Camera for Surveys Wide Field Channel (ACS/WFC) observations of M22 using F606W and F814W passbands, although the separation between the fSGB and the bSGB populations in the $m_{\rm F606W} - m_{\rm F814W}$ versus $m_{\rm F814W}$ CMD is not as clear as that in $hk_{\rm STMAG}$ versus $m_{\rm F547M}$ CMD as shown here. Their SGB number ratio is n(bSGB):n(fSGB) = 62:38 ($\pm$ 5), which is in excellent agreement with our true SGB number ratio n(bSGB):n(fSGB) = 62:38 ($\pm$ 6).

Finally, it should be worth mentioning that the hk separation between the two SGB groups in the observed CMD (Figure 10) is more ambiguous than that of the simulated CMD with a proper treatment of the photometric measurement errors (Figure 11). This may indicate that not only the differential reddening but also the metallicity spreads in the double SGB populations are necessary to perform more realistic simulations. In fact, Marino et al. (2011) reported rather large metallicity spreads for the two groups of RGB stars; 0.10 dex for the s-process-poor group and 0.05 dex for the s-process-rich group. As shown in Figure 9, the $(b-y)$ width of M22 is compatible with that of the composite GC (i.e. NGC 6752 + M55), where the $(b-y)$ locus of the RGB sequence is less sensitive to the variation in the heavy metal abundance, while the hk width of M22 is broader than that of the composite GC. Given the current interstellar reddening law (see below for more detail), the reasonable explanation for the broader RGB sequence of M22 in the hk index is likely due to the spread in the heavy metal abundances of both stellar groups in M22.

4.2. Differences in Chemical Abundances between Two RGB Groups

Lee et al. (2009a) showed that the distinctive RGB split in the *hk* index in M22 is originated due to the heterogeneous heavy elemental abundances, in particular calcium. In our previous work, we demonstrated that the RGB stars in the *Ca-s* group in M22 are in fact Ca-rich, based on seven RGB stars studied by Brown & Wallerstein (1992).

Here, using the expanded sample of RGB stars studied by Norris & Freeman (1983), Da Costa et al. (2009), and Marino et al. (2011), we compared the differences in the elemental abundances between the *Ca-w* and *Ca-s* groups in M22, providing more observational evidences that the two populations of stars are intrinsically different.

4.2.1. Comparisons with Norris & Freeman (1983)

Hesser et al. (1977) and Hesser & Harris (1979) first noticed that M22 have RGB stars with heterogeneous light elemental abundances using the DDO photometry and the low resolution spectroscopy, respectively, leading them to suggest that M22 may share the similar elemental abundance anomalies of ω Cen. Later Norris & Freeman (1983) performed a spectroscopic survey study for about 100 RGB stars in the cluster and they showed that the calcium abundance is correlated with the CN band and the G band strengths in RGB stars in M22.

In Figure 13, we show a plot of the calcium index A(Ca) as a function of V magnitude [see Equation (2) of Norris & Freeman for the definition of the A(Ca) index]. In the Figure, we also show the least square fit to the *Ca-w* RGB stars, which can provide a baseline, and we calculate the deviations of individual stars from the fitted line. As discussed by Norris & Freeman (1983), the residuals of individual stars from this fitted line against the V magnitude may correct the temperature and the surface gravity effects on the absorption strengths to the first order. The figure shows that the A(Ca) index of Norris & Freeman (1983) is correlated well with our *hk* index, which should not be a surprise because both quantities measure the same Ca II H and K line strength of RGB stars photometrically and spectroscopically.

4.2.2. Comparisons with Da Costa et al. (2009)

Da Costa et al. (2009) studied M22 RGB stars using intermediate resolution spectra and they obtained infrared Ca II triplet strengths Σ(CaT) ($= W_{8542}+W_{8662}$) for membership RGB

stars, finding a substantial intrinsic metallicity spread in M22 RGB stars. The advantage of using the infrared Ca II triplet is that these lines arises from a lower energy level of 1.70 eV, while the lower energy level of Ca II H and K lines is 0 eV. Therefore, the infrared Ca II triplet lines do not suffer from interstellar reddening contamination.[3] Also, since the absorption lines from other elements around the infrared Ca II triplet lines are sparsely populated, contamination from absorption lines of other elements would be less severe.

In the upper panel of Figure 14, we show the plot of Σ(CaT) against $V - V_{\rm HB}$, the V magnitude difference from the HB. In the figure, we also show the least square fit to the data with a dotted line. The residuals around this fitted line will correct the temperature and the surface gravity effects on Σ(CaT) to the first order. As can be seen, the RGB stars in the *Ca-s* group have larger Σ(CaT) values at a given $V - V_{\rm HB}$ magnitude than those in the *Ca-w* group, consistent with our results that the *Ca-s* RGB stars are more calcium rich than the *Ca-w* RGB stars in M22.

4.2.3. Comparisons with Marino et al. (2009, 2011)

Finally, we make use of results from high resolution spectroscopy by Marino et al. (2011). In Figure 15, we show plots of the [Ca/H] versus [Fe/H] and the [Na/Fe] versus [O/Fe] for RGB stars in the *Ca-w* and the *Ca-s* groups. Similar to the results in Lee et al. (2009a,b), the plot of [Ca/H] versus [Fe/H] shows that the RGB stars in the *Ca-w* group have lower calcium and iron abundances than those in the *Ca-s* group, confirming that our *hk* index measures the calcium abundances of RGB stars in M22. The plot of [Na/Fe] versus [O/Fe] shows that each group based on our *hk* index exhibits its own Na-O anti-correlation. This was also pointed out by Marino et al. (2011), who found two separate Na-O anti-correlations in M22 RGB stars with different *s*-process elemental abundances. Note that the separation in the *hk* index in our current work is equivalent to that in *s*-process elemental abundances by Marino et al. (2011). These separate Na-O anti-correlations made Marino et al. (2011) to suggest that M22 may be composed of the merger of two clusters. In fact, NGC 1851 shows the similar behavior in the Na-O anti-correlations between the two distinct RGB populations. Carretta et al. (2010) suggested that the simple explanation for the observational evidences of NGC 1851 would be a merger scenario, preferentially in a dwarf galaxy environment.

---

[3] Lee et al. (2009a) showed that the differential reddening effect on the Ca II H and K lines across the cluster does not affect on the RGB split in M22. We demonstrated that, for example, the differential reddening effect of $\Delta E(B-V) \approx 0.3$ mag results in $\Delta Ca \leq 0.01$ mag, too small value to fully explain the RGB split in the *hk* index in M22.

However, it is worth emphasizing is the fact that the mean values of the *Ca-w* RGB stars appear to have a higher oxygen and a lower sodium abundances, representative of the primordial elemental abundance pattern, than the *Ca-s* RGB stars, consistent with the result by Marino et al. (2011). Also lighter elements C, N and heavy elements Ca and Fe abundances are different between the two groups (Marino et al. 2011). Therefore, the feedback on the overall chemical evolution between the two groups can not be completely neglected.

From comparisons of our *hk* photometry with three independent works by others, we conclude that our *hk* index measurements for RGB stars in M22 are very consistent with calcium abundance measurements by others from Ca II H and K, infrared Ca II triplet lines and visual Ca I lines. Therefore, the *hk* index can be securely and efficiently used to distinguish the difference in the calcium abundances at a given luminosity and furthermore the multiple RGB populations in GCs.

4.2.4. On the internal δCN vs δCH positive correlation

Lim et al. (2015) presented low resolution spectroscopy for M22 RGB stars and confirmed the CN-CH positive correlation discovered by Norris & Freeman (1983) (see also Anthony-Twarog et al. 1995).[4] Here, we discuss more about the metallicity effect on the CN-CH positive correlation between the two RGB groups in M22.

The variations in lighter elements in GC stars have been known for more than three decades, pioneered by Cohen (1978), and it is now generally believed to be rooted in the primordial origin (Cottrell & Da Costa 1981; Kraft 1994). The CN-CH anti-correlation is one of well-known characteristics in the Galactic GC system. One probable explanation for origin of this CN-CH anti-correlation can be found in Grundahl et al. (2002). They nicely demonstrated that there exist a CH-NH anti-correlation and a CN-NH positive correlation

[4]It is worth mentioning that Kayser et al. (2008) did not find any CN-CH positive correlation in M22. Examinations of their data led Pancino et al. (2010) to attribute this to low S/N ratios of spectra by Kayser et al. (2008) and the differential reddening effect. However, there is other possibility that the measurements by Kayser et al. (2008) may be not correct. For example the CH strength measurements by Kayser et al. (2008) are unlikely very large for their adopted definition of the CH strength from Harbeck et al. (2003), indicating that the results presented by Kayser et al. (2008) are suspected to be unreliable. Pancino et al. (2010) examined the δCN versus the δCH distribution using the data by Kayser et al. (2008), finding neither a positive correlation nor an anti-correlation, contradictory to the results by Norris & Freeman (1983) or by Lim et al. (2015).

among RGB stars in NGC 6752, suggesting that the nitrogen abundance is inversely correlated with the carbon abundance.

The CN-CH positive correlation shown in Figure 13 of Lim et al. (2015) appears to show two separate CN-CH anti-correlations among stars in each group at a first glance. It would have been very surprising if there exists a single CN-CH anti-correlation between the *Ca-w* and the *Ca-s* groups in M22. It is thought that a CN-CH positive correlation superposed on two separate CN-CH anti-correlation in M22 can be expected naturally if M22 is composed of two groups of stars with heterogeneous metallicities. It is because the positive correlation in the δCN versus δCH relation can occur when one compares the δCN and the δCH of different groups of stars with heterogeneous metallicities (see Norris et al. 1981, for the definition of δCN and δCH).

In order to investigate the metallicity effect on the positive correlation between the CN and CH band strengths, we used the homogeneous measurements of the CN and CH band strengths for stars in 8 GCs observed in the course of Sloan Digital Sky Survey (SDSS) by Smolinski et al. (2011). Since they provided magnitudes of stars in the SDSS photometric system, we converted their SDSS photometry to the Johnson system using the relation given by Jester et al. (2005),

$$V = g - 0.59(g - r) - 0.01, \tag{2}$$

and we calculated the $V - V_{\rm HB}$ using the $V_{\rm HB}$ values given by Harris (1996).

In Figure 16, we show distributions of the CN(3839) and the CH(4300) indexes against $V - V_{\rm HB}$ for 8 GCs. As shown, the CH(4300) strengths are well correlated with the metallicity of GCs at a given magnitude (for example, the RGB stars around the level of the HB magnitude shown with vertical dashed lines), while the CN(3839) strengths exhibit rather weak correlation against metallicity mainly due to the multi-modal distributions of the CN(3839) strengths of individual GCs (for example, see Figure 4 of Smolinski et al. 2011). Also shown are M22 and NGC 288 from Lim et al. (2015), whose measurements do not agree with those of Smolinski et al. (2011) due to heterogeneous definition of the band strengths between the two works. Note that Smolinski et al. (2011) used the definition of the CN(3839) band strength by Norris et al. (1981) for RGB and SGB stars, that by Harbeck et al. (2003) for MS stars and the definition of the CH(4300) band strength by Lee (1999), while Lim et al. (2015) used the definitions by Harbeck et al. (2003) for both bands. As a consequence of heterogeneous definition of the molecule band strengths, the extent of the CN(3839) band strengths for M22 and NGC 288 by Lim et al. (2015) is greater than those by Smolinski et al. (2011). Also, the CH(4300) values for M22 and NGC 288 by Lim et al. (2015) are $\gtrsim 1.0$ and they are out of range in the figure. Therefore, a direct comparison between the two works is not feasible.

In the figure, the thick solid lines are the common lower envelopes for 8 GCs. Due to the difference in the mean metallicity among GCs, these common lower envelopes may not correct both the temperature and the surface gravity effects simultaneously on the CN(3839) and the CH(4300) band strengths for 8 GCs. This is exactly what expected to happen when one compares two groups of RGB stars in M22 with different mean metallicities using a single fitted line, since the two groups of RGB stars in M22 have very different metallicities. In Figure 17, we show the distributions of the δCN and the δCH against metallicity, where the δCN and the δCH are defined to be the differences in the CN and CH between individual stars and the common lower envelopes. As expected from Figure 16, the δCN and the δCH have substantial gradients against metallicity, 0.169 ± 0.031 and 0.077 ± 0.010 mag/dex, respectively. It is believed that these positive slopes are the source of the CN-CH positive correlation when one compares the δCN and the δCH of stars with heterogeneous metallicities.

In Figure 18, we show the CN(3839) and the CH(4300) band strengths by Lim et al. (2015) against V magnitude. Also shown are the lower envelops for the *Ca-w* (the blue dotted line) and the *Ca-s* (the red dotted line) groups. Stars with $-1.0 \leq V - V_{\rm HB} \leq 0.5$ mag are shown with plus signs (*Ca-w*) and crosses (*Ca-s*). Note that the lower envelope for the *Ca-w* group can be served as the common lower envelope for both groups.

Figure 19-(a) shows a distribution of the δCN versus the δCH of M22 RGB stars, where the δCN and the δCH are calculated with respect to the common lower envelope (i.e. the blue dotted lines in Figure 18). This plot is similar to Figure 13 of Lim et al. (2015), where the CN-CH positive correlation can be seen. Noted that Lim et al. (2015) used the mean fitted line, not the lower envelope used in this analysis or those of others (for example Norris et al. 1981; Kayser et al. 2008; Smolinski et al. 2011) and detailed distributions of individuals stars are slightly different from those presented here.

In Figure 19-(b) and (c), we show distributions of the δCN versus δCH for the *Ca-w* and the *Ca-s* groups using their own lower envelopes. Each plot appears to show its own CN-CH anti-correlation, a well-known characteristics of normal GCs. This is also consistent with the presence of the separate C-N anti-correlations in each of the two *s*-process groups (Marino et al. 2011). Since its own lower envelope for each group can correct the metallicity effects, the δCN and the δCH values calculated from its own lower envelope reflect the relative CN and CH band strengths at a given metallicity and surface gravity. As a consequence, the CN-CH positive correlation with an apparently ambiguous origin disappears. In this regards, the most simplest explanation would be a merger of two GCs with different metallicities. Each group of stars could have been chemically enriched independently and exhibits its own CN-CH anti-correlation as observed in normal GCs in our Galaxy.

Finally, it is worth pointing out again that the extents in the δCN and the δCH of M22 using the data by Lim et al. (2015) are greater than those can be expected from the slopes in the metallicity gradients as shown in Figure 17. This is partially due to the different definitions in the CN and the CH band strengths. It would be highly desirable to re-analyze spectra in a homogeneous manner in the future.

4.2.5. Spread in nitrogen abundances

Yong et al. (2008) investigated nitrogen abundances of RGB stars in NGC 6752 using NH molecule lines. They noted that Strömgren u passband contains the NH molecule band at λ 3360 Å and they showed that the c_1 index are correlated with the nitrogen abundances of individual stars. They devised an arbitrary empirical index cy [$= c_1 - (b-y)$] and derived a well correlated relation between the nitrogen abundance and the cy index of RGB stars at about $V_{\rm HB}$ of NGC 6752, [N/Fe] $\propto 16.11 \times cy$.

In Figure 20, we show cy versus V CMDs of M22 RGB stars, showing broad spreads in the cy index in both groups. Assuming Gaussian distributions, we calculated the standard deviation around the mean cy values and obtained $\sigma(cy) \approx 0.03$ mag at $V_{\rm HB}$ for both groups of stars in M22. Since the metallicity of M22 is comparable to that of NGC 6752 and if the spread in the NH absorption strengths in individual RGB stars is solely responsible for the spreads in the cy index, $\sigma(cy) \approx 0.03$ mag corresponds to σ[N/Fe] ≈ 0.5 dex in each group of stars.

Note that our photometric estimate of the spread in the nitrogen abundances in M22 RGB stars appear to be slightly larger than those of Marino et al. (2011), who obtained σ[N/Fe] ≈ 0.2 dex for their s-poor and s-rich groups based on the observations of 14 stars.

One of the remarkable features can be seen in Figure 20 is that the RGB bump magnitudes of both populations appear to be different. In the right panel of Figure 20, we show the cumulative luminosity functions (LFs) for the Ca-w and the Ca-s populations. We show the V magnitude levels of the RGB bump, V_{bump}, where the slope of the luminosity function changes abruptly, for each population by arrows. We obtained $V_{bump} = 13.91$ mag for the Ca-w population while 14.06 mag for the Ca-s population.

4.2.6. RGB bump magnitude: $V_{\rm bump}$ versus Δhk

Here, we explore more details on the RGB bump in M22. As already shown in the left panel of Figure 7, it can be seen that the V magnitude level of the RGB bump appears

to be positively correlated with the Δhk values of RGB stars at around $V \approx 14.0$ mag. Especially, due to its high stellar number density, the tilted V_{bump} magnitude level against Δhk for the *Ca-w* group is conspicuous, while the tilted HB structure in the *Ca-w* group cannot be seen in the *cy* versus V CMD as shown in Figure 20. It should be worth noting that neither this tilted V magnitude against Δhk in the *Ca-w* group nor the difference in the bump magnitude between the two groups can be explained by the differential reddening effect (see also, Lee et al. 2009a).

The difference in the mean Δhk values between the *Ca-w* stars with $\Delta hk < 0$ mag and those with $\Delta hk \geq 0$ mag at $V = 13.95$ mag is $\Delta hk = 0.04$ mag. Again, assuming that the conventional interstellar reddening law by Anthony-Twarog et al. (1991) is applicable, $E(hk) = -0.16 \times E(b-y) \approx -0.12 \times E(B-V)$, and that the differential reddening effect across the cluster is the main reason for showing a broad RGB sequence in the hk index, this 0.04 mag difference in the Δhk index can be translated into $A_V = -1.05$ mag, in the sense that the *Ca-w* RGB stars with $\Delta hk \geq 0$ mag should be about 1 mag brighter than those with $\Delta hk < 0$ mag. This is the opposite of what observed in M22. As shown in Figure 21, the V magnitude for the RGB bump of the *Ca-w* stars with $\Delta hk \geq 0$ mag is about 0.06 mag fainter than that of the *Ca-w* stars with $\Delta hk < 0$ mag (see also Figure 20). Also, if this 0.04 mag difference in Δhk is originated solely by the differential reddening across the cluster, not by the difference in the chemical compositions, the $(b-y)$ color of the *Ca-w* group should have been broadened by ≈ 0.25 mag. However the RGB sequence in M22 is not as broad as 0.25 mag as shown in Figure 4. Therefore, the difference in the RGB bump magnitude is not mainly due to differential reddening effect but due to the difference in chemical compositions.

It is well known that at a given age the RGB bump becomes fainter with increasing metallicity and with decreasing helium abundance, due to changes in the envelope radiative opacity (see for example, Cassisi & Salaris 2013). The fainter $V_{\rm bump}$ magnitude with increasing Δhk can be interpreted that Δhk increases with either increasing metallicity or decreasing helium abundance. One can quantitatively estimate the effect of metallicity and the helium abundance on the RGB bump luminosity (Bjork & Chaboyer 2006; Valcarce et al. 2012).

In their Table 2, Bjork & Chaboyer (2006) presented the absolute V magnitude of the RGB bump with metallicity and we obtained $\Delta M_{V,\rm bump}/\Delta$[Fe/H] ≈ 0.93 mag/dex for 13 Gyr. The effect of helium abundances on the RGB bump can be found in Valcarce et al. (2012). From their Figure 9, we obtained $\Delta m_{\rm bol} \approx 2.5 \times \Delta Y$ for the isochrones with $Z = 1.6 \times 10^{-3}$ and 12.5 Gyr. If the 0.06 mag spread in the RGB bump magnitude in the *Ca-w* group is solely due to metallicity, one expects to see the spread in metallicity by Δ[Fe/H] ≈ 0.06

dex. Similarly the 0.15 mag difference between the *Ca-w* and the *Ca-s* groups can translate into Δ[Fe/H] $\approx$ 0.16 dex that agrees well with what Marino et al. (2011) obtained for the *s*-poor and the *s*-rich groups, Δ[Fe/H] $\approx 0.15 \pm 0.02$ dex. However, if we take into account the enhanced helium abundance for the *Ca-s* group by $\Delta Y \approx 0.09$ (Joo & Lee 2013), the RGB bump magnitude for the *Ca-s* group should be ≈ 0.08 ($= 0.23 - 0.15$) mag brighter than that for the *Ca-w* group, which is not the case for our observation. The formation of the EBHB stars, as progenies of the *Ca-s* RGB stars, may require the enhanced helium abundance but the difference in the RGB bump magnitude is difficult to explain in this scenario. Perhaps, may this suggest that only a fraction of the *Ca-s* RGB stars have been evolved into the EBHB?

4.3. Centers

With the bright RGB stars selected above, we measured the centers of each populations using three different methods; the arithmetic mean, the half-sphere and the pie-wedge methods.

Using the coordinate of the center of the cluster measured by Goldsbury et al. (2010) as an initial value (α = 18:36:23.94 and δ = $-$23:54:17.1; J2000) we chose RGB stars in each population within 300 arcsec from the center of the cluster and we calculated the mean values for each group. The half-light radius of M22 is about 200 arcsec (Harris 1996) and the circle with a radius of 300 arcsec can contain more than 70% of RGB stars in our sample. It is believed that using this radius is sufficient enough to derive the coordinate of the center of each group with decent accuracy.

We obtained the offset values with respect to the coordinate of center of the cluster by Goldsbury et al., (ΔRA, ΔDec) = ($3\farcs8$, $0\farcs4$) for the *Ca-w* group and ($0\farcs8$, $5\farcs6$) for the *Ca-s* group, resulted in an angular separation of 6 arcsec between the centers of both populations. Note that the core radius of the cluster is about 80 arcsec (Harris 1996), and the angular separation between the centers of the two populations is relatively small.

Similar to the simple mean calculation, we use the coordinate of the cluster by Goldsbury et al. as an initial value, we chose RGB stars in each population within 300 arcsec from the center of the cluster. Then we divided the sphere into two halves by assuming the radial symmetry in the distribution of RGB stars in M22. We compared the number of RGB stars between the two halves by rotating the position angle by 10 degree at a fixed coordinate of the center and we obtained the differences in the number of RGB stars between both halves. We repeated this calculation with varying coordinates of the center and we derived the coordinates of the

centers of each group with the minimum difference in the number of RGB stars between the two halves. We found (7.″5, 1.″6) for the *Ca-w* group and (−1.″4, −1.″4) for the *Ca-s* group, slightly different from those from the simple mean method. The angular separation between the two groups is about 9 arcsec and, again, it is relatively small compared the core radius of the cluster.

Finally, we applied the pie-wedge method. Using the coordinate by Goldsbury et al. (2010), we divided the sphere of a radius of 300 arcsec into 12 different slices. Then we compared the number of stars in the opposing distribution. We repeated this calculation with varying coordinates of the center and obtained the center of each population with the minimum differences. We found (7.″7, −2.″8) for the *Ca-w* group and (−4.″9, 6.″5) for the *Ca-s* group. Again, the angular separation between the two groups is about 16 arcsec and it is still relatively small compared with the core (≈ 80 arcsec) or the half-light (≈ 200 arcsec) radii of the cluster.

We show our results in Table 5 and Figure 22. We conclude that the coordinates of the centers of each population are slightly different. However the differences in the coordinates of the center from various methods do not appear to be substantially large to claim that the centers of the RGB distributions of two populations are distinctively different.

4.4. Spatial Distributions

4.4.1. Red giant branch stars

In Figure 23, we show the number ratios of RGB stars in the *Ca-s* group to those in the *Ca-w* group against the radial distance from the center using the coordinate of the center by Goldsbury et al. (2010). It is worth noting that there appears to exist a weak gradient of the number ratio between the two populations against the radial distance from the center, indicating that the distribution of the *Ca-w* group is slightly more centrally concentrated. However, the difference in the mean number ratio are in agreement within the measurement errors from the central part of the cluster up to ≈ 800 arcsec from the center, about four times of the half-light radius of M22, similar to that can be seen in NGC 1851. Milone et al. (2008) showed that the number ratio between the two distinctive populations in NGC 1851 does not appear to vary up to 1.7 arcmin from the center, which is about 2 times of the half-light radius of the cluster.[5] The flat number ratio between the multiple populations

[5] Carretta et al. (2011) claimed that the metal-poor RGB population in NGC 1851 is more centrally concentrated than the the metal-poor population from the incomplete sample of their spectroscopic study

in M22 and NGC 1851 is in sharp contrast with that in ω Cen. Bellini et al. (2009) found that both intermediate-metallicity and the metal-rich RGB populations are more centrally concentrated than the metal-poor RGB population in ω Cen (see also Sollima et al. 2007).

The relaxation time at the half-mass radius for ω Cen is about 10 Gyr (Harris 1996) and it is substantially large that the later generation of stars in ω Cen may not have sufficient time to be homogenized completely. As a consequence, the later generation of stars fails to achieve similar radial distribution as the early generation of stars in the cluster. On the other hand, the relaxation times at the half-mass radius for M22 and NGC 1851 are about 1.7 Gyr and 0.7 Gyr, respectively, significantly smaller than that of ω Cen. If the second generation of stars in M22 and NGC 1851 formed from gaseous ejecta expelled from the first generation of stars, they might have enough time to become relaxed systems. In this regard, Decressin et al. (2008) claimed that stars initially centrally concentrated toward the center need about the two relaxation times to achieve a completely homogenization throughout the cluster and any radial difference among multiple stellar populations would be erased over the dynamical history of old GCs.[6] However, it is also possible that the merger of two GCs can maintain a flat RGB number ratio in M22.

We show a comparison of cumulative distributions of RGB stars in both groups in the lower panel of Figure 23. As can be seen, the radial distribution of RGB stars in the *Ca-w* group is slightly more centrally concentrated. We performed a Kolmogorov-Smirnov (K-S) test and we found the probability of being drawn from identical populations is 0.1%, with a K-S discrepancy of 0.10, indicating that they have different parent populations. As we have demonstrated earlier, the difference in the radial distribution is not likely due to the field star contamination.

Although small, the difference in the distributions of RGB stars is difficult to understand within the current theoretical framework of the GC formation. If the second generation of stars formed out of gas expelled from the first generation of stars in the central part of the cluster (Bekki 2010, see for example), the second generation of stars should have a more centrally concentrated distribution in the early history of the cluster. Also importantly, if the complete homogenization had been achieved within a couple of relaxation times, the two different populations in M22 are expected to have indistinguishable radial distributions.

---

with larger radial distance from the center, $\approx$ 12 arcmin.

[6] The work of Vesperini et al. (2013) is also worth mentioning. They performed N-body numerical simulations and showed that the time required to have a flat number ratio between the first and the second generations can be larger than 45 half-mass relaxation time for their $r10$ system, where $r10$ refers the ratio between the two half-mass radii (see their Figure 7).

We speculate that the difference in the radial distributions of RGB stars may suggest that either (or perhaps both) of followings is correct; (i) The *Ca-s* population did not form out of the gaseous ejecta of the first generation of stars. Or, (ii) the complete homogenization may require much longer time scale than that proposed by Decressin et al. (2008). In this regard, the merger of two GCs can naturally explain the observed radial distributions of RGB stars.

We turn our attention to the spatial distributions of RGB stars in both groups. In the top panel of Figure 24, we show the projected spatial distributions of RGB stars in the *Ca-w* and the *Ca-s* groups in M22. In the Figure, the offset values of the projected right ascension and the declination in the units of arcsec were calculated using the transformation relations in van de Ven et al. (2006),

$$\begin{aligned} \Delta RA &= \frac{648000}{\pi}\cos\delta\sin\Delta\alpha, \\ \Delta Dec &= \frac{648000}{\pi}(\cos\delta\cos\delta_0 - \cos\delta\sin\delta_0\cos\Delta\alpha), \end{aligned} \tag{3}$$

where $\Delta\alpha = \alpha - \alpha_0$ and $\Delta\delta = \delta - \delta_0$, and α_0 and δ_0 are the coordinate of the center. For our calculations, we adopted the coordinate for the cluster center measured by Goldsbury et al. (2010).

In the lower panel of the Figure, we show smoothed density distributions of RGB stars along with iso-density contours for each population. For the smoothed density distribution of each population, we applied a fixed Gaussian kernel estimator algorithm with a FWHM of 70 arcsec (Silverman 1986). We show the FWHM of our Gaussian kernel in the lower left panel of the figure. To derive the iso-density contour for each population, we applied the second moment analysis (Dodd & MacGillivary 1986; Stone 1989). In the Figure, we show the iso-density contour lines for 90, 70, 50, and 30% of the peak values for both populations.

At a glance of the figure, the distribution of the *Ca-s* group appears to be more spatially elongated than that of the *Ca-w* group does. In Table 6, we show the axial ratio, b/a, and the ellipticity, e $(= 1 - b/a)$, and we show radial distributions of the axial ratio and the ellipticity of the *Ca-w* and the *Ca-s* groups in Figure 25. As shown, the radial distributions for both groups agree rather well up to $\approx$ 130 arcsec ($\approx$ 1.5 core radii of the cluster) from the center but two distributions bifurcate at the larger radial distance, in the sense that the *Ca-s* group is more elongated.

4.4.2. Horizontal branch stars

In recent years, the nature of the multiple stellar populations of the HB stars in GCs has been emerged through the detailed spectroscopic studies (e.g. Marino et al. 2013, 2014a; Gratton et al. 2014). Marino et al. (2013) studied 7 HB stars in M22 and they found that all their HB stars are Ba-poor and Na-poor, equivalent to the *s*-poor RGB population, leading them to suggest that the position of a HB star is strictly related to the chemical composition. More recently, Gratton et al. (2014) investigated the chemical compositions of more than 90 HB stars in M22, using the multi-object spectroscopy facility. Their results showed that there appears to exist 3 different groups of HB stars in M22. However, they did not find any severely O-depleted HB stars. They claimed that the progeny of the severely O-depleted RGB stars may evolve into the hotter part of the HB, where the surface temperature of these HB stars are beyond the temperature range of their sample.

In addition to metallicity and age, it is generally believed that the HB morphology of GCs can be governed by the helium abundances (e.g. D'Antona et al. 2002; Joo & Lee 2013; Milone et al. 2014) and there also exist direct spectroscopic observational evidences of helium enhancement in GC HB stars (Marino et al. 2014a; Gratton et al. 2014).

In their recent work, Joo & Lee (2013) investigated M22 HB populations using the synthetic population models. Although simplistic, they divided M22 HB populations into two groups, the BHB and the EBHB, and they delineated a connection between the RGB and the HB of M22 (see their Figure 13). Here, we explore more details on the number ratio and the spatial distribution of the HB populations in M22 using our wide field data. Note that the *hk* index is not an useful tool to study the BHB or the EBHB stars, since the Ca II H and K lines become suppressed and the absorption strength of H_ϵ at λ 3970 Å reaches its maximum at A0 and can contaminate the adjacent Ca II H line at the high effective surface temperature of BHB or EBHB stars.

In Figure 26, we shows CMDs of the HB region of M22. As for the RGB populations, we used all available multi-color information in order to remove the contamination from the off-cluster field star population in our study. Also shown in the figure is the cumulative LF of the HB stars, where the slope in the cumulative LF of HB stars becomes briefly zero at the location of the HB gap at $V = 15.97$ mag. This magnitude is about the same magnitude level that Joo & Lee (2013) separated the BHB and the EBHB populations in M22. Furthermore, Joo & Lee (2013) claimed that the BHB stars are the first generation of stars (corresponding to the progeny of the *Ca-w* RGB population in our notation), while the EBHB stars the second generation of stars (the *Ca-s* population) of the cluster.

In our photometric data, the observed number ratio between the BHB and the EBHB

stars becomes n(BHB):n(EBHB) = 80:20 ($\pm$ 9), marginally in agreement with those of the RGB populations, $n(Ca\text{-}w)$:$n(Ca\text{-}s)$ = 69:31 ($\pm$ 3), and the SGB populations, n(bSGB):n(fSGB) = 69:31 ($\pm$ 6), without the correction for the evolutionary effects. With the correction of the evolutionary effect, the HB number ratio does not agree with that of SGB, n(bSGB):n(fSGB) = 62:38 ($\pm$ 6). Note that our HB number ratio includes the completeness correction that shown in Figure 3. We calculated the average completeness fraction as a function of V magnitude using those from the central and outer part of the cluster as shown in Figure 3, and we applied the correction factor to individual HB stars by interpolating the average completeness fraction against V magnitude. As discussed above, our photometry is complete down to $\approx$ 18.5 mag. Therefore, only the the EBHB population is insignificantly affected ($\approx$ 0.6 %) by the completeness correction.

In the upper panel of Figure 27, we show the number ratios of the EBHB to the BHB populations against the radial distance from the center. Although, the HB number ratios against the radial distance are in agreement within measurement errors up to $\approx$ 3 times of the half-light radius of the cluster, the mean HB number ratio appear to have a weak gradient against the radial distance in the sense that the BHB stars are slightly more centrally concentrated than the EBHB stars, similar that can be seen in the RGB stars in Figure 23. In the bottom panel of the figure, we show the cumulative distributions of the BHB and the EBHB populations against the distance from the center. The BHB population is more centrally concentrated than the EBHB population, qualitatively consistent with that can be seen in the RGB populations. The K-S test indicates a probability of 1.8% that two HB populations are drawn from the same parent population, suggesting that they have different parent populations as can be seen in the RGB stars.

As have done for the RGB and SGB populations, due to different masses and chemical compositions, different lifetimes of individual HB stars should be taken into account. We compared the lifetimes between the BHB and the EBHB populations using the HB tracks by Joo & Lee (2013) and obtained the correction factor in terms of the number of HB stars, n(BHB):n(EBHB) = 56.5:43.5 ($\pm$ 4.0). Because the EBHB stars live longer, one naturally expects to observe a larger number of EBHB stars if initially even numbers of stars are distributed both on the BHB and on the EBHB locations.

In addition, the number of HB stars evolved from the $Ca\text{-}w$ and the $Ca\text{-}s$ RGB populations will be slightly different since the RGB-tip masses between the two groups will be different. If the $Ca\text{-}s$ population has the higher helium abundance by $\Delta Y = 0.09$ (Joo & Lee 2013), the evolution of stars in the $Ca\text{-}s$ population would be faster than those in the $Ca\text{-}w$ population due to increasing mean molecular weight, resulted in smaller RGB-tip masses in the $Ca\text{-}s$ population. With the HB mass dispersion adopted by Joo & Lee (2013), σ_M

$= 0.023 M_{\odot}$ for both populations, we calculated the number of stars within $4\times\sigma_M$ from the RGB-tip masses[7] of both isochrones using the same evolutionary population synthesis model that we constructed previously. For this purpose, we populated 10^7 artificial stars in each group using the Salpeter's IMF and we generated 50 different sets for both groups. We obtained the correction factor, n(BHB):n(EBHB) = 58.9:41.1 ($\pm$ 0.1), in the sense that the observed number of HB stars that evolved from the *Ca-s* population gets larger since the RGB-tip mass of the *Ca-s* is smaller owing to its faster evolution from the MS through the RGB phases. If we take these effects into consideration, the number ratio between the BHB and the EBHB stars becomes n(BHB):n(EBHB) = 88.2:11.8 ($\pm$ 9.8), significantly different from those of the RGB and the SGB populations. It should be noted that this result is based on the assumption that the BHB stars are the progeny of the *Ca-w* RGB stars while the EBHB stars are the progeny of the *Ca-s* RGB stars as proposed by Joo & Lee (2013).

Our result may suggest that the connection between the RGB and HB populations may not be as clear as that Joo & Lee (2013) claimed. Note that Joo & Lee (2013) adopted the number ratio between the BHB and EBHB of 70:30 in their synthetic HB model construction and they claimed that their HB number ratio does not disagree with the previous estimates of RGB or SGB number ratios between the two populations by others. It is thought that Joo & Lee (2013) overestimated the EBHB fraction in their calculation compared to our observation. As Joo & Lee (2013) suggested, if the EBHB population is the only progeny of the second generation of the RGB population (i.e. the *Ca-s* population), the discrepancy in the number ratios between the two populations in the HB and SGB/RGB is difficult to explain. For instance, it is evident that the R value, the number ratio of the HB to the RGB stars (Caputo et al. 1987), of each population is against the theoretical expectation. The observed R value of a simple stellar population is the measure of the helium abundance in the sense that the R value increases with the helium abundance. We define the modified R value which includes RGB stars from $V_{\rm HB}$ (= 14.15 mag for M22) to 12.0 mag (not the tip of the RGB sequence), since we already selected bright RGB stars with 12 mag $\leq V \leq$ 16.5 mag in both populations as discussed above. Then we have the modified R values of 1.73 $\pm$ 0.14 for for the BHB versus the *Ca-w* RGB populations and 1.21 $\pm$ 0.17 for the EBHB versus the *Ca-s* RGB populations. If the EBHB and the *Ca-s* RGB populations are the second generation of the stars in the cluster and they formed out of interstellar gas enriched in helium by the first generation of stars, one would naturally expect to have a larger R value for the EBHB and the *Ca-s* RGB populations. However, the observed R value for the EBHB and the *Ca-s* RGB populations is smaller than that for BHB and the *Ca-w* RGB

[7]This mass range is rather arbitrary, but the final result does not significantly depend on the adopted mass range if the same mass dispersions for both groups are maintained.

populations and the observe R values are opposite of the theoretical expectation. Our result may suggest that, like other lighter elemental abundances, there may exist a spread in the helium abundance of the second generation of stars and at least about the half of the *Ca-s* RGB stars must have evolved into the BHB sequence (which requires no or little helium enrichment) and a significant fraction of the *Ca-s* RGB stars failed to become EBHB stars (which requires the helium enrichment of $\Delta Y \approx 0.09$, see Joo & Lee 2013) in M22.

It would be very interesting to point out the recent result by Gratton et al. (2014). They carried out the spectroscopic survey of the BHB stars in M22 and found a significant fraction ($\approx 18\%$) of the metal-rich helium-enhanced BHB stars in their sample (Group 3 designated by Gratton et al.). If we consider that the Group 3 BHB stars by Gratton et al. (2014) are the progeny of the *Ca-s* RGB stars, the number ratio between the second generation and the first generation of HB stars becomes 34:66 and this number ratio is in good agreement with those from the RGB and the SGB stars. Perhaps, this is also hinted by the separate Na-O distribution of M22 RGB stars, indicative of internal He spread in both the *Ca-w* and the *Ca-s* groups. If so, the *Ca-s* population of M22 may be exactly what we observe in NGC 6752, which contains both the BHB and the EBHB populations maintaining a rather monotonous metallicity distribution.

4.5. Radial velocity and velocity dispersion

Recently, Lane et al. (2009) performed a wide-field spectroscopic survey of bright RGB stars in M22 using AAOmega mounted on the 3.9-m Anglo-Australian Telescope. Their primary concern was to test Newtonian gravity by investigating velocity profiles of several globular clusters, including M22, at larger radii. We made use of their radial velocity data, which were kindly provided by Dr. Kiss, in order to investigate the differences in kinematics of the multiple stellar populations in M22.

We compared our coordinates of *Ca-w* and *Ca-s* RGB stars with those of Lane et al. (2009) and we selected common stars matched within a radius of $2''$. During our source matching process, we excluded stars having uncertainties in the radial velocity measurement larger than 10 km s^{-1} tagged by Lane et al. (2009). Through this process, we have 208 *Ca-w* and 87 *Ca-s* RGB stars.

We show the radial velocity of individual stars in each group against the radial distance from the center in the upper panel of Figure 28. We obtained the mean radial velocity of the cluster, $\langle v_r \rangle = -144.89 \pm 6.76$ km s^{-1}. The distributions of the radial velocity between the two populations are in good agreement. Also the distribution of the radial velocity of

each population does not vary with the radial distance from the center.

Using these stars, we calculate the average radial velocities and velocity dispersions for *Ca-w* and *Ca-s* groups as given by Pryor & Meylan (1993), assuming that each velocity v_i is drawn from the normal distribution,

$$f(v_i) = \frac{1}{\sqrt{2\pi(\sigma_c^2 + \sigma_{e,i}^2)}} \exp\left[-\frac{(v_i - v_r)^2}{2(\sigma_c^2 + \sigma_{e,i}^2)}\right], \quad (4)$$

where $\sigma_{e,i}$ is the known measurement uncertainty of v_i and v_r, σ_c are the average radial velocity and the intrinsic velocity dispersion of each group. For our calculations, we used a FORTRAN program kindly provided by Prof. Pryor, obtaining $v_r = -144.59 \pm 0.40$ km s^{-1} and $\sigma_v = 4.71 \pm 0.35$ km s^{-1} for the *Ca-w* group and $v_r = -145.77 \pm 0.89$ km s^{-1} and $\sigma_v = 7.55 \pm 0.66$ km s^{-1} for the *Ca-s* group. Our results are shown in the bottom panel of Figure 28. The mean velocities of both groups are in good agreement, while the velocity dispersion for the *Ca-s* group appears to be slightly larger than that of the *Ca-w* group. Note that Marino et al. (2014b) studied the velocity dispersions between the two SGB in NGC 1851 and they did not find any difference.

4.6. Projected Rotations

Peterson & Cudworth (1994) first found a clear evidence of the rotation of M22 from both proper motions and radial velocities of bright stars in the cluster, with the amplitude of the mean rotation of about from ≈ 6 km s^{-1} for $1' \leq r \leq 3'$ to ≈ 3 km s^{-1} for $3' \leq r \leq 7'$. Their result is an unique example of obtaining the rotational velocity of GCs using proper motion data. Later Lane et al. (2009, 2010) confirmed that M22 has a substantial rotation among other GCs that they studied. In this section, we investigate the mean rotation of RGB stars of the double populations in M22 using three methods.

4.6.1. Radial velocity versus position angle

First, we estimated the mean rotation of the cluster by using the radial velocity distribution against the position angle of individual stars (Peterson & Cudworth 1994). In Figure 29, we show radial velocities of individual stars in each group against their position angles measured from North. We chose the RGB stars[8] with the proper motion member-

[8]Peterson & Cudworth (1994) also studied the HB stars in the cluster, of which we do not make use in this study. Therefore, the mean velocity of the cluster and the number of stars being used in this study are

ship probability larger than 90% from Peterson & Cudworth (1994) and we merge their radial velocity measurements with our photometric data. We show radial velocities from Peterson & Cudworth (1994) against the position angle for individual RGB stars in Figure 29-(a). We performed a sinusoidal fit to the data and we obtained the amplitude of the mean rotation of all RGB stars is about 4.2 km s^{-1} which is comparable to that from Peterson & Cudworth (1994), 3.8 km s^{-1} (Meylan & Heggie 1997).

Next, we investigate the mean rotational velocity of the *Ca-w* and the *Ca-s* groups. We divided RGB stars from Peterson & Cudworth (1994) into two groups based on the *hk* index of individual stars in Figure 7 and we show plots of radial velocities against the position angle of RGB stars in the *Ca-w* and the *Ca-s* groups in Figure 29-(b) and -(c). The amplitude of the sinusoidal fit to the *Ca-w* group is about 3.6 km s^{-1}, while that to the *Ca-s* group is about 5.6 km s^{-1}. The amplitude of the projected rotation of the *Ca-s* group is larger than that of the *Ca-w* group.

We carried out the same procedure using the radial velocities by Lane et al. (2009). As shown in the bottom panels of Figure 29, similar results can be found from the radial velocity data by Lane et al. (2009), although the mean radial velocities and the amplitudes of the mean rotation are different from those from Peterson & Cudworth (1994). We obtained the amplitude of mean rotation for the *Ca-w* group is about 1.5 km s^{-1}, while that for the *Ca-s* group is about 3.6 km s^{-1}. Again, the amplitude of the mean rotation for the *Ca-s* group is larger than that for the *Ca-s* group.

It should be noted that the difference in the mean radial velocities of the cluster using the data from Peterson & Cudworth (1994), -149.1 km s^{-1}, and Lane et al. (2009), -144.6 km s^{-1}, may suggest that two sets of radial velocity data are heterogeneous. Therefore, we did not attempt to merge two sets of data together to investigate the rotation of the cluster. The amplitude of the mean rotation using the data by Lane et al. (2009) is smaller than that by Peterson & Cudworth (1994). Since the number of RGB stars being used is smaller for the case of using data by Peterson & Cudworth (1994), it is suspected that a few stars with large deviations from the mean velocity can affect the results. In the upper panel of Figure 29, the radial velocities of three RGB stars deviate more than 3 σ level from the mean value; IV-20 (-166.78 km s^{-1}), 2-73 (-127.65 km s^{-1}), and I-27 (-127.51 km s^{-1}). If we exclude these three stars in our calculations, the amplitudes of the mean rotations become 2.7 km s^{-1}, 2.5 km s^{-1} and 3.3 km s^{-1} for all RGB stars, the *Ca-w* and the *Ca-s* groups, respectively. These values become comparable to those using data from Lane et al. (2009).

---

different from those in Peterson & Cudworth (1994).

4.6.2. Radial velocity difference between two hemispheres

Next, we estimated the amplitude of the mean rotation of the cluster using the method described by Lane et al. (2009). Assuming an isothermal rotation, the mean rotation can be measured by dividing the cluster in half at a given position angle and calculating differences between the average velocities in the two halves. We repeated this calculation by increasing the position angle of the boundary of the two halves by 10°. Then the net rotation velocity is the half of the amplitude of the sinusoidal function in the differences between the average velocities in the two halves.

We show the differences in the mean radial velocities as a function of the position angle (East = 0° and North = 90°) along with the best-fitting sine function in Figure 30. Our result for all RGB stars in the cluster is shown in the top panel of the figure. We obtained the mean rotation velocity of 1.4 ± 0.3 km s^{-1} and the position angle of the equator (i.e. the axis perpendicular to the rotation axis) of the rotation of 81° (i.e. ≈ North), which are very consistent with those of previous studies by Lane et al. (2009, 2010), 1.5 ± 0.4 km s^{-1} and approximately North-South, respectively.

In the middle and the bottom panels of Figure 30, we show plots of differences in the mean radial velocities for the *Ca-w* and the *Ca-s* groups. We obtained the mean rotation of 1.0 ± 0.4 km s^{-1} with the position angle of 86° for the *Ca-w* group and 2.5 ± 0.8 km s^{-1} with the position angle of 73° for the *Ca-s* group. Again, the amplitude of the mean rotation of the *Ca-s* group is slightly larger than that of the *Ca-w* group is.

Note that the mean rotations of this method are smaller than those of the sinusoidal fit to individual stars on the radial velocity versus position angle. As we have demonstrated above, the sinusoidal fit to the individual stars suspects to be vulnerable to stars with large velocity deviations from the mean value. This may explain the difference in the amplitudes of the mean rotation between the two methods.

4.6.3. Radial velocity profile

Finally, we examine the rotation of the cluster by using the radial velocity profile along the axis perpendicular to the mean rotation. In the top panel of Figure 31, we show the distributions of RGB stars in the *Ca-w* and *Ca-s* groups with the radial velocity measurements. In the figure, blue and red colors denote blue-shift and red-shift from the mean radial velocity of the cluster, respectively, and the size of each circle represents the velocity deviation from the mean value of the cluster. We also show grids for calculating the group velocity and the velocity dispersion with rectangles with the width of 800 arcsec and the

height of 100 arcsec. We adopt the tilted angle of the grid rectangles that we obtained in §4.6.2, 89° for the *Ca-w* group and 64° for the *Ca-s* group.

We calculated the the mean radial velocity and the velocity dispersion in each grid rectangle. Our results are shown in the bottom panels of Figure 31. Inside the half-radius of the cluster, the velocity dispersion of the *Ca-s* population appears to be slightly larger, consistent with our previous result presented in §4.5. Also, the radial velocity profile against the projected distance perpendicular to the rotation axis are different.

We performed a least square fit to the line of sight velocity versus the projected distance perpendicular to the rotation axis. We found that the maximum velocity of 1.0 km s^{-1} for the *Ca-w* group and 4.3 km s^{-1} for the *Ca-s* group at the half-light radius of the cluster. Again, the RGB stars in the *Ca-s* group appear to rotate faster than those in the *Ca-w* group do, consistent with our previous results.

We examined the anisotropy parameter of the cluster (see, for example, Bender et al. 1991),

$$\left(\frac{V_{\rm rot}^{\rm max}}{\sigma_{\rm m}}\right)^{*} = \left(\frac{V_{\rm rot}^{\rm max}}{\sigma_{\rm m}}\right)\sqrt{(1-e)/e} \tag{5}$$

where $\sigma_{\rm m}$ is the mean velocity dispersion and e is the ellipticity of the cluster. Note that $(V_{\rm rot}^{\rm max}/\sigma_{\rm m})^{*} \ll 1$ indicate strong anisotropy. Using the relation above, we obtained the anisotropy parameter $(V_{\rm rot}^{\rm max}/\sigma_{\rm m})^{*} = 0.707$ for the *Ca-w* group and 1.62 for the *Ca-s* group, where we adopted $e = 0.074$, $V_{\rm rot}^{\rm max} = 1.0$ km s^{-1} and $\sigma_{\rm m} = 5.0$ km s^{-1} for the *Ca-w* group and $e = 0.106$, $V_{\rm rot}^{\rm max} = 4.3$ km s^{-1} and $\sigma_{\rm m} = 7.7$ km s^{-1} for the *Ca-s* group. For ellipticity, we used the simple mean of those given in Table 6 within about 210 arcsec from the center (i.e. about the half-light radius of the cluster). The large values of anisotropy parameters for both populations suggest that the flattening observed in M22 is most likely originated from the presence of internal rotation.

5. SUMMARY

We presented new wide-field ground-based *Ca by* photometry and the HST WFC3 photometry of the peculiar GC M22 (NGC 6656), confirming our previous results that M22 has a distinctive RGB split in the *hk* index, mainly due to the bimodal distribution in heavy elemental abundances, especially in calcium.

Our ground-based photometry is complete down to $V \approx 18.5$ mag both in the central and the outer part of the cluster and incompleteness at the fainter magnitude regime does not affect our results presented in this paper. Although M22 is located toward the Galactic

bulge, the contamination from the off-cluster field populations appears to be negligible when our cluster membership star selection scheme based on our multi-color photometry is applied.

Similar to our previous work (Lee et al. 2009a), we defined the *Ca-w* and the *Ca-s* RGB groups based on the *hk* index values at a given V magnitude. We obtained the apparent number ratio of $n(Ca\text{-}w)$:$n(Ca\text{-}s)$ = 69:31 ($\pm$ 3), without the correction for the differential evolutionary effects due to the heterogeneous elemental abundances and slightly different ages between the two groups (Marino et al. 2011; Joo & Lee 2013). After applying such correction, the intrinsic or the true number ratio becomes $n(Ca\text{-}w)$:$n(Ca\text{-}s)$ = 70:30 ($\pm$ 3).

Using the HST/WFC3 data of the central part of the cluster, we obtained the apparent SGB number ratio of n(bSGB):n(fSGB) = 69:31 ($\pm$ 6) without the correction for the differential evolutionary effects and the true SGB number ratio of 62:38 ($\pm$ 6) with the correction, which is in excellent agreement with previous result from the HST observations in other passbands by Marino et al. (2009).

We showed that the RGB split in the $m1$ index in M22 is not mainly due to the difference in the CNO abundances, but in the heavy metal abundances. Remarkable resemblance in the HB morphology and the double RGB sequences both in the $m1$ and the *hk* indexes between M22 and the composite GC using M55 and NGC 6752 (each of which has similar metal abundances as the *Ca-w* and the *Ca-s* groups in M22) may support our idea. Therefore, it is thought that the origin of the RGB split in the $m1$ index in M22 is the same as that in the *hk* index: the difference in the mean heavy metal abundances.

Comparisons with the chemical abundance measurements of RGB stars from previous studies showed that the *hk* index indeed a measure of calcium abundance at a given luminosity. Our *hk* measurements are well correlated with Ca II H and K lines, infrared Ca II triplet lines and visual Ca I lines by others. Therefore, the *hk* index can provide an efficient means to distinguish the difference in the calcium abundance and furthermore the multiple populations in GCs and nearby dwarf spheroidal galaxies.

Using homogeneous CN and CH band strength measurements by Smolinski et al. (2011), we showed that the gradients in δCN and δCH against metallicity are naturally expected to occur, when the common lower envelope for GCs with heterogeneous metallicity is adopted. In this regard, we showed that the CN-CH positive correlation in M22 reported by Lim et al. (2015) is most likely due to metallicity effects between the two RGB groups with heterogeneous metallicities in M22. However, when corrected with its own lower envelope, each RGB group keeps maintaining its own CN-CH anti-correlation, showing a well-known characteristics of normal GCs. This may suggest that the merger of two GCs with different chemical compositions would be the most simplest explanation.

Our *cy* index measurements for each RGB group in M22 confirmed that there exists a significant spread in the nitrogen abundance among RGB stars in both groups. Quantitatively, the *cy* index appears to over-estimate the nitrogen abundance when compared with the results from the high-resolution spectroscopy by Marino et al. (2011).

We found that the mean RGB bump V magnitude, V_{bump}, of the *Ca-w* group is about 0.15 mag brighter than that of the *Ca-s* group, which is consistent with the idea that the difference in V_{bump} between the two groups is mainly due to the difference in metallicity. Furthermore, the tilted V_{bump} magnitude level against Δhk for the *Ca-w* group can be seen our data, suggesting that the hk index is indeed a good measure of metallicity and the RGB bump luminosity decreases with increasing metallicity. It is an widely accepted fact that the formation of the EBHB stars may require a helium enhancement (e.g. D'Antona et al. 2002). If the *Ca-s* group has an enhanced helium abundance by $\Delta Y = 0.09$ as Joo & Lee (2013) proposed, the brighter V_{bump} magnitude by $\Delta V = 0.08$ mag is expected for the *Ca-s* group. But this is not the case and the difference in the V_{bump} magnitude within the context of the enhanced helium abundance of the *Ca-s* group is difficult to explain.

With the carefully selected sample of RGB stars, we derived the coordinates of the center of both RGB populations using three different methods, finding insignificant differences in the coordinates of the center of both populations. The coordinates of the center of each group appear to be slightly different, but the difference is not substantially large to claim that the centers of two groups are distinctively different. On the other hand, the radial and spatial distributions between the two groups are different. The *Ca-w* group appears to be slightly more centrally concentrated while the number ratio between the *Ca-w* and the *Ca-s* groups are almost flat within the measurement errors up to $\approx 3 - 4$ half-mass radii, a reminiscence of the peculiar GC NGC 1851. The spatial distribution of the *Ca-s* group is very similar as that of the *Ca-w* group up to ≈ 1.5 core radii, while the more elongated spatial distribution of the *Ca-s* group at larger radii can be seen.

The similarity and the difference between the RGB and the HB populations could be the critical puzzle to understand the formation of the EBHB stars. The BHB stars in M22 are thought to be the canonical progeny of the metal-poor *Ca-w* RGB population with a normal helium abundance while the EBHB stars are thought to be that of the metal-rich *Ca-s* RGB population with an enhanced helium abundance (Joo & Lee 2013). Our result showed that the BHB population is more centrally concentrated than the EBHB population, qualitatively consistent with the result from the RGB populations. However, the number ratio between the BHB and the EBHB populations is significantly different from that of the RGB and the SGB populations, n(BHB):n(EBHB) = 80:20 ($\pm$ 10) without the correction for the differential evolutionary effects and n(BHB):n(EBHB) = 88:12 with such correction.

With this HB number ratio, we showed that the comparison of the modified R values of the two groups is against the theoretical expectation that the *Ca-s* + EBHB population (G2 designated by Joo & Lee) is more helium enhanced than the *Ca-w* + BHB population (G1) as Joo & Lee (2013) proposed.

Our results for the HB number ratio and the modified R values may indicate that the EBHB is not the only progeny of the *Ca-s* RGB group. In this regard, the recent spectroscopic study of the HB stars in M22 by Gratton et al. (2014) is very intriguing as we have mentioned previously. They carried out the spectroscopic survey of the BHB stars in M22 and found a significant fraction ($\approx 18\%$) of the metal-rich helium-enhanced BHB stars in their sample (Group 3 designated by Gratton et al.). If we consider the Group 3 BHB stars by Gratton et al. (2014) as the progeny of the *Ca-s* RGB stars, the apparent HB number ratio equivalent to the *Ca-w* and the *Ca-s* RGB groups becomes 66:34 and this number ratio between the two different HB groups is in good agreement with those from the RGB and the SGB stars.[9] However, this does not explain why some of the metal-rich helium-enhanced RGB stars end up with the BHB stars, while others end up with the EBHB stars. Perhaps, may the discrepancy in the number counts indicate that there exists a non-canonical channel of the evolution of the EBHB stars without invoking the helium enhancement as proposed by Moehler et al. (2011)? Or, may this indicate that there exist the substantial spread or the bimodal distribution in helium abundance of the second generation of stars? Or, perhaps may the dispersion in the mass loss during the RGB phase be much larger than that of the canonical channel? These are the questions should be answered in the future.

We measured the mean radial velocities and velocity dispersions of of each RGB population using the results from a wide-field spectroscopic survey by Lane et al. (2009). We obtained $v_r = -144.59 \pm 0.40$ km s^{-1} and $\sigma_v = 4.71 \pm 0.35$ km s^{-1} for the *Ca-w* RGB population and $v_r = -145.77 \pm 0.89$ km s^{-1} and $\sigma_v = 7.55 \pm 0.66$ km s^{-1} for the *Ca-s* RGB population. The mean velocities of both populations are in good agreement, while the velocity dispersion of the *Ca-s* population is slightly larger.

Finally, we derived the projected rotation velocities for each population using three different methods. Our rotation velocity measurement for all RGB stars is in good agreement with previous measurements by others, ranging from 1.4 km s^{-1} to 2.1 km s^{-1} depending on the methods, suggesting that the elongated structure of M22 is most likely due to the presence of internal rotation. However, detailed comparisons between the *Ca-w* and the *Ca-s* groups revealed that they have different kinematic properties. The *Ca-s* RGB population

[9]Recall that the *Ca-s* group in M22 may be equivalent to NGC 6752, which contains both the BHB and the EBHB stars.

(2.5 – 4.3 km s^{-1}) appears to rotate faster than the *Ca-w* population (1.0 – 1.5 km s^{-1}), with different position angles of the axis of the rotation, 89° for the *Ca-w* group and 64° for the *Ca-s* group.

6. DISCUSSIONS

The up-to-date observational evidences strongly suggest that the formation history of M22 must have been different from that of normal GCs in our Galaxy. Two different formation scenarios have been frequently explored in order to elucidate the nature of M22: the self-enrichment and the merger scenarios (e.g. Lee et al. 2009a; Marino et al. 2011, 2012; Joo & Lee 2013; Lim et al. 2015). Each hypothesis has pros and cons to explain the detailed photometric and spectroscopic characteristics observed in M22.

In an attempt to delineate the chemical evolution between the two groups, at least three or four sources for specific elemental abundance changes should be involved: (i) Core-collapsed SNe: Heavy metals including Ca and Fe, but not affect the *r*-process elements. (ii) Intermediate-mass AGBs (IMAGBs) or FRMSs: Na-O, C-N anti-correlations. The He and overall C and N abundance enhancements. (iii) Low-mass AGBs (LMAGB): *s*-process elements. As extensively discussed by Marino et al. (2011, 2012) and Roederer et al. (2011), the self-enrichment formation hypothesis may require unlikely complex fine-tuning assumptions. The formation scenario of M22 in the context of the self-enrichment hypothesis can be described in the following steps[10] (e.g Marino et al. 2011); (1) The formation of the first generation (FG) of stars of the *s*-process-poor (or *Ca-w*) group (FGSP); (2) SNe II explosions, which expelled material far from the center; (3) IMAGBs of the FGSP polluted the intra-cluster medium, which went into the central region via cooling flow; (4) The formation of the second generation (SG) of stars of the *s*-poor group (SGSP); (5) LMAGBs of the FG expelled the ejecta with enhanced *s*-process elements; (6) A second cooling flow, containing the ejecta from the LMAGBs and SNeII, into the central part of the cluster; (7) The formation of the FG of the *s*-process-rich (or *Ca-s*) group (FGSR); (8) IMAGBs of the FGSR polluted the intra-cluster medium, which went into the central region via cooling flow again; (9) The formation of the SG of the *s*-rich group (SGSR); (10) Loss of stars only in the FGSP and the FGSR due to gas expulsion induced by SNe explosions.

The first problem with such self-enrichment hypothesis is the number ratios between the FG and the SG in both the *s*-poor and *s*-rich groups. The most conspicuous feature

[10]The self-enrichment hypothesis by Joo & Lee (2013) is slightly different from that of Marino et al. (2011), but it does not affect our discussions made in this paper.

can be seen in the recent spectroscopic study of the majority of normal GCs is that the SG is the major component of normal GCs, generally ≈ 50-80 % (e.g. D'Antona et al. 2008; Carretta et al. 2009). This cannot be easily explained with the chemical evolution with variant IMFs, which led D'ercole et al. (2008) to propose the loss of the vast amount of the FG stars due to the gas expulsion induced by SNe Ia explosions in the early phase of the GC evolution. This must be the case for both groups of stars in M22. We estimate that the fractions of the SG for both groups in M22 are very similar, about 40-50%, based on the [O/Fe] versus [Na/Fe] diagram of Marino et al. (2011), using the definition for the primordial component by Carretta et al. (2009). This means that the FGs in both groups are loosely bounded to the same extent with respect to each SG, so that the similar fractions of the FG stars in both groups must have been lost during the phase (10) above, which appears to be difficult to explain.[11]

The second problem is the number ratio between the two groups. Given the current theoretical framework of the normal GC formation which requires extensive mass loss of the previous generations of stars, it may be expected that the fraction of the *s*-rich (or the *Ca-s*) stars is supposed to be larger than that of the *s*-poor (*Ca-s*) stars, in sharp contrast to the result presented here, $n(Ca\text{-}w)$:$n(Ca\text{-}s) \approx 70$:30. Initially, if M22 were much more massive and located in an isolated place, such as NGC 2419, it could be able to retain the *s*-poor (or *Ca-w*) stars expelled during the phase (10) above (e.g. Caloi & D'Antona 2011). In fact, the recent observations showed that the metal-poor population is the major component of NGC 2419 (Beccari et al. 2013; Lee et al. 2013). If so, isn't it natural to expect that the FGSP and the FGSR are the major components for both groups?

The third problem is the almost flat number ratio against the radial distance, with a hint of the slightly more centrally concentrated structure of the *Ca-w* group in M22. One of the general characteristics of normal GCs is the central concentration of the SG population (e.g. Lardo et al. 2011), including NGC 2419 (Beccari et al. 2013). As mentioned earlier, the *N*-body numerical simulations by Vesperini et al. (2013) suggested that the time required to have a flat number ratio between the FG and the SG of normal GCs is likely much larger than a Hubble time. If their result is applicable to the two groups of stars in M22, the flat number ratio against the radial distance is not likely due to the dynamical evolution of the cluster with multiple stellar populations but it must have been set initially (e.g. Larsen et al. 2015).

The last problem is the difference in the velocity dispersions. As discussed by Bekki

[11]The loss of the FGSP can occur during the phases (4-5), but this cannot explain the similar fractions of the FG in both groups and the number ratio between the two groups.

(2010), the SG formed gaseous ejecta of the FG in the central region of the cluster can have larger rotational amplitudes but smaller velocity dispersions than the FG. He suggested that the dynamically cold nature of the SG is largely due to gaseous dissipation during the gas accretion onto the cluster center. Thus the lower velocity dispersion of the SG is the key signature that can be imprinted. If the *Ca-s* group were formed out of gaseous material accreted onto the center within the self-enrichment scenario, the lower velocity dispersion is expected. However this is not consistent with our result, showing that the velocity dispersion of the *Ca-s* group is slightly larger than that of the *Ca-w* group. Therefore, the difference in the velocity dispersions between the two groups does not appear to be well understood within the current frame of the dynamical evolution of the GCs with multiple stellar populations.

It is interesting to note that the heavy elemental abundance pattern between the two groups of M22 can be reproduced by the merger of two mono-metallic normal GCs, M5 and M4 (Roederer et al. 2011). In addition, we showed that the photometric characteristics of M22 can also be successfully reproduced by the two mono-metallic normal GCs, M55 and NGC 6752. As mentioned earlier, the observed CN and CH distributions in M22 RGB stars can be simply explained with the merger scenario. The differences in the spatial distributions and the kinematic properties between the two groups in M22 can not be well understood in the context of the self-enrichment hypothesis and they appear to favor the merger scenario. Also, the rather high flattened structure and rotation of M22 can be induced by the merging of a GC pair. We proposed that the plausible explanation of the formation of M22 would be that M22 formed via a merger of two GCs, preferentially, in a dwarf galaxy environment where the GC merger events are much more probable (e.g. Thurl & Johnston 2002; Bekki & Yong 2012), and then accreted later to the Milky Way (see also Carretta et al. 2010; Marino et al. 2011).

J.-W. L. acknowledges financial support from the Center for Galaxy Evolution Research through the National Research Foundation of Korea (grant no. 2010-0027910). The author thank Dr. Kiss for providing AAOmega data, Prof. Pryor for a fortran code that calculates velocity dispersion, Dr. Joo for providing model isochrones and the anonymous referee for constructive comments. Finally, special thanks should go to Prof. Bruce Carney, who first invented the *Ca* filter decades ago and provided invaluable guidance to this work.

REFERENCES

Anthony-Twarog, B. J., Twarog, B. A., Craig, J. 1995, PASP, 107, 32

Anthony-Twarog, B. J., Laird, J. N., Payne, D., & Twarog, B. A. 1991, AJ, 101, 1902

Anthony-Twarog, B. J., & Twarog, B. A. 1998, AJ, 116, 1922

Baumgardt, H., Kroupa, P., & Parmentier, G. 2008, MNRAS, 384, 1231

Bedin, L. R., Piotto, G., Anderson, J., Cassisi, S., King, I. R., Momany, Y., & Carraro, G. 2004, ApJ, 605, L125

Beccari, G., Bellazzini, M., Lardo, C., Bragaglia, A., Carretta, E., Dalessandro, E., Mucciarelli, A., & Pancino, E. 2013, MNRAS, 421, 1995

Bekki, K. 2010, ApJ, 723, L99

Bekki, K. 2012, MNRAS, 421, L44

Bekki, K., & Freeman, K. C. 2003, MNRAS, 346, L11

Bekki, K. & Yong, D. 2012, MNRAS, 419, 2063

Bjork, S. R., & Chaboyer, B. 2006, ApJ, 64, 1102

Bellini, A., Piotto, G., Bedin, L. R., King, I. R., Anderson, J., Miline, A. P., & Momany, Y. 2009 A&A, 507, 1393

Bender, R., Paquet, A., & Nieto, J.-L. 1991, A&A, 246, 349

Bertin, E., & Arnouts, S. 1996, A&AS, 317, 393

Bressan, A., Marigo, P., Girardi, L., Salasnich, B., Dal Cero, C., Rubele, S., & Nanni, A. 2012, MNRAS, 427, 127

Brown, J. W., & Wallerstein, G. 1992, AJ, 104, 1818

Caloi, V., & D'Antona, F. 2011, MNRAS, 417, 228

Cannon, R. D., Croke, B. F. W., Bell, R. A., Hesser, J. E., & Stathakis, R. A. 1998, MNRAS, 298, 601

Caputo, F., Martinez Roger, C., & Paez, E. 1987, A&A, 183, 228

Carretta E., Bragaglia, A., Gratton, R.G., Lucatello S., Cantanzaro G. et al. 2009, A&A, 505, 117

Carretta, E., Gratton, R. G., Lucatello, S., Bragaglia, A., Catanzaro, G., Leone, F., Momany, Y., DOrazi, V., Cassisi, S., DAntona, F., & Ortolani S. 2010, ApJ, 722, L1

Carretta, E., Lucatello, S., Gratton, R. G., Bragaglia, A., D'Orazi, V. 2011, A&A, 533, A69

Cassisi, S., & Salaris, M. 2013, Old Stellar Populations: how to study the fossil record of galaxy formation (Berlin:Wiley-VCH)

Cassisi, S., Salaris, M., Pietrinferni, A., Piotto, G., Milone, A. P., Bedin, L. R., & and Anderson, J. 2008 ApJ, 672, 115

Cohen, J.G., 1978, ApJ, 223, 487

Cottrell, P. L., & Da Costa, G. S. 1981, ApJ, 245, 79

D'Antona, F., Bellazzini, M., Caloi, V., Fusi Pecci, F., Galleti, S., Rood, R. T. 2005, ApJ, 631, 868

D'Antona, F., & Caloi, V. 2008, MNRAS, 390, 693

D'Antona, F., Caloi, V., Montalbán, J., Ventura, P., & Gratton, R. 2002, A&A, 395, 69

D'Antona, F., & Ventura, P. 2007, MNRAS, 379, 1431

Da Costa, G. S., Held, E. V., Saviane, I., & Gullieuszik, M. 2009, ApJ, 705, 1481

Decressin, T., Baumgardt, H., & Kroupa, P. 2008, A&A, 492, 101

Decressin T., Charbonnel C., & Meynet G. 2007, A&A, 475, 859

D'Ercole, A., Vesperini, E., D'Antona, F., McMillan, S. L. W., & Recchi, S. 2008, MNRAS, 391, 825

Decressin, T., Charbonnel, C., Meynet, G., 2007, A&A, 475, 859

Dodd, R. J., & MacGillivary, H. T. 1986, AJ, 92, 706

Goldsbury, R., Richer, H. B., Anderson, J., Dotter, A., Sarajedini, A., & Woodley, K. 2010, AJ, 140, 1830

Gratton, R. G., Lucatello, S., Sollima, A., Carretta, E., Bragaglia, A., Momany, Y., D'Orazi, V., Cassisi, S., & Salaris, M. 2014, A&A, 563, A13

Grundahl, F., Briley, M., Nissen, P. E., & Feltzing, S. 2002, A&A, 385, L14

Harbeck, D., Smith, G. H., Grebel, G. K. 2003, AJ, 125, 197

Harris, W. E. 1996, AJ, 112, 1487

Hesser, J. E., & Harris, G. L. H. 1979, ApJ, 234, 513

Hesser, J. E., & Hartwick, F. D. A., & McClure, R. D. 1977, ApJS, 33, 471

Hilker, M., & Richtler, T. 2000, A&A, 362, 895

Jester, S., Schneider, D. P., Richards, G. T., Green, R. F., Schmidt, M., Hall, P. B., Strauss, M. A., Vanden Berk, D. E., Stoughton, C., Gunn, J. E., Brinkmann, J., Kent, S. M., Smith, J. A., Tucker, D. L., Yanny, B. 2005, AJ, 130, 873

Joo, S.-J., & Lee, Y.-W. 2013, ApJ, 762, 36

Kayser, A., Hilker, M., Grebel, E. K., & Willemsen, P. G. 2008, A&A, 486, 437

Kraft, R. P. 1994, PASP, 106, 553

Kroupa, P. 2001, MNRAS, 322, 231

Lane R. R., Kiss, L. L., Lewis, G. F., Ibata, R. A., Siebert, A., Bedding, T. R. & Székely, P. 2009, MNRAS, 400, 917

Lane R. R., Kiss, L. L., Lewis, G. F., Ibata, R. A., Siebert, A., Bedding, T. R., Székely, P., Balog, Z. & Szabó, G. M. 2010, MNRAS, 406, 2732

Lane R. R., Kiss, L. L., Lewis, G. F., Ibata, R. A., Siebert, A., Bedding, T. R., Székely, P. & Szabó, G. M. 2011, A&A, 530, 31

Lardo, C., Bellazzini, M., Pancino, E., Carretta, E., Bragaglia, A., & Dalessandro, E. 2011, A&A, 525, A114

Larsen ,S. S., Baumgardt, H., Bastian, N., Brodie, J. P., Grundahl, F., & Strader, J. 2015, ApJ, 804, 71

Lee, J.-W. 2010, MNRAS, 405, L36

Lee, J.-W., & Carney, B. W. 1999, AJ, 117, 2868

Lee, J.-W., Kang, Y.-W., Lee, J., & Lee, Y.-W. 2009a, Nature, 462, 480

Lee, J.-W., Lee, J., Kang, Y.-W., Lee, Y.-W., Han, S.-I., Joo, S.-J., Rey, S.-C., & Yong, D. 2009b, ApJ, 695, L78

Lee, J.-W., López-Morales, M., Hong, K., Kang, Y.-W., Pohl, B.L., & Walker, A. 2014, ApJS, 210, 6

Lee, J.-W., Pogge, R. 2015, JKAS, submitted

Lee, S.-G. 1999, AJ, 118, 920

Lee, Y.-W., Gim, H. B., & Casetti-Dinescu, D. I. 2007, ApJ, 661, L49

Lee, Y.-W., Han, S.-I., Joo, S.-J., Jang, S., Na, J., Okamoto, S., Arimoto, N., Lim, D., Kim, H.-S., & Yoon, S.-J. 2013, ApJ, 778, L13

Lee, Y.-W., Joo, J.-M., Sohn, Y.-J., Rey, S.-C., Lee, H.-c., & Walker, A. R. 1999, Nature, 402, 55

Lim, D., Han, S.-I., Lee, Y.-W., Roh, D.-G., Sohn, Y.-J., Chun, S.-H., Lee, J.-W., & Johnson, C. I. 2015, ApJS, 216, 19

Marino, A. F., Milone, A. P., & Lind, K. 2013, ApJ, 768, 27

Marino, A. F., Milone, A. P., Piotto, G., Villanova, S., Bedin, L. R., Bellini, A., & Renzini, A. 2009, A&A, 505, 1099

Marino, A. F., Milone, A. P., Przybilla, N., Bergemann, M., Lind, K., Asplund, M., Cassisi, S., Catelan, M., Casagrande, L., Valcarce, A. A. R., Bedin, L. R., Cortés, C., D'Antona, F., Jerjen, H., Piotto, G., Schlesinger, K., Zoccali, M., & Angeloni, R. 2014a, MNRAS, 437, 1609

Marino, A. F., Milone, A. P., Sneden, C., Bergemann, M., Kraft, R. P., Wallerstein, G., Cassisi, S., Aparicio, A., Asplund, M., Bedin, R. L., Hilker, M., Lind, K., Momany, Y., Piotto, G., Roederer, I. U., Stetson, P. B., & Zoccali, M. 2012, A&A, 541, 15

Marino, A. F., Milone, A. P., Yong, D., Dotter, A., Da Costa, G., Asplund, D., Jerjen, H., Mackey, D., Norris, J., Cassisi, S., Sbordone, L., Stetson, P. B., Weiss, A., Aparicio, A., Bedin, L. R., Lind, K., Monelli, M., Piotto, G., Angeloni, R., & Buonanno, R. 2014b, MNRAS, 442, 3044

Marino, A. F., Sneden, C., Kraft, R. P., Wallerstein, G., Norris, J. E., Da Costa, G., Milone, A. P., Ivans, I. I., Gonzalez, G., Fulbright, J. P., Hilker, M., Piotto, G., Zoccali, M., & Stetson, P. B. 2011, A&A, 532, A8

McClure, R. D., & van den Bergh, S. 1968, AJ, 73, 313

Meylan, G., & Heggie, D. C. 1999, A&A Rev., 8, 1

Milone, A. P., Bedin, L. R., Piotto, G., Anderson, J., King, I. R., Sarajedini, A., Dotter, A., Chaboyer, B., Marín-Franch, A., Majewski, S., Aparicio, A., Hempel, M., Paust, N. E. Q., Reid, I. N., Rosenberg, A., & Siegel, M. 2008, ApJ, 673, 241

Milone, A. P., Marino, A. F., Dotter, A., Norris, J. E., Jerjen, H., Piotto, G., Cassisi, S., Bedin, L. R., Recio Blanco, A., Sarajedini, A., Asplund, M., Monelli, M., & Aparicio, A. 2014, ApJ, 785, 21

Milone, A. P., Stetson, P. B., Piotto, G., Bedin, L. R., Anderson, J., Cassisi, S., & Salaris, M. 2009 A&A, 503, 755

Moehler, S., Dreizler, S., Lanz, T., Bono, G., Swegart, A. V., Calamida, A., & Nonino, M. 2011, A&A, 526, A136

Norris, J., Cottrell, P. L., Freeman, K. C., & Da Costa, G. S. 1981, ApJ, 244, 205

Norris, J., & Freeman, K. C. 1983, ApJ, 266, 130

Pancino, E., Rejkuba, M., Zoccali, M., & Carrera, R. 2010, A&A, 524, A44

Peterson, R. C., & Cudworth, K. M. 1994, ApJ, 420, 612

Piotto, G., Bedin, L. R., Anderson, J., King, I. R., Cassisi, S., Milone, A. P., Villanova, S., Pietrinferni, A., & Renzini, A. 2007, ApJ, 661, L53

Piotto, G. 2008, MmSAI, 79, 334

Pryor, C., & Meylan, G. 1993, in ASP Conf. Ser. 50, Structure and Dynamics of Globular Clusters, ed. Djorgovski S., & Meylan G. (San Francisco, CA: ASP), 357

Richter, P., Hilker, M., & Richtler, T. 1999, A&A, 350, 476

Roederer, I. U., Marino, A. F., & Sneden, C. 2011, ApJ, 732, 37

Silverman, B. W. 1986, Density Estimation for Statistics and Data Analysis (Chapman & Hall/CRC, New York)

Smolinski, J. P., Martell, S. L., Beers, T. C., & Lee, Y. S. AJ, 142, 126

Sollima, A., Ferraro, F. R., Bellizzini, M., Origlia, L., Straniero, O., & Pancino, E. 2007, ApJ, 654, 915

Stetson P. B. 1987, PASP, 99, 191

Stetson P. B. 1990, PASP, 102, 932

Stetson P. B. 1993, in IAU Coll. 136, Stellar Photometry: Current Techniques and Future Developments, ed. C. J. Butler & I. Elliot (Cambridge: Cambridge Univ. Press), 291

Stetson P. B. 1994, PASP, 106, 250

Stetson P. B. 1995, DAOPHOTII User's Manual (Victoria : Dominion Astrophys. Obs.)

Stetson P. B., & Harris, W. E. 1988, AJ, 96, 909

Stone, R. C. 1989, AJ, 97, 1227

Thurl, C., & Johnston, K. V. 2002, ASP Conf. Ser. Vol. 265, ω Centauri: A Unique Window into Astrophysics, ed. F. van Leeuwen, J. D. Hughes, & G. Piotto (San Francisco: ASP), 337

Trager, S. C., King, I. R., & Djorgovski, S. 1995, AJ, 109, 218

Tripicco, M. J., & Bell, R. A. 1991, AJ, 102, 744

Turner A. M. 1995, Cooking with ALLFRAME: Photometry and the H_0 Key Project (Victoria : Dominion Astrophys. Obs.)

Twarog, B. A., & Anthony-Twarog, B. J. 1995, AJ, 109, 2828

Valcarce, A. A. R., Catelan, M., & Sweigart, A. V. 2012, A&A, 547, A5

van de Ven, G., van den Bosch, R. C. E., Verolme, E. K., & de Zeeuw, P. T. 2006, A&A, 445 513

Ventura, P., D'Antona, F., Mazzitelli, I., & Gratton, R. 2001, ApJ, 550, L65

Vesperini, E., McMillan, S. L. W., D'Antona, F., & D'Ercole, A. 2013, MNRAS, 429, 1913

Yong, D., Grundahl, F., Johnson, J. A., & Asplund, M. 2008, ApJ, 684, 1159

Zacharias, N., Monet, D. G., Levine, S. E., et al. 2004, AAS, 205, 4815

Table 1. Journal of observations.

date (yy/mm/dd)	Int. Exp. Time (s) y	b	Ca	Tel. (CTIO)	Weather
11/03/27	180	310	1,500	1.0m	Photometric
11/03/28	340	580	2,400	1.0m	Non-photometric
11/03/29	340	580	2,400	1.0m	Photometric
11/03/30	340	580	1,800	1.0m	Non-photometric
11/03/31	160	540	2,400	1.0m	Photometric
11/04/01	600	1,350	4,200	1.0m	Non-photometric
11/04/02	275	600	2,100	1.0m	Photometric
11/04/03	400	900	3,000	1.0m	Photometric
11/04/07	200	450	1,500	1.0m	Photometric
11/08/19	100	200	1,200	1.0m	Photometric
11/08/20	200	400	1,500	1.0m	Non-photometric
11/08/21	350	600	2,400	1.0m	Photometric
11/08/22	300	500	2,400	1.0m	Photometric
11/08/31	310	240	900	1.0m	Non-photometric
11/09/04	100	200	900	1.0m	Photometric
12/04/29	60	180	1,200	0.9m	Non-photometric
12/07/12	250	330	1,200	0.9m	Non-photometric
12/07/14	200	600	1,200	0.9m	Non-photometric
12/07/16	100	300	1,500	0.9m	Non-photometric
12/07/18	200	500	1,500	0.9m	Non-photometric
12/07/19	100	250	1,500	0.9m	Non-photometric
12/07/21	200	500	1,500	0.9m	Non-photometric
12/07/22	60	180	2,400	0.9m	Non-photometric
12/07/23	50	150	1,200	0.9m	Photometric
12/07/24	130	390	1,200	0.9m	Photometric
12/10/10	140	420	3,000	1.0m	Photometric
12/10/11	120	360	2,400	1.0m	Photometric
13/04/07	80	200	1,200	1.0m	Photometric
13/04/08	185	475	1,500	1.0m	Non-photometric
13/04/11	180	500	1,500	1.0m	Photometric

Table 1—Continued

date (yy/mm/dd)	Int. Exp. Time (s) y	b	Ca	Tel. (CTIO)	Weather
13/04/12	115	310	1,500	1.0m	Photometric
13/04/13	100	250	1,200	1.0m	Photometric
13/05/14	100	250	1,500	1.0m	Non-photometric
13/07/27	80	200	1,200	1.0m	Non-photometric
13/07/28	180	260	1,200	1.0m	Non-photometric
13/07/31	95	240	1,200	1.0m	Non-photometric
13/08/02	180	500	1,500	1.0m	Non-photometric
14/05/23	150	450	1,800	1.0m	Non-photometric
14/05/25	300	900	3,900	1.0m	Non-photometric
14/05/26	300	900	3,900	1.0m	Photometric
14/05/27	240	600	3,600	1.0m	Photometric
14/05/30	320	800	3,600	1.0m	Photometric
14/05/31	615	1,545	8,700	1.0m	Photometric
14/06/01	120	360	1,500	1.0m	Photometric
total	9,145	20,930	90,900		

Table 2. Comparisons of photometric results.

	Anthony-Twarog et al.	Richter et al.
No. of stars	198	60
ΔV	$+0.024 \pm 0.051$	-0.038 ± 0.027
$\Delta(b-y)$	$+0.034 \pm 0.050$	$+0.003 \pm 0.037$
$\Delta m1$	-0.028 ± 0.063	$+0.021 \pm 0.037$
Δhk	-0.029 ± 0.079	$\cdots$

Table 3. Color-Magnitude Diagram data.

ID	RA	Dec	V	$b-y$	hk
96	279.502014	-24.007305	11.436	0.849	1.280
104	279.061249	-24.014750	11.895	0.717	0.901
106	279.059052	-24.033777	11.756	0.927	0.954
130	278.959198	-24.261583	11.649	0.895	1.178
146	279.027954	-24.347834	12.278	0.528	0.463
163	279.502747	-24.352249	11.570	0.836	1.186
197	279.064087	-23.805361	12.211	0.885	0.815
252	279.312927	-23.539223	11.941	0.308	0.409
285	279.184082	-23.980139	12.530	0.888	0.842
297	279.138306	-23.940722	12.655	0.942	0.830
301	278.767181	-24.275888	13.256	0.202	0.221

Note. — Table 3 is presented in its entirety in the electronic edition of the Astrophysical Journal Supplement. A portion is shown here for guidance regarding its form and content.

Table 4. Number ratios.

	Before Correction	After Correction	Error
$n(Ca\text{-}w)$:$n(Ca\text{-}s)$	69:31	70:30	$\pm$ 3
n(bSGB):n(fSGB)	69:31	62:38	$\pm$ 6
n(BHB):n(EBHB)	80:20	88:12	$\pm$ 10

Table 5. Centers of M22.

	Simple mean		Half-sphere		Pie-slice	
	ΔX($''$)	ΔY($''$)	ΔX($''$)	ΔY($''$)	ΔX($''$)	ΔY($''$)
All	2.9	−0.1	5.5	1.1	7.1	1.0
Ca-w	3.8	0.4	7.5	1.6	7.7	−2.8
Ca-s	0.8	5.6	−1.4	−1.4	−4.9	6.5

Table 6. Ellipse fitting parameters.

Pop.	grid	Ellipse center		θ	b/a	e
		ΔX($''$)	ΔY($''$)			
Ca-w	0.9	10.5 ± 0.4	4.2 ± 0.4	1.6 ± 1.4	0.929 ± 0.016	0.071
	0.8	10.1 ± 0.6	4.6 ± 0.6	3.2 ± 1.3	0.931 ± 0.015	0.069
	0.7	9.2 ± 0.7	5.2 ± 0.7	4.9 ± 1.2	0.937 ± 0.014	0.063
	0.6	7.9 ± 0.7	5.0 ± 0.8	7.3 ± 1.1	0.940 ± 0.013	0.060
	0.5	6.2 ± 0.8	4.3 ± 0.8	11.2 ± 1.0	0.943 ± 0.011	0.057
	0.4	3.5 ± 0.8	2.7 ± 0.8	17.4 ± 0.8	0.942 ± 0.010	0.058
	0.3	0.2 ± 0.7	-0.6 ± 0.8	24.3 ± 0.7	0.934 ± 0.008	0.066
	0.2	-2.3 ± 0.7	-5.2 ± 0.7	31.4 ± 0.5	0.912 ± 0.006	0.088
Ca-s	0.9	-6.6 ± 0.4	6.2 ± 0.4	15.3 ± 1.3	0.943 ± 0.015	0.057
	0.8	-3.3 ± 0.6	5.4 ± 0.6	18.9 ± 1.2	0.943 ± 0.014	0.057
	0.7	0.1 ± 0.7	3.6 ± 0.7	24.1 ± 1.1	0.944 ± 0.013	0.056
	0.6	3.8 ± 0.8	0.8 ± 0.7	29.2 ± 1.0	0.941 ± 0.011	0.059
	0.5	6.8 ± 0.8	-3.2 ± 0.8	35.4 ± 0.8	0.934 ± 0.010	0.066
	0.4	8.1 ± 0.8	-8.0 ± 0.8	42.7 ± 0.7	0.912 ± 0.008	0.088
	0.3	6.6 ± 0.7	-13.2 ± 0.8	41.8 ± 0.6	0.872 ± 0.006	0.128
	0.2	2.4 ± 0.7	-13.5 ± 0.7	37.6 ± 0.4	0.837 ± 0.005	0.163

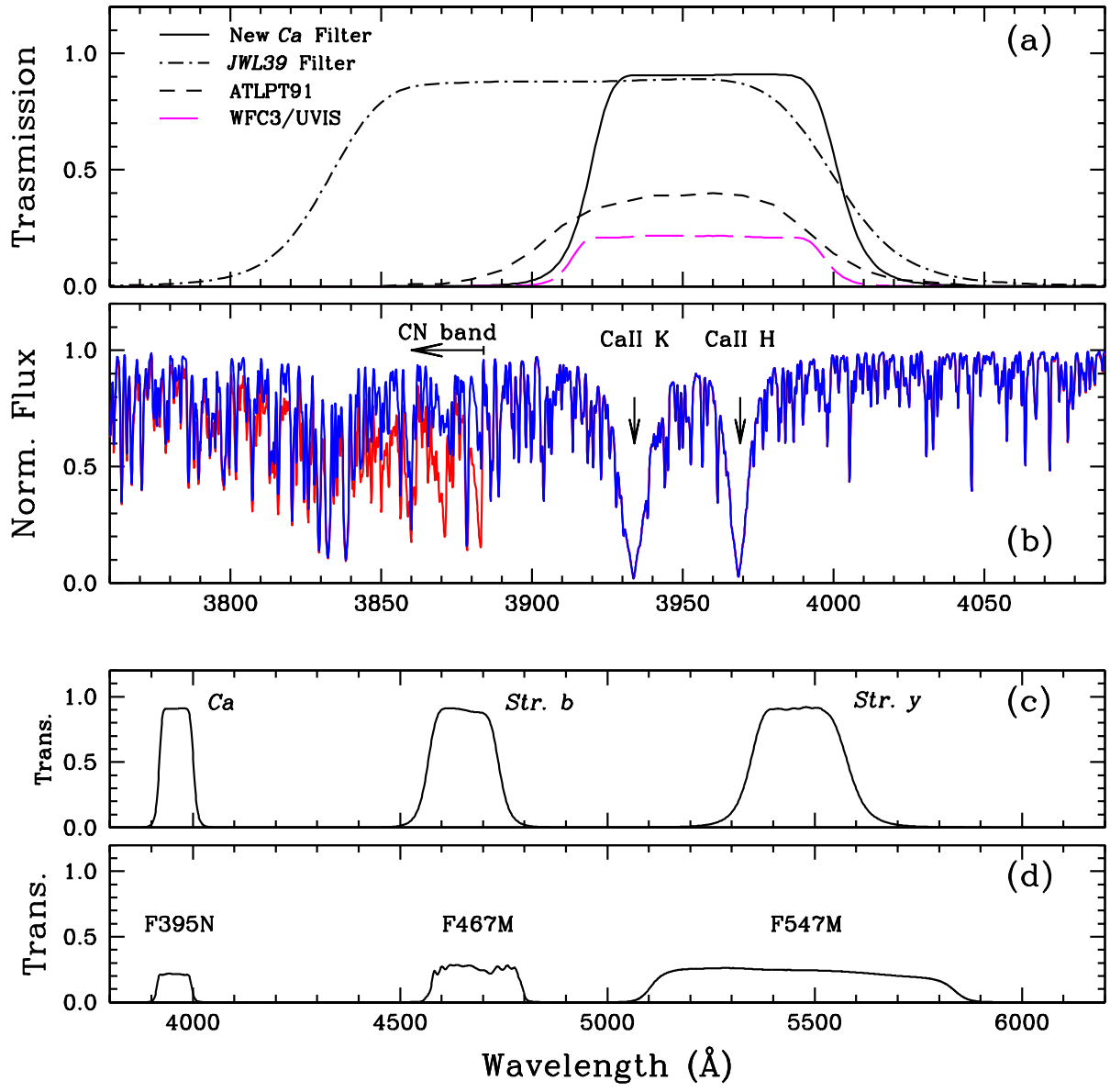

Fig. 1.— (a) A comparison of Ca filter transmission functions between that in Anthony-Twarog et al. (1991) (the dotted line) and that for our new Ca filter measured with collimated beam (the solid line). Both filters have similar FWHMs, approximately 90 Å but our new Ca filter has a more uniform and high transmission across the passband, dropping more rapidly at both edges. The transmission function for the new filter system, $JWL39$, is also shown in the plot. (b) Synthetic spectra for the CN normal (the blue line) and the CN strong (the red line) RGB stars. The CN band at λ 3885 Å lies outside of the lower boundary of our new Ca filter. On the other hand, we can measure the CN band strength by using our new filter system, $JWL39$. (c) Filter transmission functions for the ground-based extended Strömgren photometry. (d) Filter transmission functions for the HST WFC3/UIVS photometry. Note that the bandwidth of the HST F547M is about twice as broad as that of the Strömgren y filter.

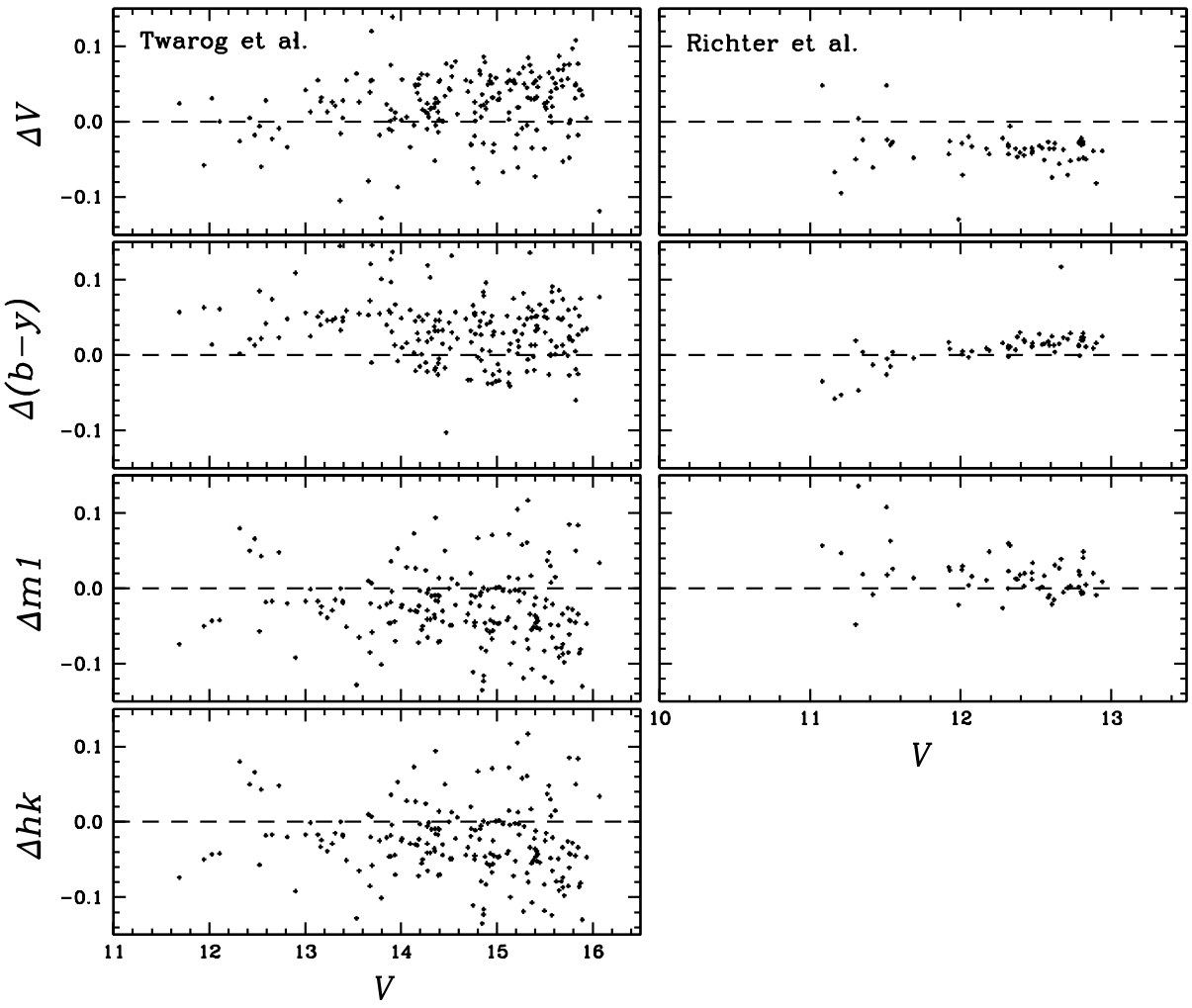

Fig. 2.— Residuals of the CCD photometry of Anthony-Twarog et al. (1995) and Richter et al. (1999) as a function of the magnitude. The differences are in the sense of Anthony-Twarog et al. or Richter et al. minus our work.

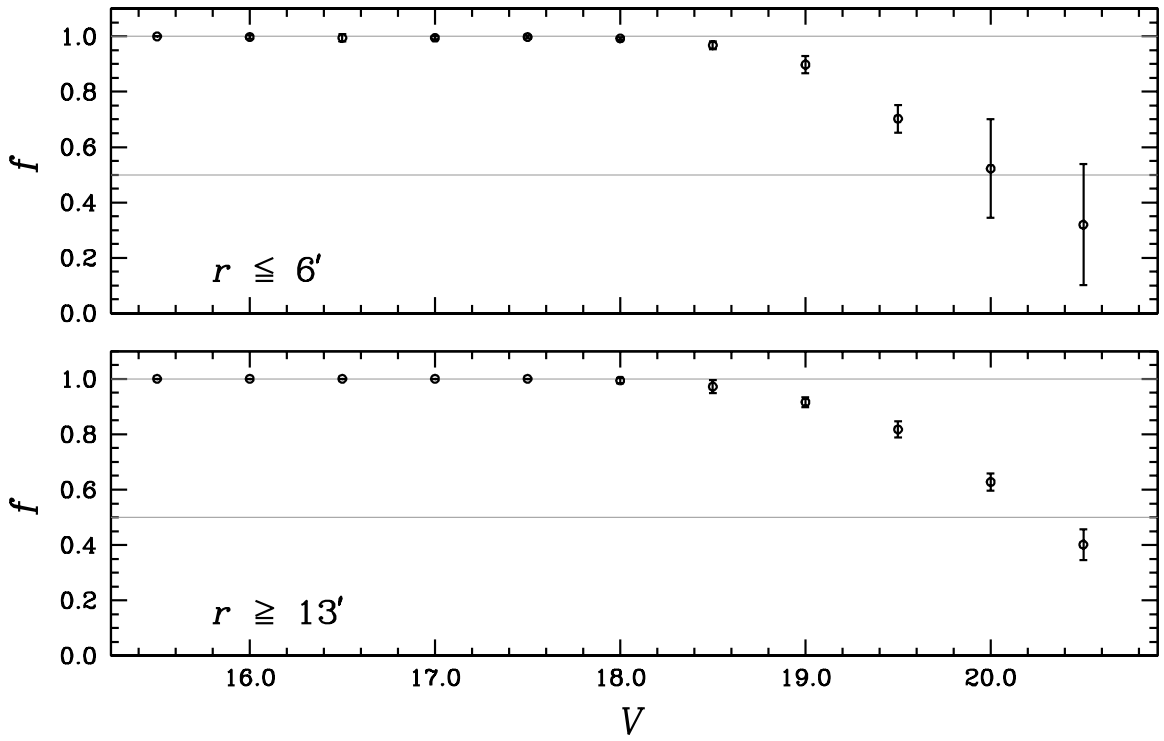

Fig. 3.— Completeness fractions at each magnitude bin measured from artificial star experiments for the inner and outer parts of M22. The experiments suggest that our photometry is complete down to $V \approx 18.5$ mag.

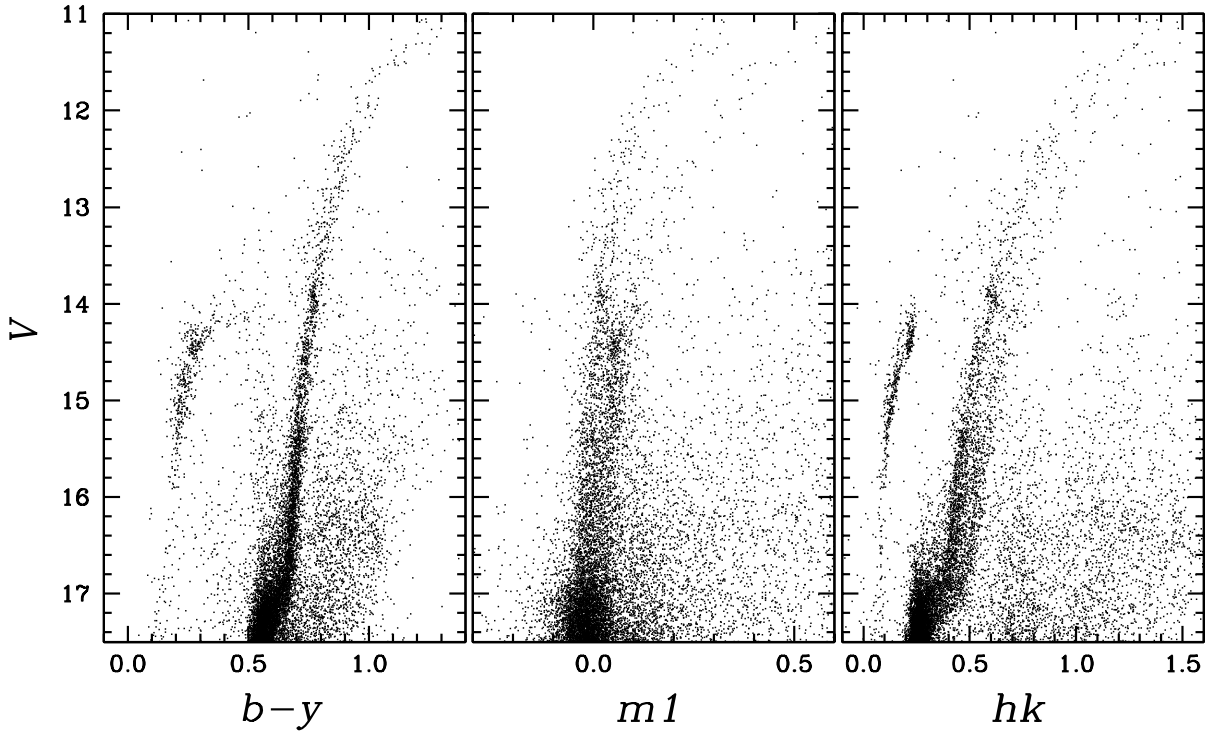

Fig. 4.— Color-magnitude diagrams for bright stars located within 10 arcmin from the center of the cluster. Note that discrete two RGB sequences can be clearly seen in the hk versus V CMD. In the figure, the $m1$ versus V CMD is taken from Lee et al. (2009a).

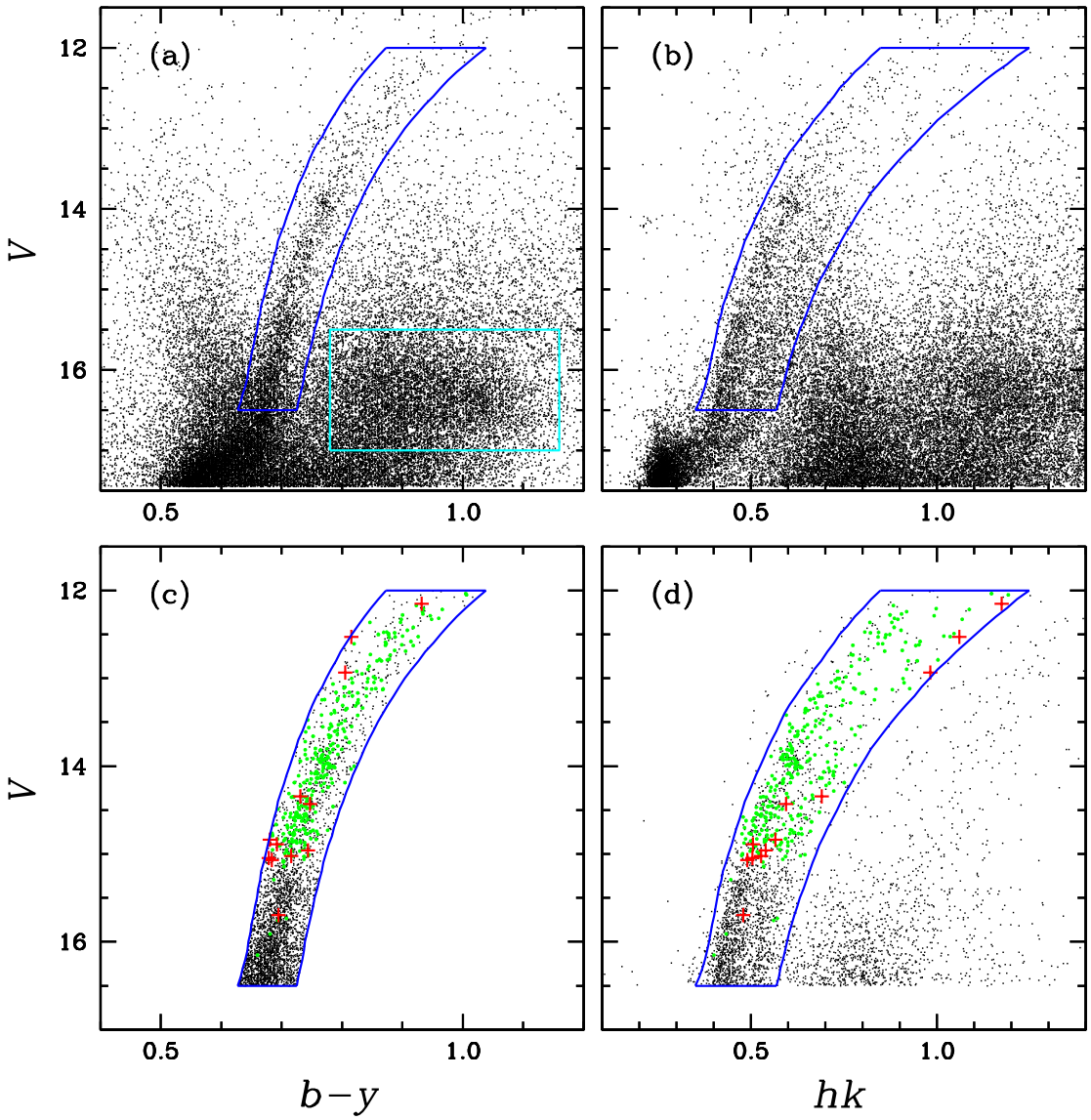

Fig. 5.— (a) & (b) CMDs of the M22 field. The enclosed regions by blue lines indicate the location of RGB stars in M22, while the enclosed region by cyan box in (a) mostly represents the bulge red-clump star population; (c) The number of stars in the enclosed region is 3571. Compared with Lane et al. (2009), we have 307 stars in common; 295 stars are the radial velocity member star (green dots) and 12 are radial velocity non-member star (red plus signs). (d) The hk versus V CMD for 3571 stars from (c). The number of stars in the enclosed region is 2054 without the radial-velocity non-member stars.

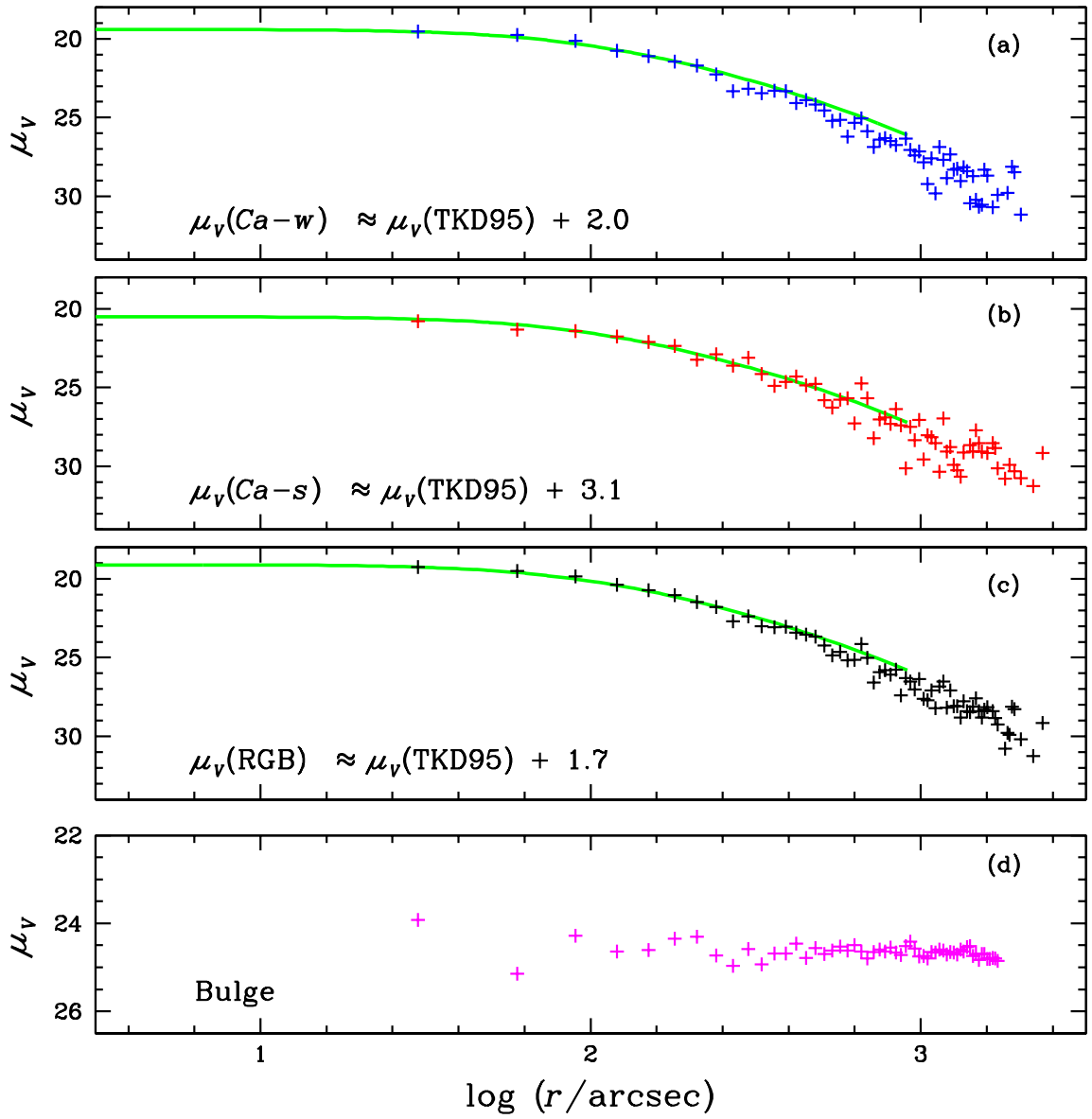

Fig. 6.— The surface-brightness profiles for M22 RGB stars with $12.0 \leq V \leq 16.5$ mag. (a) *Ca-w* RGB stars only; (b) *Ca-s* RGB stars only; and (c) All RGB stars in M22. Our surface-brightness profiles for M22 RGB stars are in excellent agreement with the Chebyshev polynomial fit of M22 by Trager et al. (1995), shown with green solid lines. On the other hand, the surface-brightness profile for the Galactic bulge red-clump stars is almost flat against the radial distance from the center of the cluster. Our results strongly suggest that the contamination from the off-cluster field star in our RGB selection procedure is not severe.

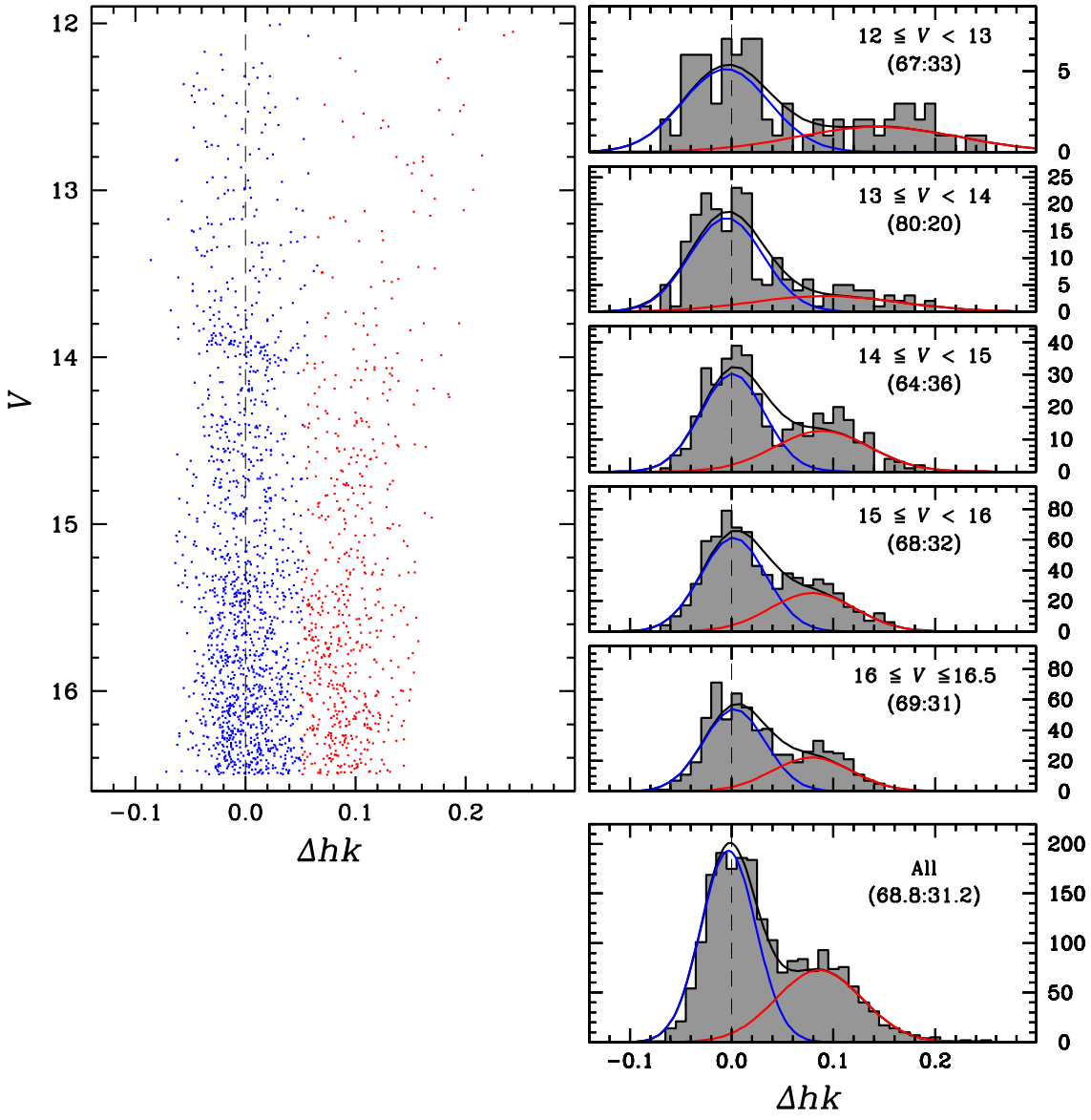

Fig. 7.— (Left) The plot of Δhk versus V for M22 RGB stars, where Δhk is defined to be the difference in color from the mean fiducial sequence of the Ca-w group. Stars with the probability of being the Ca-w group $P(w) \geq 0.5$ from the EM estimator assuming the two gaussian mixture model are denoted with blue dots, while $P(s) > 0.5$ with red dots. (Right) Histograms of M22 RGB stars with different magnitude bins. The two gaussian distribution was estimated by using the EM method and the number ratio in the parenthesis is for $n(Ca\text{-}w)$:$n(Ca\text{-}s)$ in each bin.

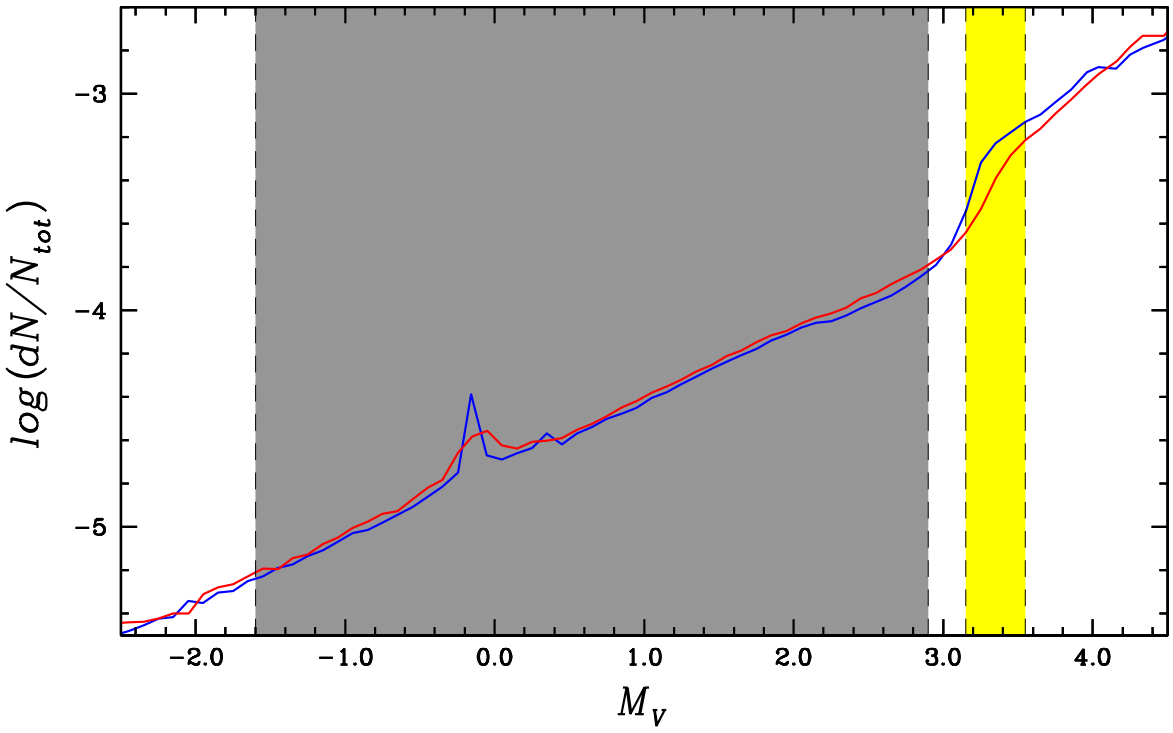

Fig. 8.— The theoretical luminosity functions for the *Ca-w* group (the blue line) and the *Ca-s* group (the red line). The grey shaded area corresponds to the RGB stars and the yellow shaded area to the SGB stars analyzed in our current work. Note that the RGB number ratio between the two groups at the fixed magnitude bin is very similar, $n(Ca\text{-}w)$:$n(Ca\text{-}s)$ = 48.3:51.7 (± 0.3), while the number of SGB stars in the *Ca-w* (or bSGB) group is slightly larger than that in the *Ca-s* (or fSGB) group, n(bSGB):n(fSGB) = 58.0:42.0 (± 0.2).

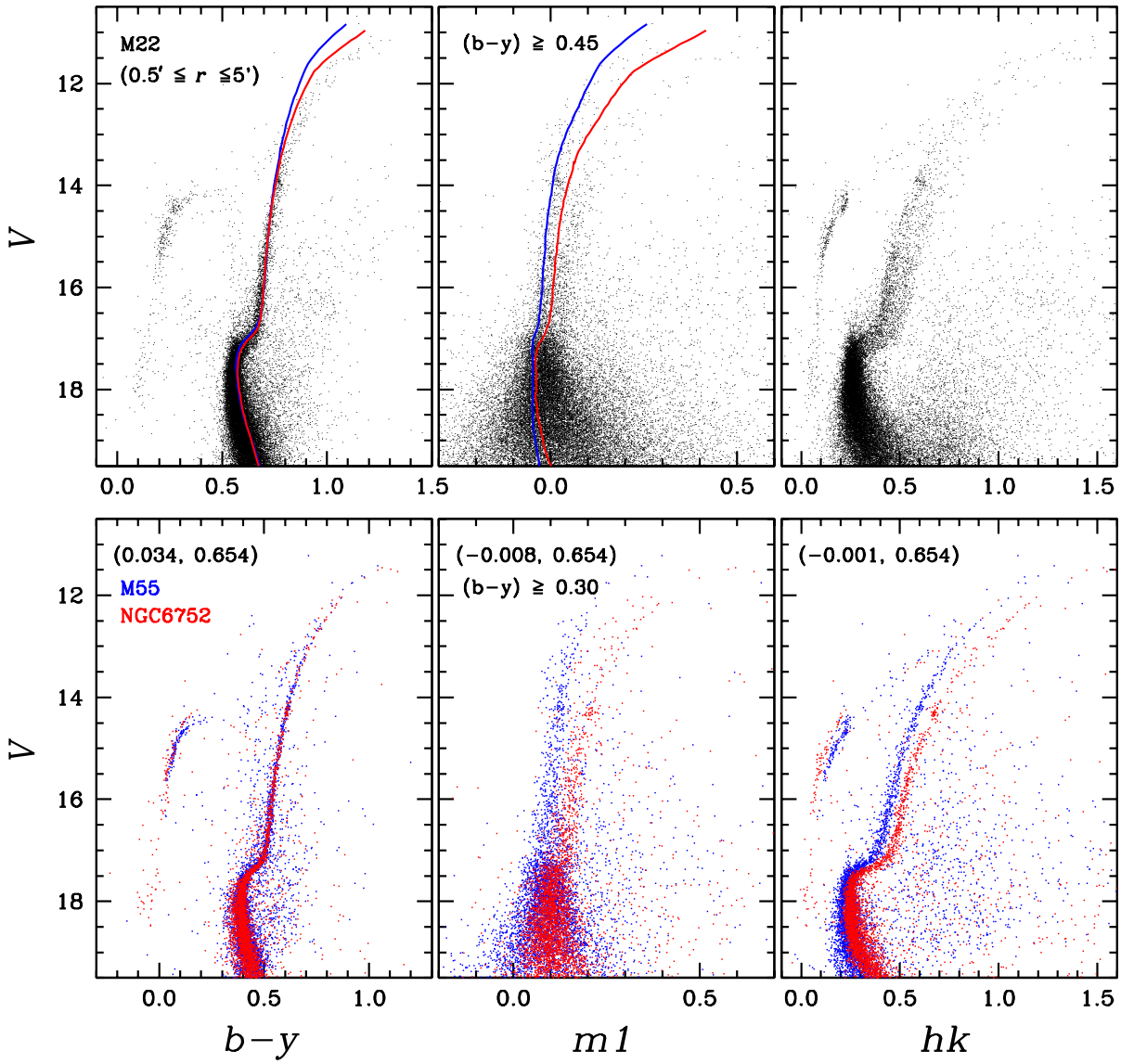

Fig. 9.— (Upper panels) CMDs of M22 using stars with $0.5 \leq r \leq 5.0$ arcmin. In the $m1$ versus V CMD, we show stars with $(b-y) \geq 0.45$ mag, since the location of HB stars in the CMD overlaps with that of RGB stars. Note that the blue solid line is for the Padova isochrone with [Fe/H] = −1.8 and the red solid line for −1.5 (Bressan et al. 2012). (Bottom panels) Composite CMDs for globular clusters M55, which mimics the *Ca-w* groups in M22, shown with blue dots and NGC 6752, which mimics the *Ca-s* groups, with red dots. The numbers in the parentheses indicate differential colors and the visual magnitude terms for NGC 6752 with respect to M55. The composite CMDs using M55 and NGC 6752 reproduce very well the photometric characteristics of M22 in the $m1$ versus V and hk versus V CMDs.

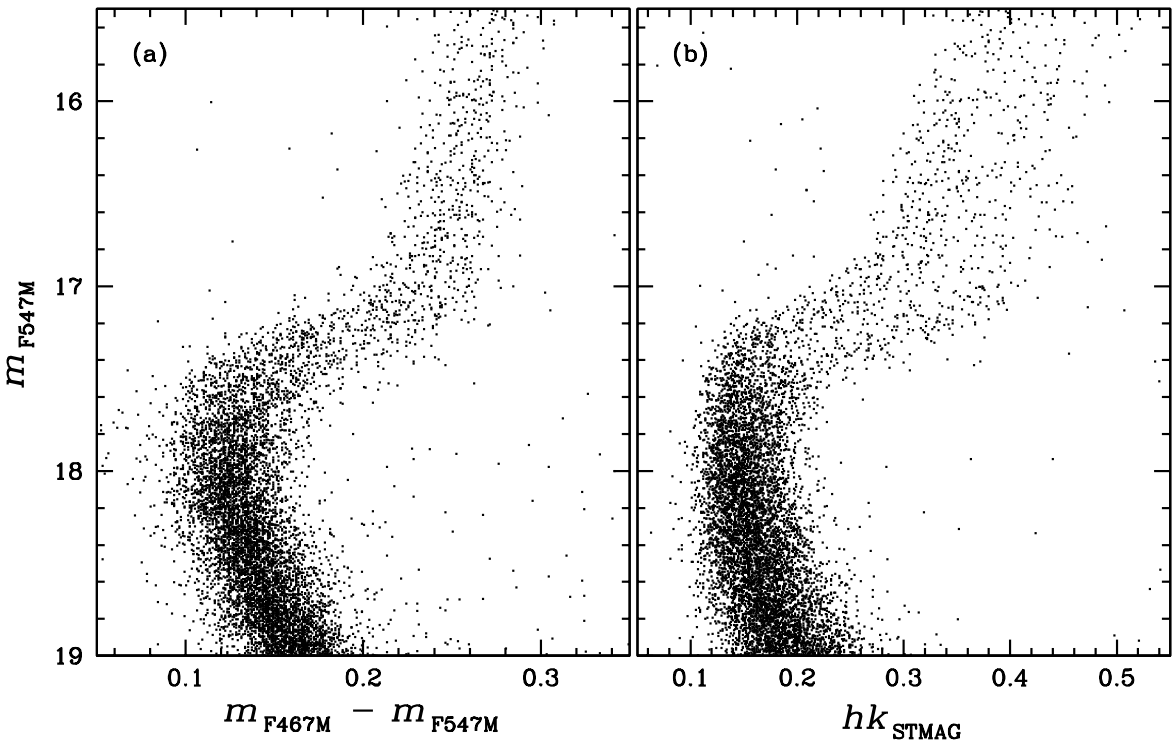

Fig. 10.— Color-magnitude diagrams of M22 using the HST data. The $hk_{\rm STMAG}$ denotes $(m_{\rm F395N} - m_{\rm F467M}) - (m_{\rm F467M} - m_{\rm F547M})$. The split in the SGB and the RGB sequences in M22 can be clearly seen in the $hk_{\rm STMAG}$ versus $m_{\rm F547M}$ CMD.

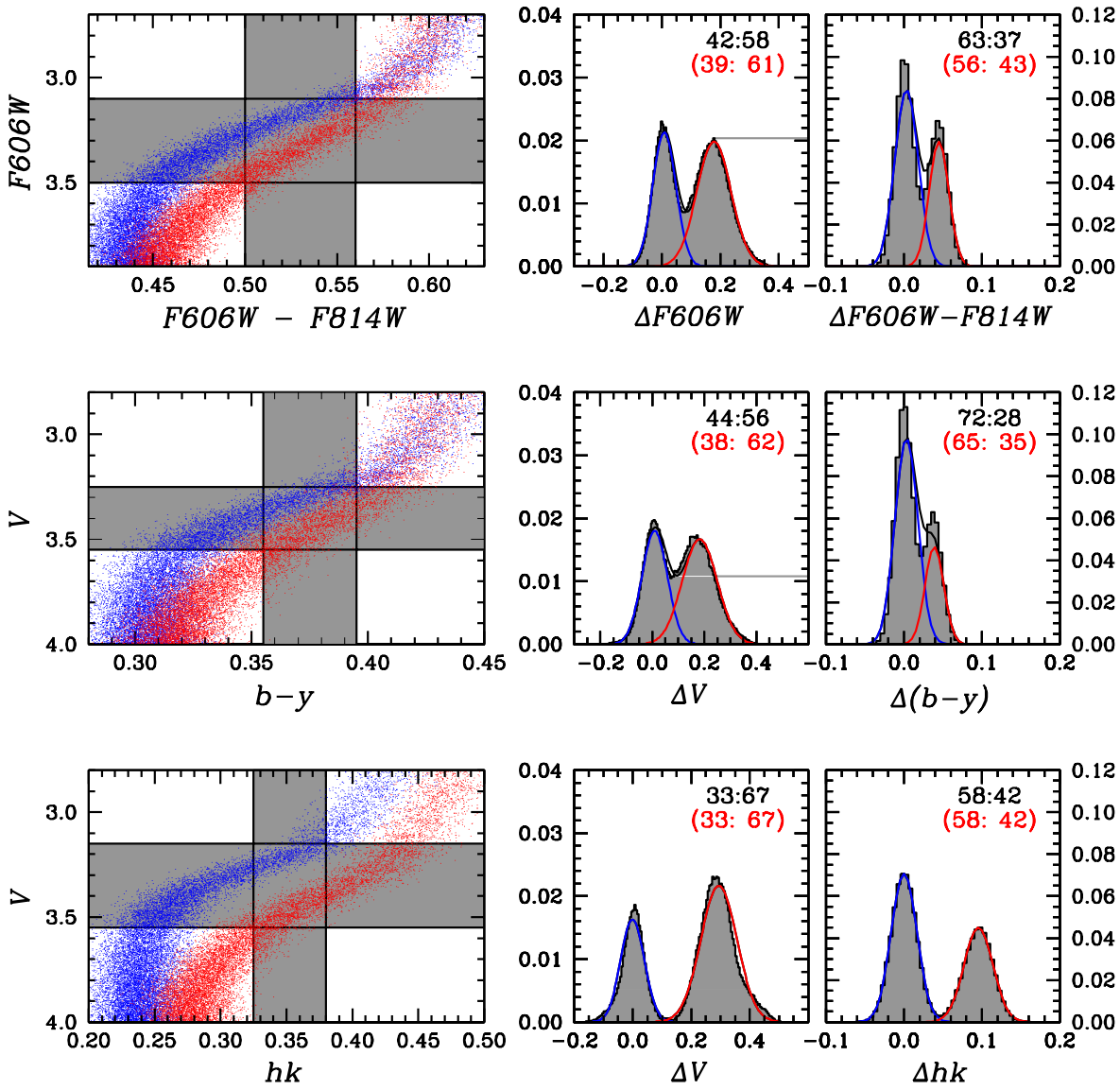

Fig. 11.— (Left panels) Artificial CMDs around the SGB region of M22 for different photometric systems. The blue dots are for the bSGB stars and the red dots are for the fSGB stars. The vertical and horizontal grey shaded regions indicate ranges in the color indexes and in the magnitudes used to derive the number ratios between the two groups. We show only a small fraction of stars in each plot for the sake of clarity. (Middle panels) The distributions of SGB stars at the fixed color indexes. The first number ratios in each plot are those returned from the EM estimator assuming the two gaussian mixture model while the number ratios in the parenthesis are the input values from our evolutionary population models. (Right panels) The distributions of SGB stars at the fixed magnitudes. Note that the number ratios from the (hk, V) plane are the most reliable, while those from the ($b-y$, V) plane are the least reliable.

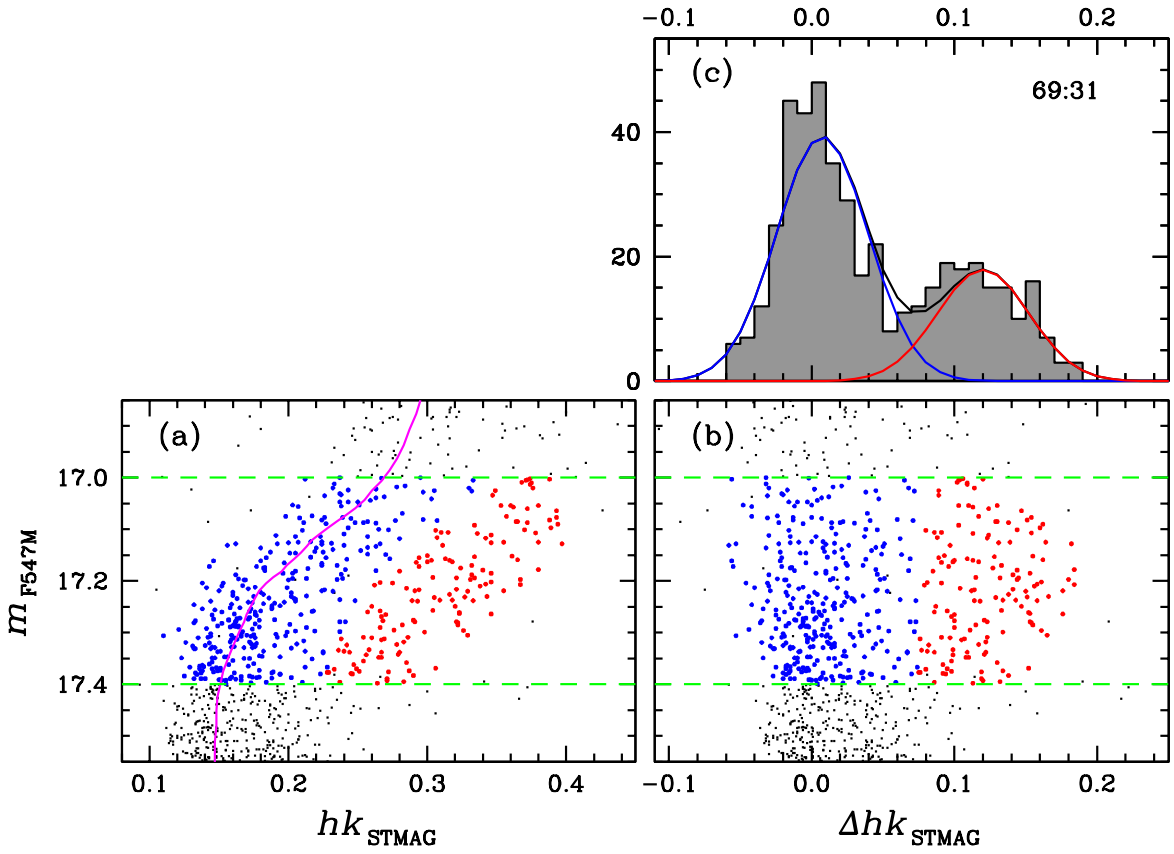

Fig. 12.— (a) The $hk_{\rm STMAG}$ versus $m_{\rm F547M}$ CMD around the SGB region of M22. Also shown is the fiducial sequence for the bSGB group. We use the SGB stars with 17.0 mag $\leq m_{\rm F547M} \leq$ 17.4 mag to estimate the number ratio between the two groups. The stars with P(bSGB) ≥ 0.5 from the EM estimator are denoted with blue dots, while P(fSGB) > 0.5 with red dots. (b) The plot of $\Delta hk_{\rm STMAG}$ versus V, where $\Delta hk_{\rm STMAG}$ is defined to be the difference in the $hk_{\rm STMAG}$ index between the individual stars and the fiducial sequence of the bSGB group. (c) The distribution of $\Delta hk_{\rm STMAG}$ and the two gaussian mixture model fit to the data. We obtain the apparent number ratio of n(bSGB):n(fSGB) = 69:31 ($\pm$ 6) and the intrinsic number ratio of n(bSGB):n(fSGB) = 62:38 ($\pm$ 6) after applying the correction for the differential evolutionary effect. This SGB number ratio is in agreement with the RGB number ratio within measurement errors.

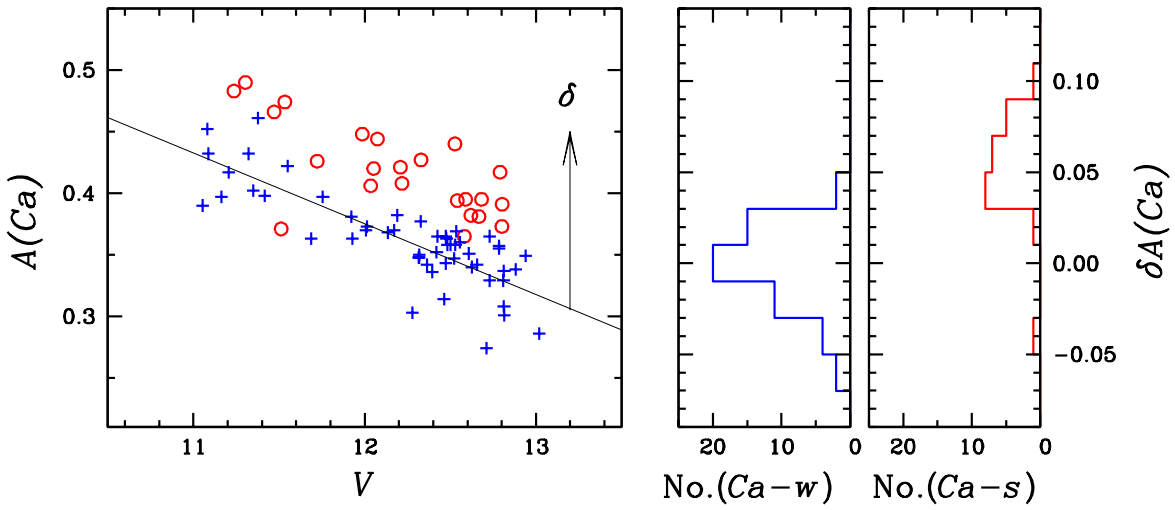

Fig. 13.— A comparison of the Calcium index A(Ca) measured by Norris & Freeman (1983) between the RGB stars in the *Ca-w* (blue plus signs) and the *Ca-s* (red circles) groups in M22 as functions of V magnitude. We also show the least square fit to the *Ca-w* RGB stars and the differences are measured from the fitted line to correct the temperature and the surface gravity effects on the absorption strengths. The histograms for each group are shown in the right panel. Note that the boundary between the two groups is rather sharp.

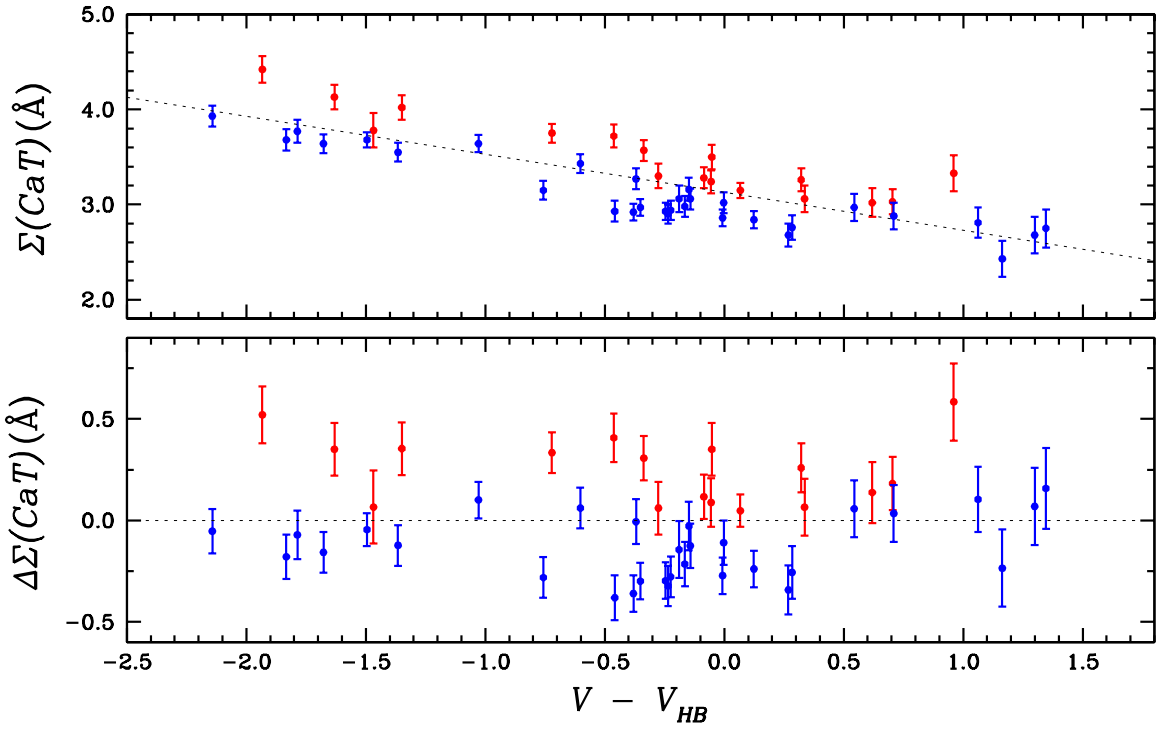

Fig. 14.— Comparisons of Ca II triplet strength Σ(CaT), (= $W_{8542} + W_{8662}$), measured by Da Costa et al. (2009) for the *Ca-w* (blue circles) and the *Ca-s* (red circles) RGB stars against magnitude difference from the horizontal branch, $V - V_{\rm HB}$. In the upper panel, the dotted line denotes the least square fit to the data. The lower panel show the residuals around the fitted line.

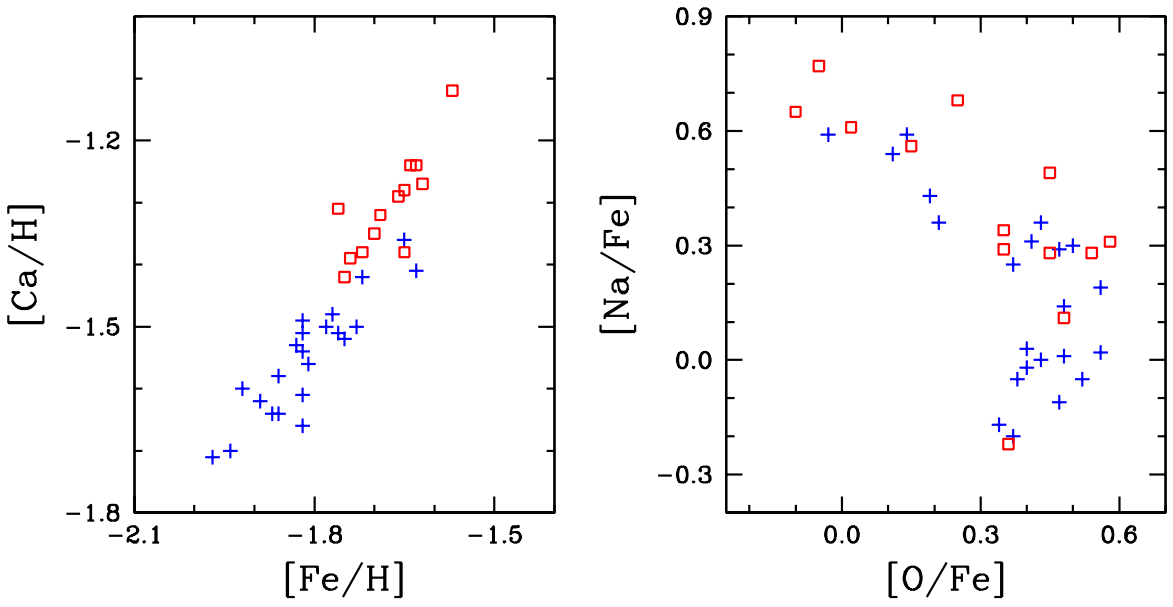

Fig. 15.— Plots of [Ca/H] versus [Fe/H] and [Na/Fe] versus [O/Fe] for the *Ca-w* (blue pluses) and the *Ca-s* (red squares) RGB stars using high-resolution spectroscopic measurements by Marino et al. (2011). The plot of [Ca/H] versus [Fe/H] shows that the RGB stars in the *Ca-w* group have lower calcium and iron abundances than those in the *Ca-s* group. The plot of [Na/Fe] versus [O/Fe] shows that each group has its own Na-O anti-correlations. In the mean the *Ca-w* group appears to have a higher oxygen and a lower sodium abundances than the *Ca-s* group.

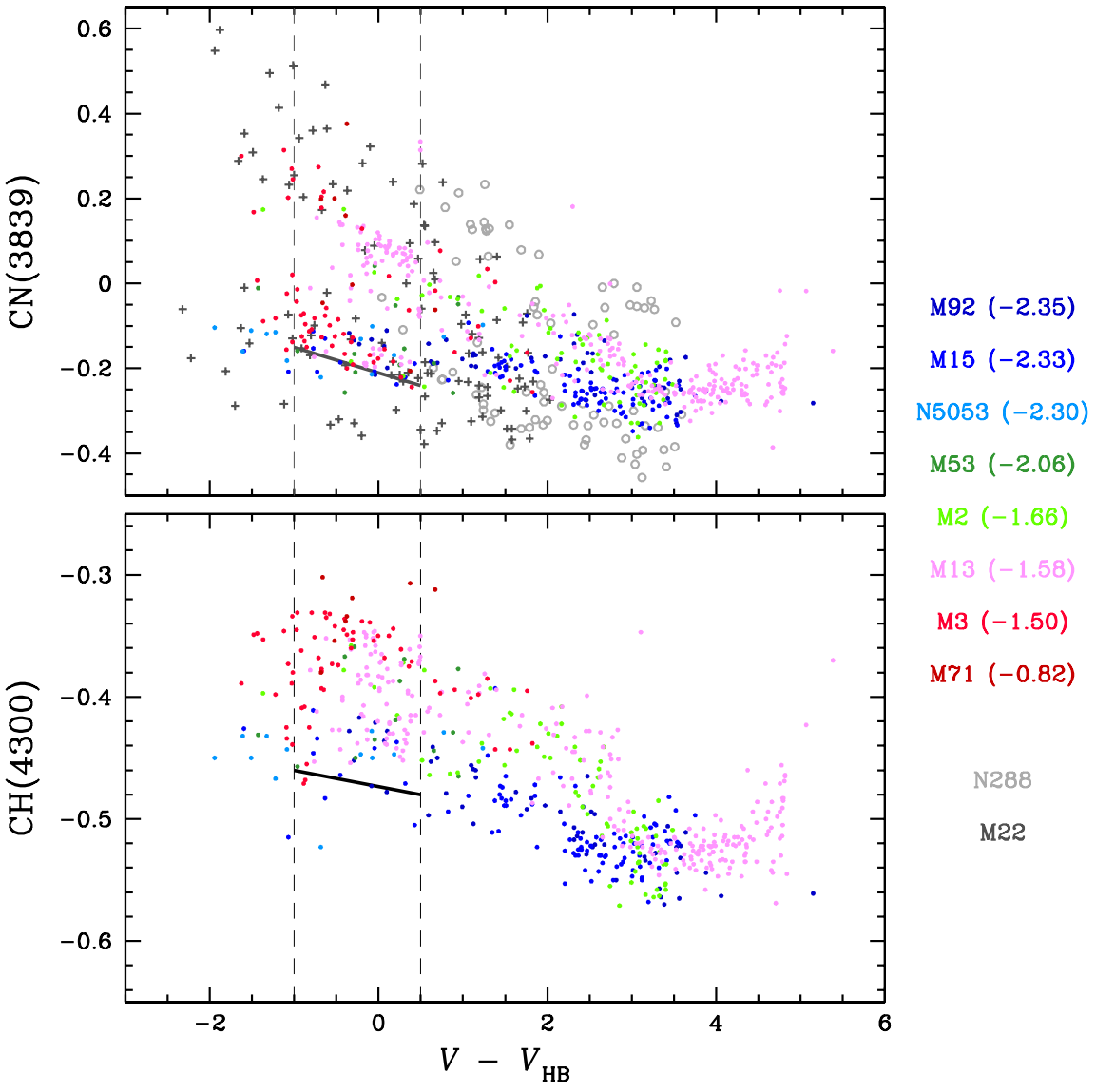

Fig. 16.— Distributions of CN(3839) and CH(4300) against $V - V_{\rm HB}$ for 8 GCs by (Smolinski et al. 2011). The numbers inside the parentheses are the metallicity of each GC. Also shown are two GCs, M22 and NGC 288, by Lim et al. (2015). The thick solid lines denote the common lower envelopes for RGB stars around $V_{\rm HB}$, $-1 \leq V - V_{\rm HB} \leq 0.5$, used in our analysis. Note that the CN(3839) and CH(4300) index values by Smolinski et al. (2011) do not agree with those by Lim et al. (2015) due to different definitions of the band strengths between the two works.

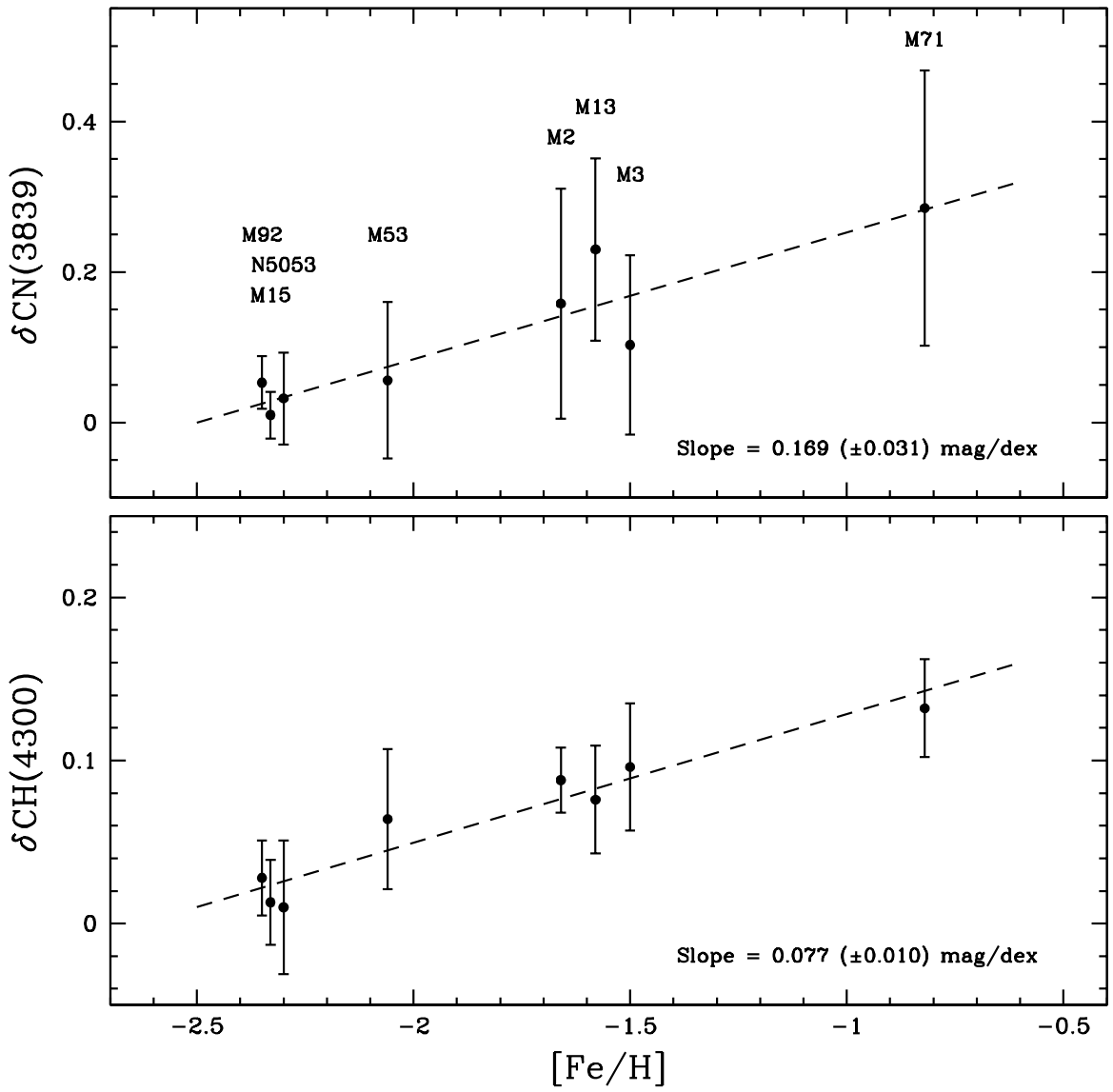

Fig. 17.— The distributions of the δCN(3839) and the δCH(4300) against [Fe/H] for 8 GCs by Smolinski et al. (2011), where the δCN(3839) and the δCH(4300) are defined to be the differences in the band strengths from the common lower envelopes. The least square fits to the data are shown with dashed lines. As expected from Figure 16, both the δCN(3839) and the δCH(4300) have the gradients against metallicity.

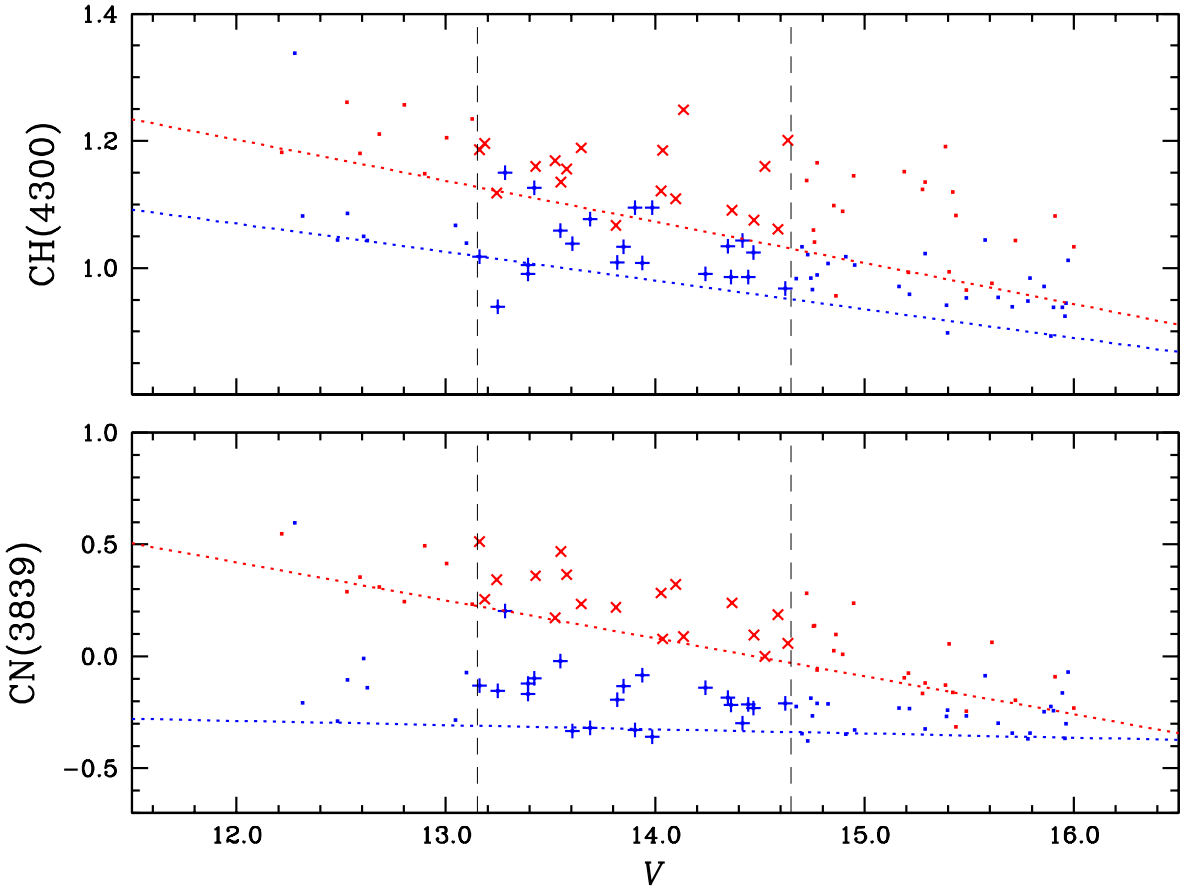

Fig. 18.— Distributions of CN(3839) and CH(4300) against $V - V_{\rm HB}$ for M22 RGB stars by Lim et al. (2015). The blue color and the red color denote the *Ca-w* and the *Ca-s* RGB stars in M22, respectively. The blue dotted lines denote the lower envelope for the *Ca-w* stars, while the red dotted lines for the *Ca-s* stars. The vertical dashed lines denote the region around the $V_{\rm HB}$ of M22, $-1 \leq V - V_{\rm HB} \leq 0.5$.

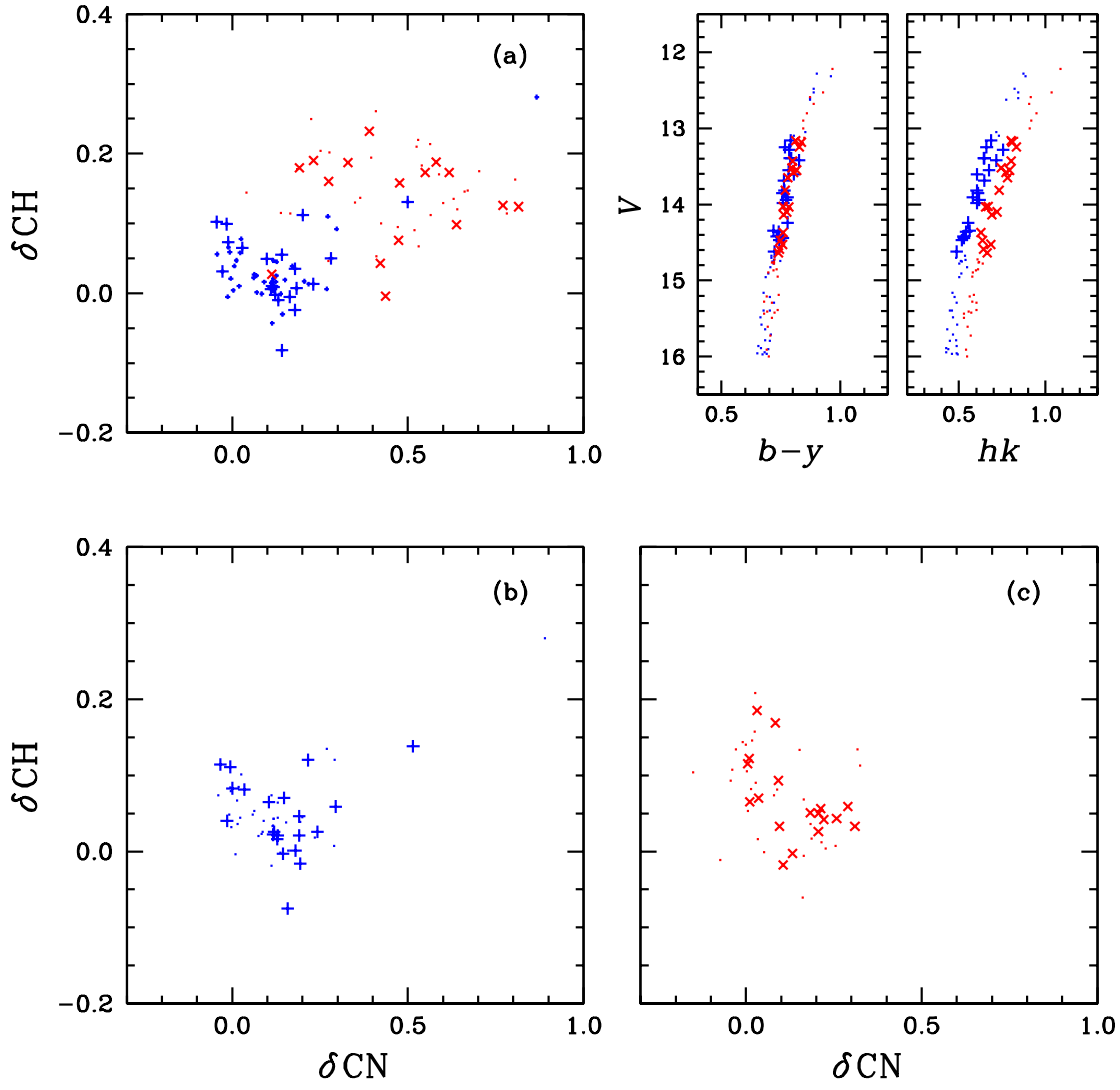

Fig. 19.— The distributions of the δCN(3839) versus the δCH(4300); (a) Using the common lower envelopes. (b) The *Ca-w* RGB stars using its own lower envelopes. (c) The *Ca-s* RGB stars using its own lower envelopes. The RGB stars around the $V_{\rm HB}$ are shown with the plus signs and crosses. The δCN–δCH positive correlation in (a) is most likely due to the metallicity effect between the two groups as shown in Figure 17.

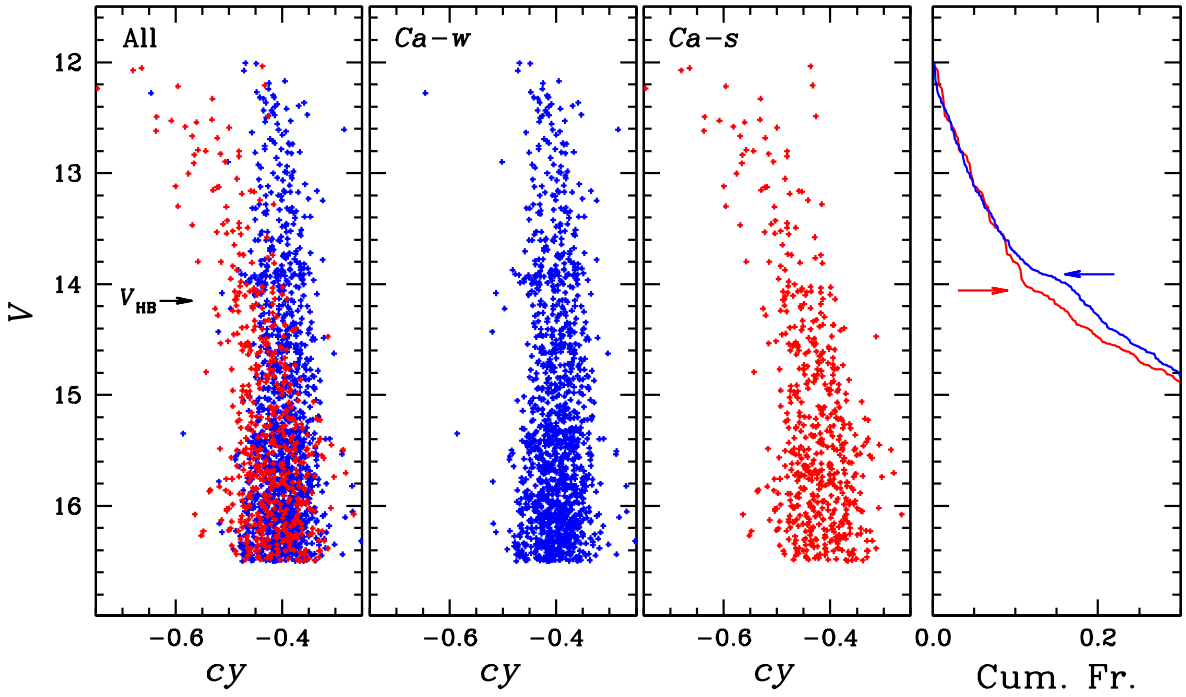

Fig. 20.— Plots of cy versus V CMDs of M22 RGB stars. The V magnitude of the horizontal branch, $V_{\rm HB} = 14.15$ mag, is indicated by an arrow. The cy spread at $V_{\rm HB}$ is $\sigma(cy) \approx 0.03$ mag in each group, corresponding to σ[N/Fe] ≈ 0.5 dex, if the spread in the NH absorption strengths are solely responsible for the cy spreads in M22 RGB stars. In the right panel of the figure, we show the cumulative LFs for the Ca-w and the Ca-s populations. We show the V magnitude levels of the RGB bump, V_{bump}, at which the slope of the LF changes abruptly, for each population by arrows. We obtained $V_{bump} = 13.91$ mag for the Ca-w population while 14.06 mag for the Ca-s population. The fainter bump magnitude in the Ca-s population suggests the metallicity effect on the bump brightness is greater than the effect from the helium enrichment is.

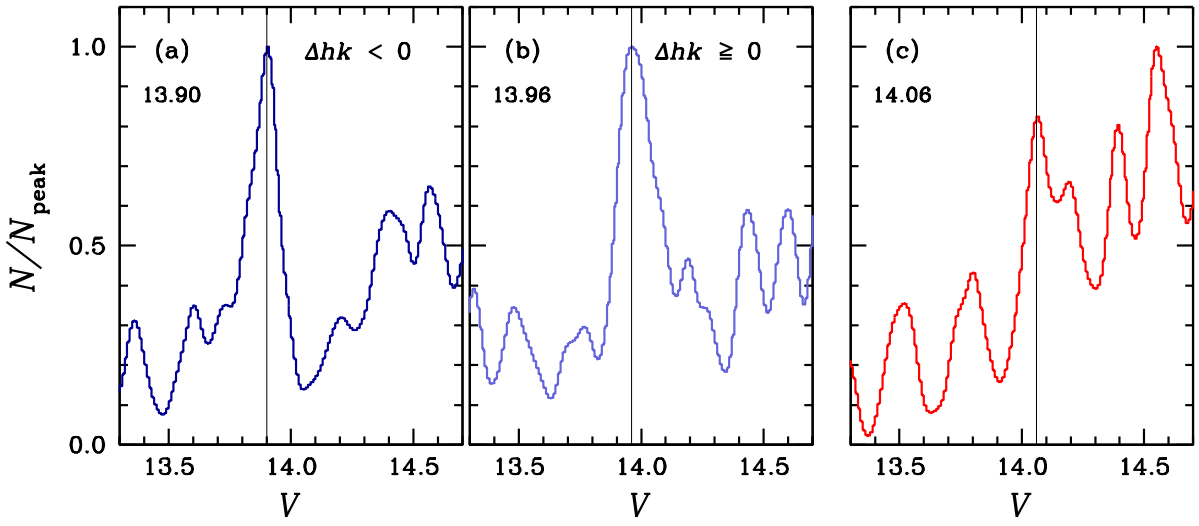

Fig. 21.— Generalized histograms for RGB stars against V magnitude. (a) *Ca-w* RGB stars with $\Delta hk < 0$ from Figure 7. (b) *Ca-w* RGB stars with $\Delta hk \geq 0$. (c) *Ca-s* RGB stars. The vertical thin lines represent V_{bump} for each subset, 13.90, 13.96 and 14.06 mag respectively.

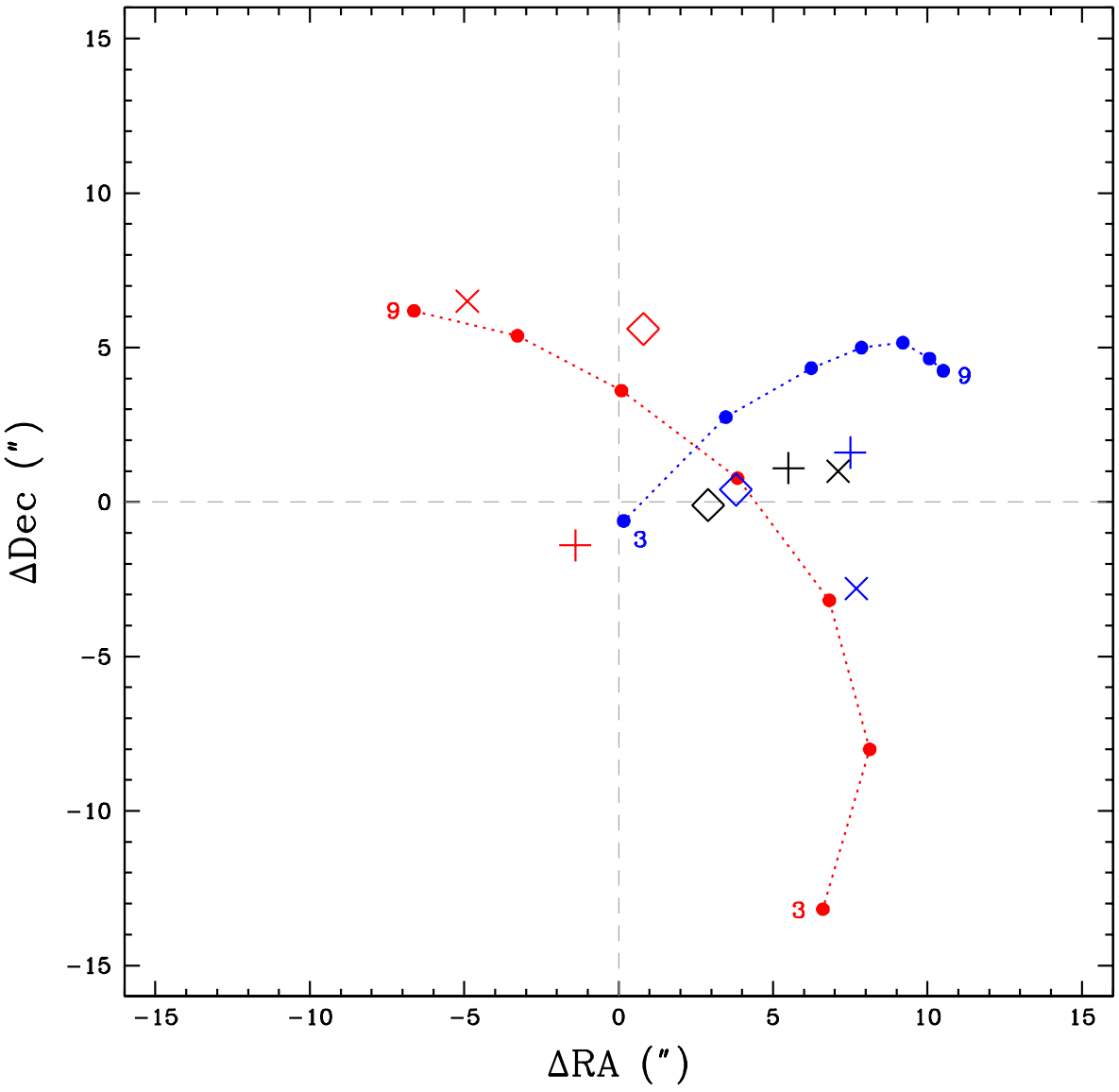

Fig. 22.— Relative positions of centers with respect to that of Goldsbury et al. (2010). The blue color is for the *Ca-w* group, the red color for the *Ca-s* group and the black for the combined RGB stars. Diamond signs denote for the centers from the simple mean, plus signs for those from the half-sphere method and crosses for those from the pie-slice method. The filled circles are centers of each population from the iso-density contour method from 90% to 30% levels.

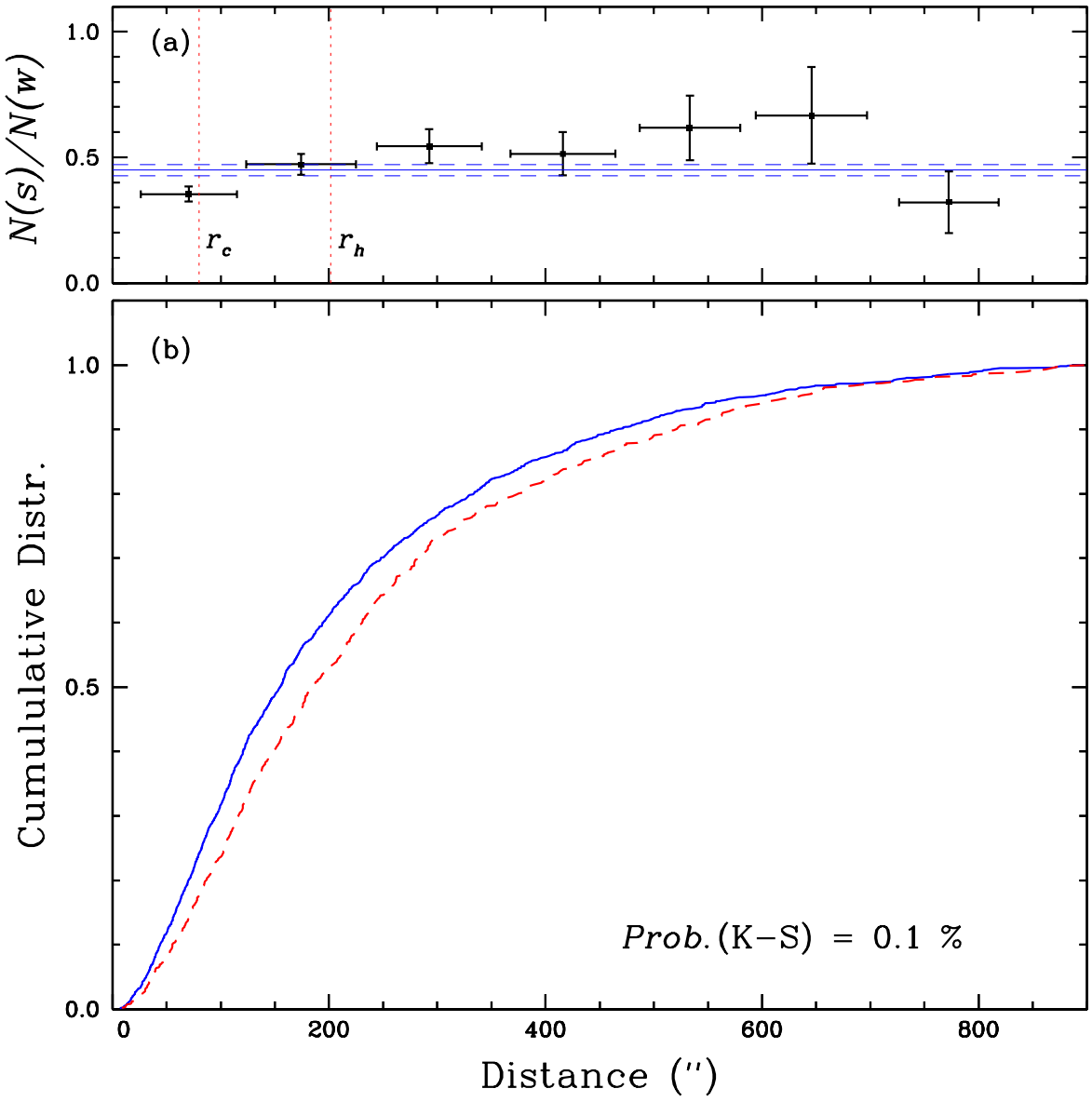

Fig. 23.— (a)The number ratios of the *Ca-s* to the *Ca-w* groups against the radial distance from the center. The RGB number ratio appears to have a weak radial gradient up to $r \approx$ 700 arcsec from the center, in the sense that the number of the *Ca-w* population is slightly more centrally concentrated than that of the *Ca-s* population. In the figure, the vertical lines denote the cluster's core and half-light radii and the horizontal lines denote the mean number ratio and the standard deviations. (b) Cumulative radial distributions of *Ca-w* (blue) and *Ca-s* (red) RGB populations. The *Ca-w* RGB stars are slightly more centrally concentrated. The K-S test indicates a probability of 0.1% that two populations are drawn from the same parent population.

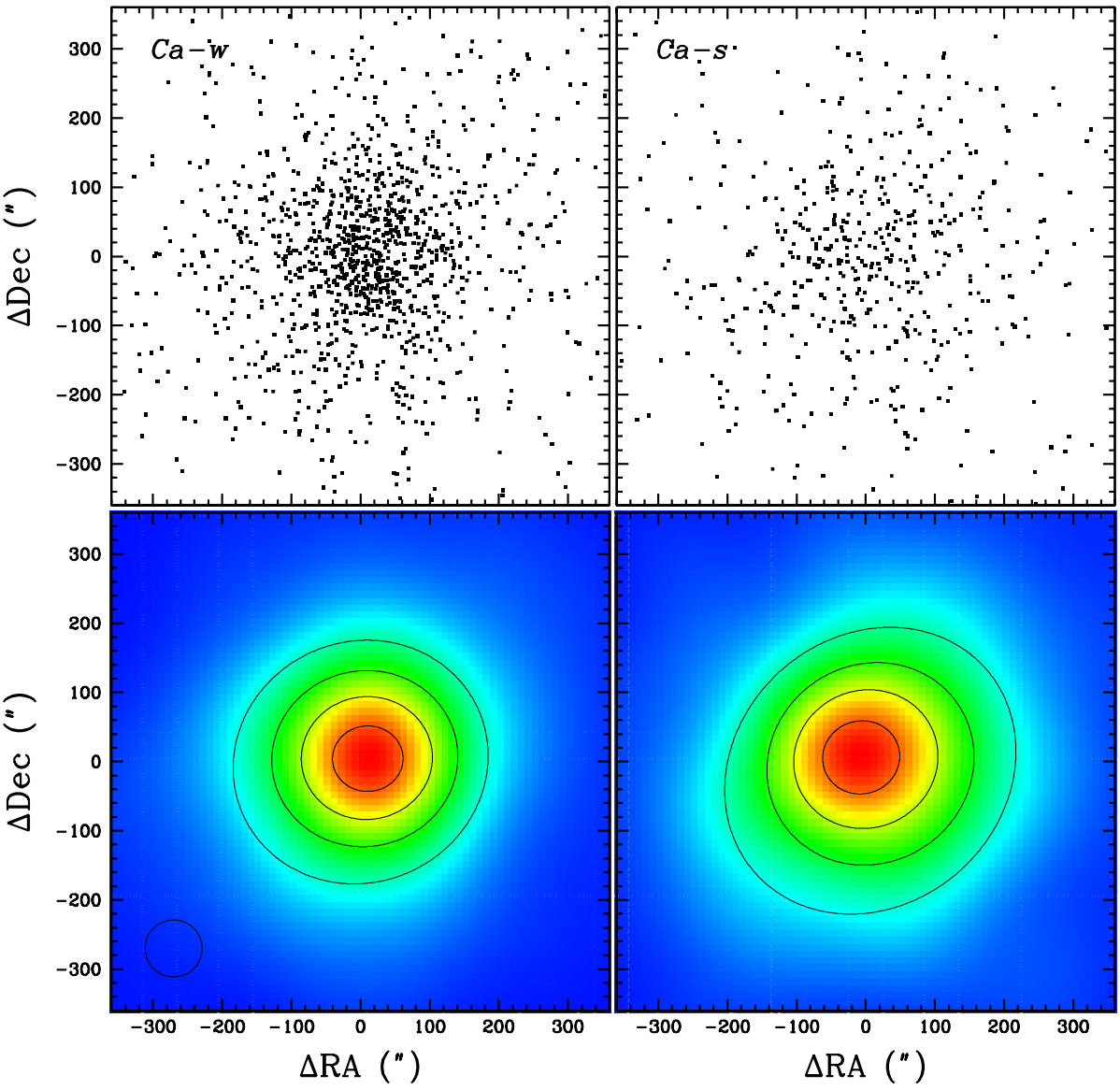

Fig. 24.— Spatial distributions of the *Ca-w* and the *Ca-s* RGB stars in M22 are shown in the upper panels and the smoothed contour maps using the fixed Gaussian kernel are shown in the lower panels, where we show the iso-density contour lines for 90, 70, 50, and 30% of the peak values for both populations. We also show the FWHM of our adopted Gaussian kernel in the lower left panel of the figure. Note that the distribution of the *Ca-s* RGB stars is more elongated.

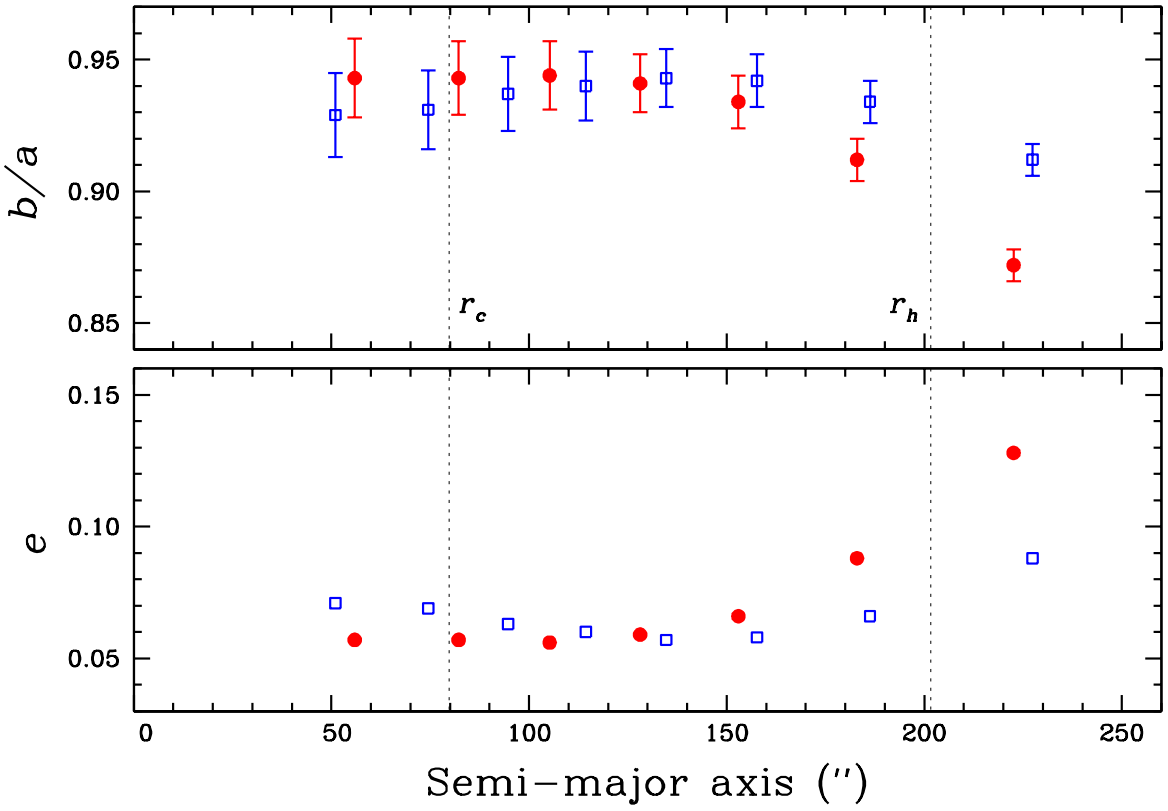

Fig. 25.— The run of the axial ratio, b/a, the ellipticity, e $(= 1 - b/a)$ of the *Ca-w* (blue) and the *Ca-s* (red) groups against the semi-major axis, a. The radial distributions for each group bifurcate at the radial distance larger than $a \gtrsim 150$ arcsec, in the sense that the *Ca-s* group is more elongated.

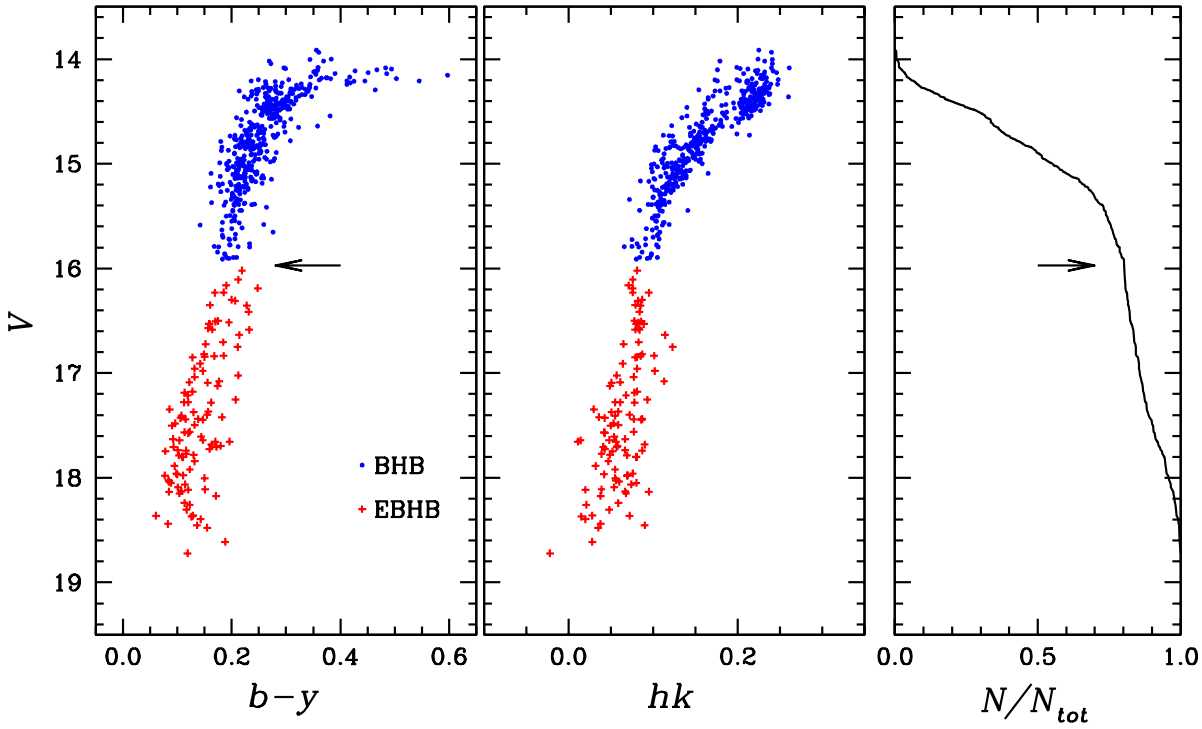

Fig. 26.— CMDs of the HB region of M22 and the cumulative LF of HB stars. The HB gap at $V = 15.97$ mag, with the zero slope in the cumulative LF of HB stars, is denoted by arrows. The BHB and EBHB stars are denoted by blue filled circles and red plus signs, respectively.

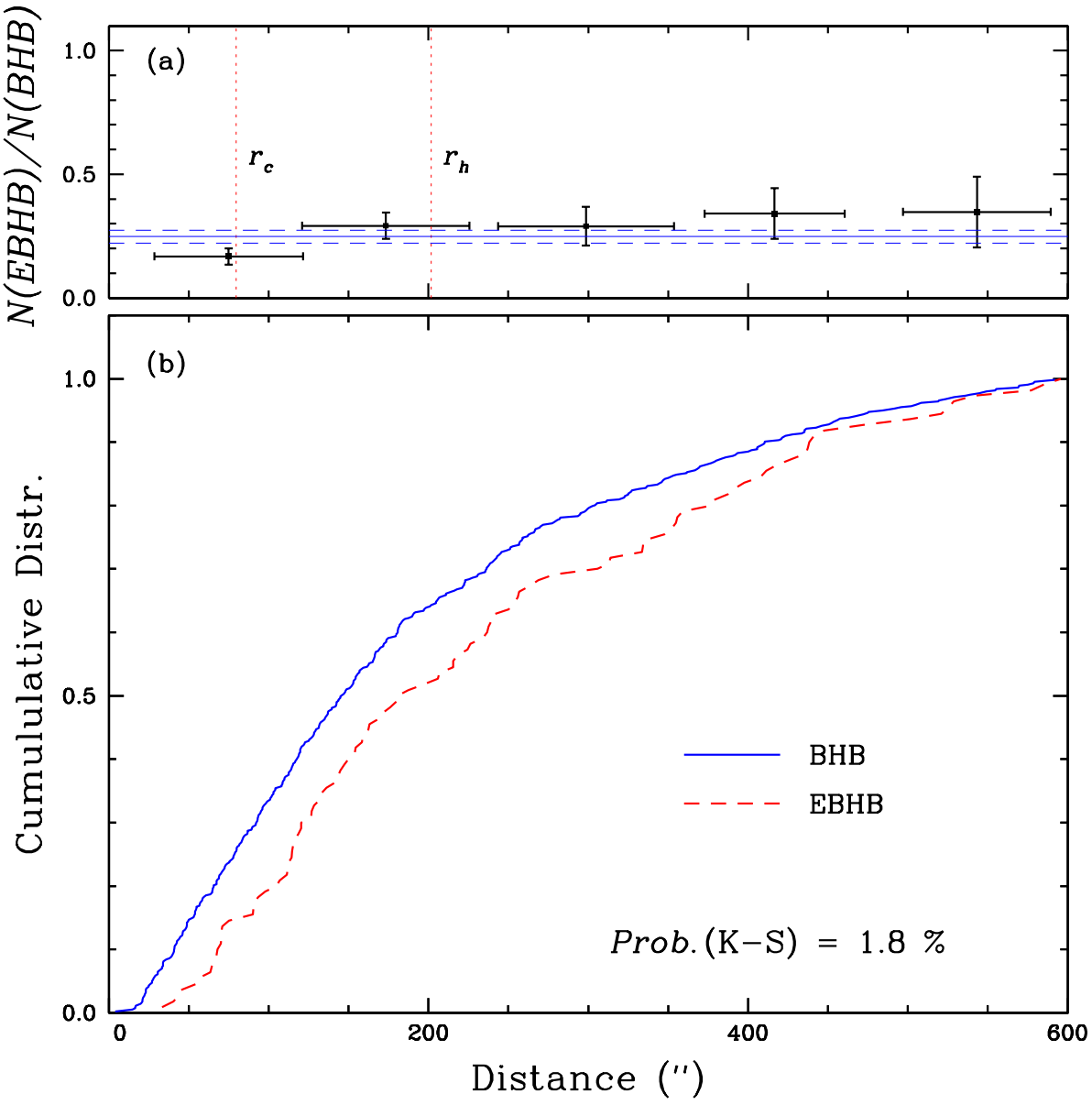

Fig. 27.— Same as Figure 23, but for the BHB and EBHB stars in M22. Similar to the *Ca-w* RGB population, the BHB population is more centrally concentrated.

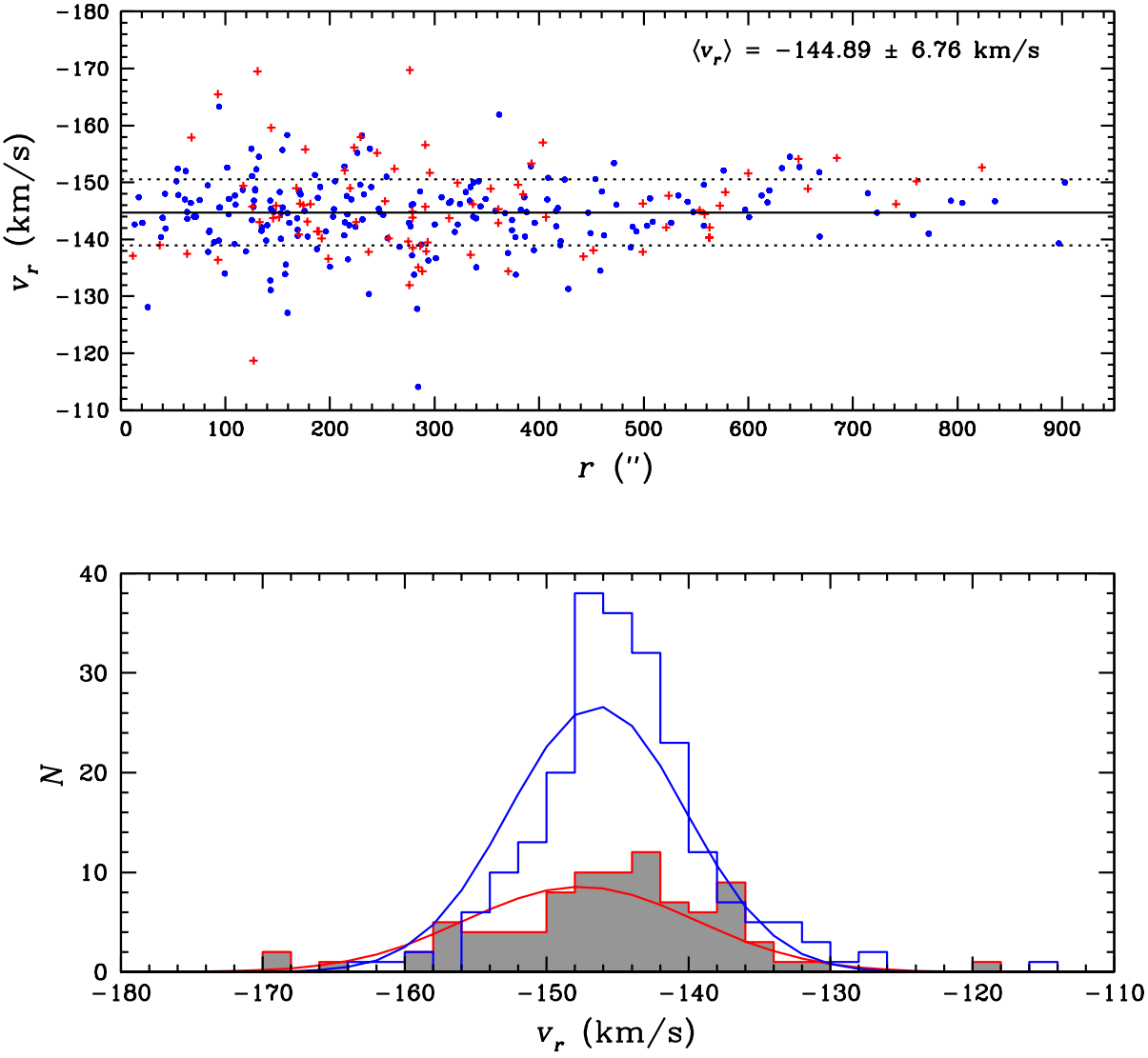

Fig. 28.— (Upper) The distribution of radial velocities of individual stars against the radial distance from the center.The blue color represents the *Ca-w* group and the red color the *Ca-s* group. No radial gradient can be seen. (Lower) Histograms for the radial velocities of each group with gaussian fits. The mean radial velocities and the velocity dispersions are very similar between the two groups.

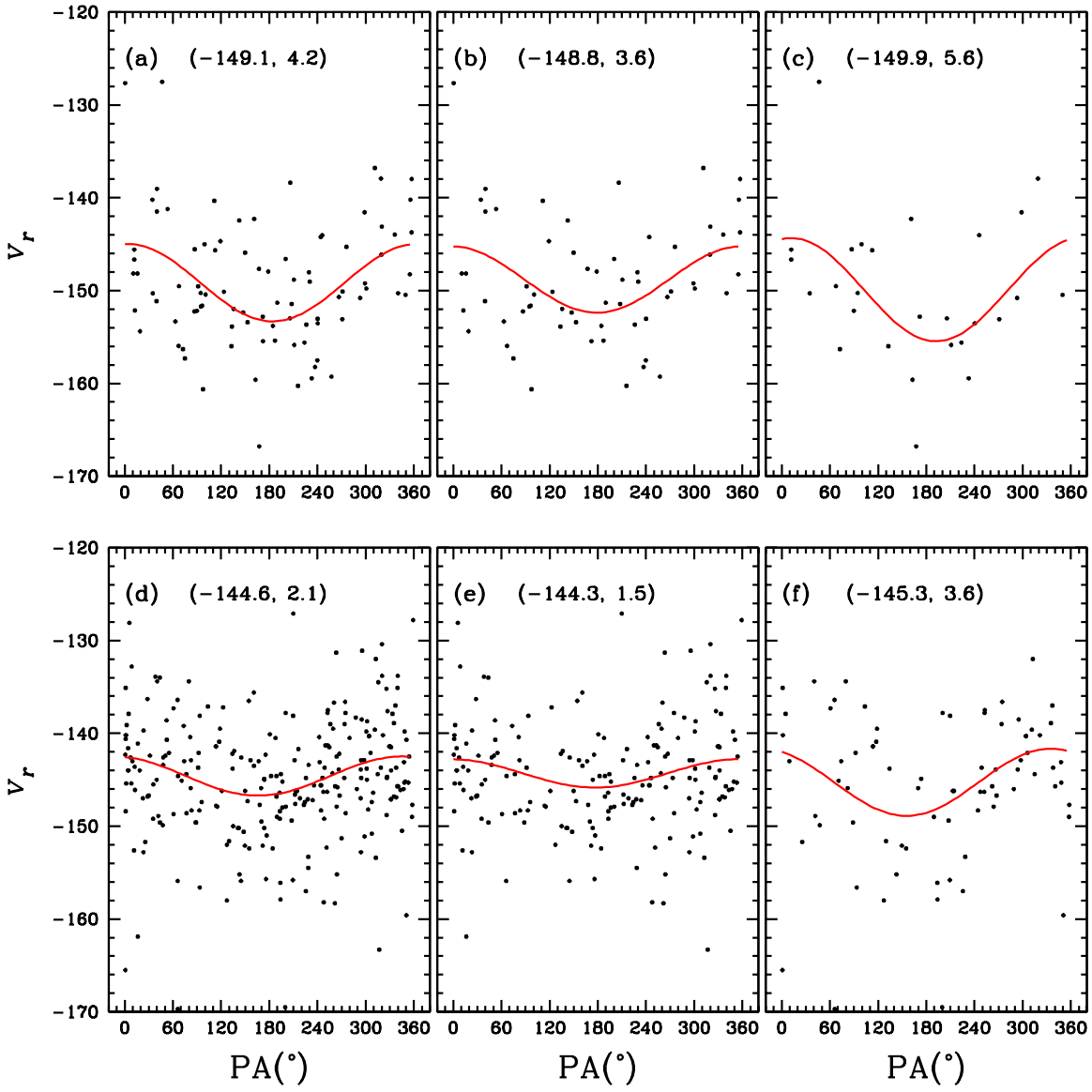

Fig. 29.— Radial velocities of individual RGB stars in M22 against their position angles. The two numbers in the parentheses in each plot denote the mean radial velocity and the amplitude of the mean rotational velocity. The red solid lines are sinusoidal fits to the data. (a) All RGB stars; (b) *Ca-w* stars; and (c) *Ca-s* stars with radial velocities measured by Peterson & Cudworth (1994). (e) – (f) As (a) – (c) but using stars measured by Lane et al. (2009). It is evident that the *Ca-s* group rotates faster than the *Ca-w* group does.

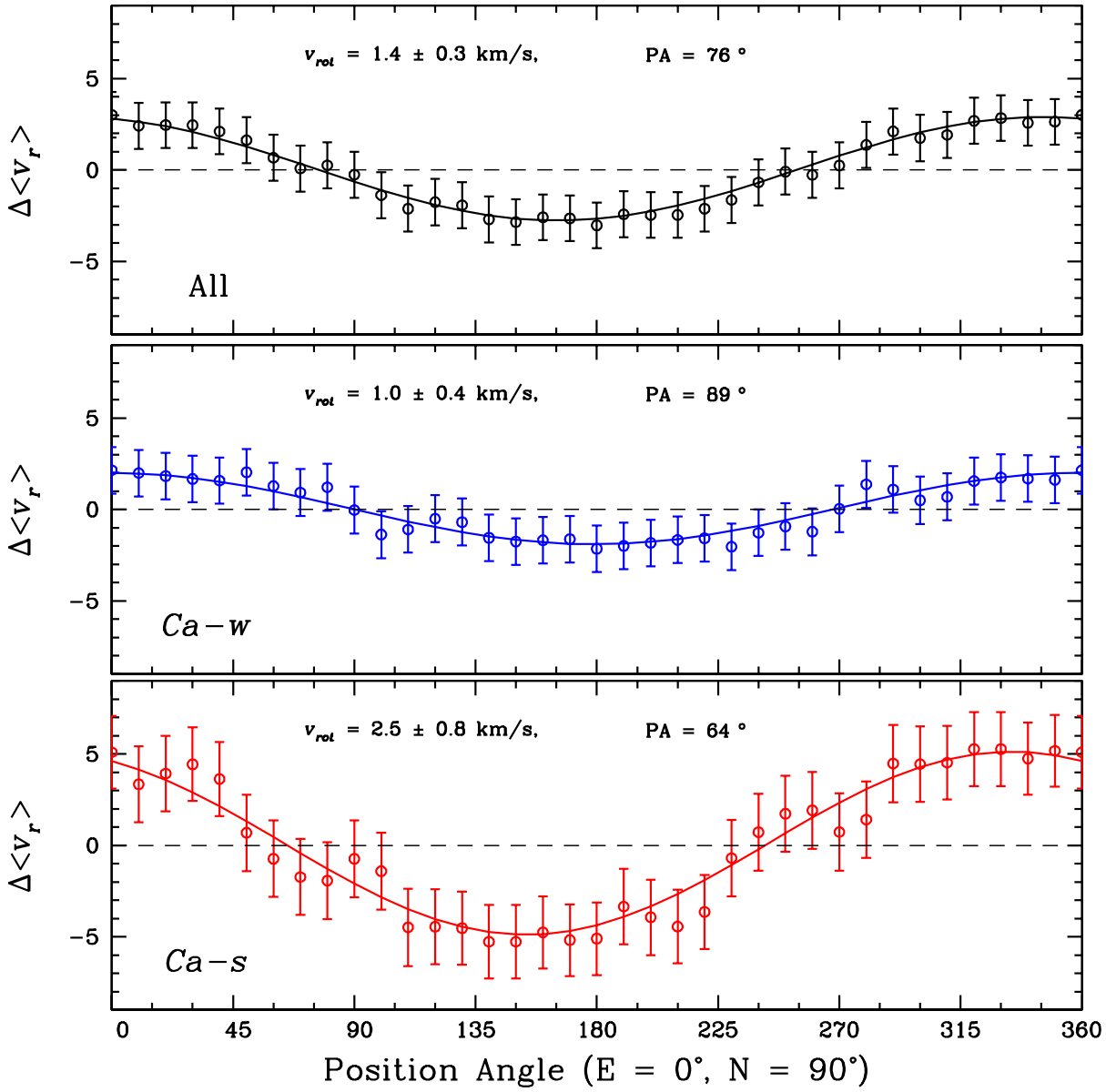

Fig. 30.— The difference in the mean radial velocities between both hemispheres against its position angle. Again, it is evident that the *Ca-s* group appear to rotate faster than the *Ca-w* group does. The position angle refers to that of the equator of the rotation, i.e. the axis perpendicular to the rotation axis. The error bar is the error of the mean.

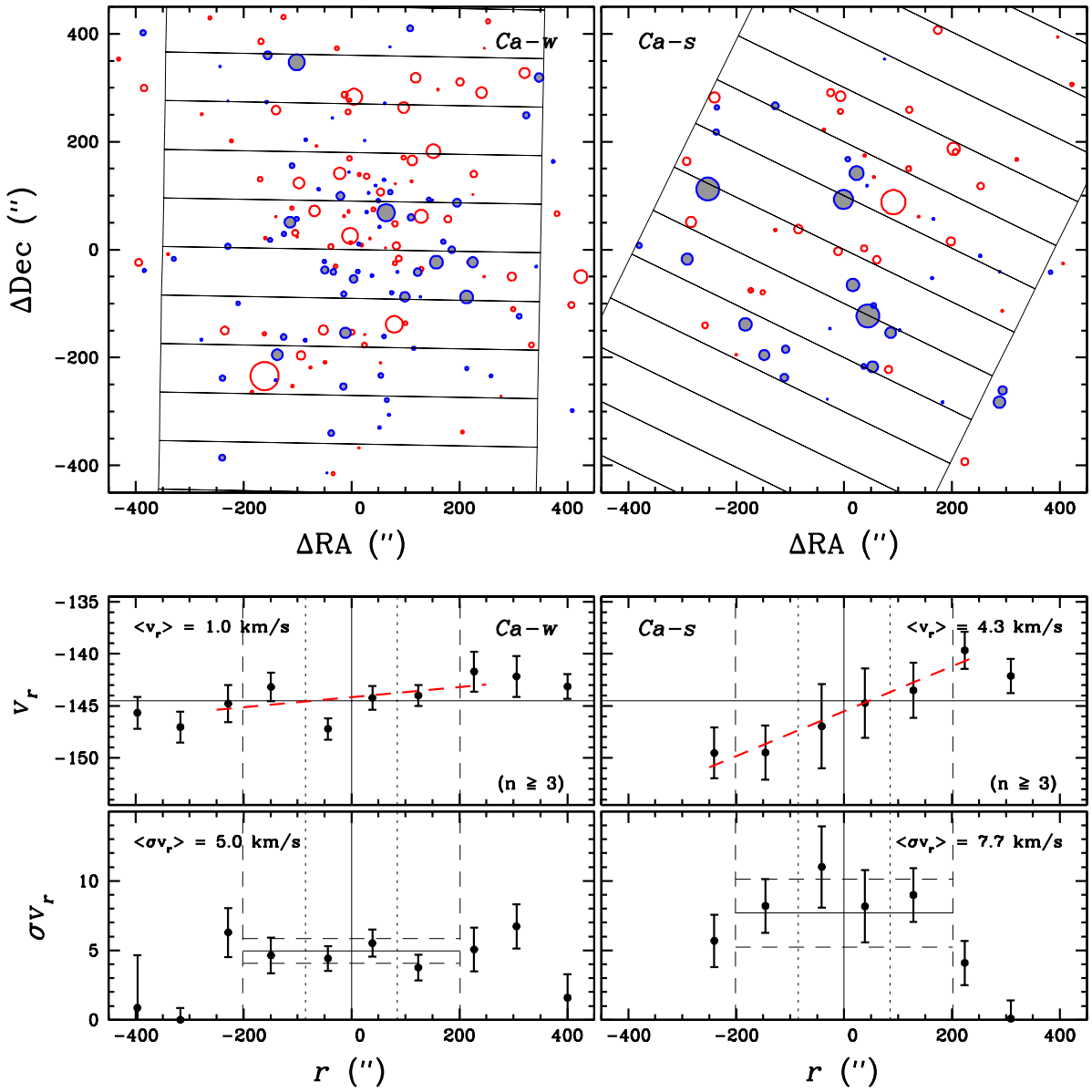

Fig. 31.— The upper panels show the distributions of RGB stars with radial velocity measured by Lane et al. (2009). The blue color denotes the blue shift and the red color the red shift. The size of each circle indicates the difference between the velocities of individual stars and the mean velocity. The bottom panels show the radial velocities and the velocity dispersions against the projected distance on the equator of the rotation. In the Figure, the position angles of 86° and 73° for the *Ca-w* and the *Ca-s* groups, respectively, are used. In the middle panels, red dotted lines represent the mean rotation. The maximum rotation velocities at the half-light radius are 1.0 km s^{-1} for the *Ca-w* and 4.3 km s^{-1} for the *Ca-s* groups. The velocity dispersion of the *Ca-s* group is slightly larger but those of both groups are in agreement within the errors.